Heat-transfer-based Biomedical Devices: Synergistic Numerical Simulations and Experimentation

A DISSERTATION
SUBMITTED TO THE FACULTY OF THE GRADUATE SCHOOL
OF THE UNIVERSITY OF MINNESOTA
BY

Winson Tan

IN PARTIAL FULFILLMENT OF THE REQUIREMENTS
FOR THE DEGREE OF
DOCTOR OF PHILOSOPHY

Professor Ephraim Sparrow

January 2015

Acknowledgements

First and foremost, I cannot express enough thanks to Professor Ephraim Sparrow for his unconditional support, teachings, knowledge, mentorship and friendship. I am so grateful to be able to work with him all these years, and extremely lucky to have an advisor who cared so much for my work and whose availability to answer questions and provide advice is a one-of-a-kind experience. In addition, I am thankful for my laboratory friends (John Gorman and Jungwon Ahn) to provide me guidance on using Ansys.

Dedication

This dissertation is dedicated to my family for their support and patience especially my wife, Michelle and son, Harry.

Abstract

A synergistic multi-faceted investigation was performed to demonstrate an approach to the design of thermal-based medical devices. The synergism was achieved by the mutual interaction of numerical simulation and experimentation. Focus was directed to two independent but related biomedical devices. One of these is a non-invasive means of measuring the body core temperature under both steady state and transient circumstances. A realistic application of such a probe is the monitoring of the temperature of a patient undergoing surgery. The investigation of the novel temperature probe involved the interaction of a model of the relevant physical phenomena, which was implemented by numerical simulation. A near-congruent experimental apparatus was designed and fabricated with the view to validate the numerical results. The excellent agreement between these two independent methodologies lends strong support to the validity of the model and the utility of the results obtained. The other thermal-based device is therapeutic in that it is used to supply infusants into the human body under critical conditions. The infusants may be blood, saline, or a mixture of the two. Critical conditions demand high rates of infusion. Furthermore, the temperature of the infusants must be above a critical value to avoid the onset of hypothermia. The goal was to maximize the temperature of the delivered infusant while at the same time avoiding catastrophic events such as hemolysis which is a thermal-based necrosis of the red cells. The mutual supportive outcomes of the simulations and experiments provided strong evidence of the validity of the modeling and its numerical implementation.

Table of Contents

List of Tables

List of Figures

CHAPTER 1

Introduction

Heat transfer has made a highly significant impact on biomedical engineering. In general, biomedical engineering may be regarded as including three stages of patient interaction: (a) diagnostic, (b) maintenance, and (c) therapy. In all of these stages, heat transfer continues to play major roles. In the diagnostic category, seemingly-simple measurements of temperature can foretell non-normal body function. Thermal maintenance may be achieved by enveloping the totality of the human body or components of it in an isothermal environment. In large measure, thermal-based therapies have replaced conventional surgery. For example, the extraction of tumorous tissue, a therapeutic action previously regarded as a scalpel-based procedure, is now performed either by hypothermic or hyperthermic therapy. The latter action reveals that the necrosis (cell destruction) of malfunctioning tissue can be thermally achieved by either elevated temperatures or depressed temperatures. The frequent use of depressed temperatures has been given a special designation: cryosurgery.

The history of thermal-based maintenance has evolved along with the general perfection of technology. Earlier means of maintaining near-normothermic body temperatures were based on water-filled mattresses whose therapeutic action tended to bring on skin damage. That outcome was a result of the high heat transfer coefficients of liquid water. An advance in that maintenance therapy was based on the recognition that a gaseous medium is endowed with much lower heat transfer capabilities than is water. To implement the efficient use of air-based temperature control, a necessary prerequisite is to uniformly disperse the medium over the entire body. In that regard, a novel manifold principle was invented and subsequently applied to create uniform air dispersal to body geometry encompassing various somatotypes.

Temperature measurement, although simple in principle, has been a long-term puzzlement. For example, the measurement of skin temperature has undergone a number of recipes over the years. These recipes have revolved around the number of skin sites needed to provide a suitable base for averaging. Along with that issue, many approaches for the implementation of actual measurement have been put forth. Aside from the thermometer, the thermocouple was the only available instrument for precise temperature measurement. The invention of the thermistor brought it into frequent use for the measurement of skin temperature. Equally recently, the perfection of optical thermometers as well as infrared cameras has encouraged their usage for skin temperature measurement. The apparent advantage of the foregoing non-contact devices is balanced by certain insufficiencies. Both optical thermometers and infrared cameras require that the healthcare worker input the radiative emissivity of surface being observed. Most healthcare workers are unaware of radiative heat transfer issues and would not know the appropriate emissivity value. A second insufficiency of the optical thermometers and infrared cameras is that, without proper shielding, these radiation sensitive devices may observe other sources of radiant energy besides the skin site being observed.

It is a still a matter of debate as to the proper means of determining the body core temperature. The body core is made up of major organs such as the heart, brain, kidneys, liver, and others. For diagnostic purposes, it is the core temperature that is most useful. It appears that practitioners have settled on an invasive approach to determine this critical parameter. That approach involves the swallowing of a tethered-temperature sensor which is allowed to descend to the level of the esophagus. This approach, while the most trustworthy of all candidate means of core temperature determination, is not highly favored because of its invasive nature.

There is a plethora of other sites that have been proposed and employed as surrogate core temperature measurement locations. A favorite site is the rectal, but it may be faulted because the mass of the rectum creates a large thermal mass and corresponding time lag in the temperature measured therein. Another often-considered site is the tympanic. The

uncertainty connected with this site can be traced to the ambiguous placement of the sensor in the ear. Two other locations are also commonly considered: axial and "oral". The axial is actually the armpit, and its virtue as a measurement site is its proximity to a major blood vessel. Similar to the aforementioned uncertainty concern of the tympanic measurement, the placement of the sensor in the axial is critical to a proper measurement. The under-the-tongue placement of a temperature sensing instrument is by far the most commonly employed site. Among biomedical researchers, its temperature determination is regarded as the least accurate.

In recent years, renewed attention has been given to the forehead as a candidate measurement site for the determination of the body core temperature. The first known use of this site occurred in 1971. A number of improvements have been made in the underlying technology since that time. Notwithstanding this, the forehead has been lightly used for temperature measurements until the very recent past. That upsurge of interest can be traced to the appearance of the radiation-based swipe optical thermometer. The commercialization and intense promotion of that thermometer has brought it into the perceptual field of the general public. There a number of features of swipe thermometers that are technically defective. For one thing, the radiation emissivity of the targeted skin is fixed by the device in a "one-size-fits-all" approach. Another equally critical issue is that it measures the skin temperature and not the core temperature. In that regard, it is noteworthy that a major artery, the carotid, passes very near to the outboard ends of the forehead. Therefore, a proper usage of any forehead-based temperature measurement should be tailored to take advantage of the proximity of those arteries. Even so, the skin temperature will necessarily be different from the temperature of the blood carried by the carotid arteries.

To ensure that a temperature measurement at a proper forehead site provides a valid measurement of the core temperature, it is mandatory to suppress heat flow across the thickness of the tissue and forehead bone that separates the artery from the skin surface. The swipe thermometer does not in any way create such a necessary condition.

The discussion set forth in the immediately preceding paragraph leads to one of the foci of the research of this thesis. That focus is a first-principles, logic-based investigation of the optimal core temperature determination by means of measurement at an adiabatic forehead site. The investigation synergistically involves both numerical simulation and laboratory experimentation. The evolved model is free of any inappropriate assumptions and is a true description of the participating physical processes. Those processes include: (a) unsteady, multi-dimensional heat conduction through tissue and bone, (b) blood profusion through tissue, (c) natural convection heat transfer at exposed surfaces, (d) thermal radiation at exposed surfaces, (e) realistic operational scenarios, and (f) control system realities.

The investigation is set forth in Chapters 2, 3, and 4. An encompassing literature search pertinent to the relevant issues is presented at the beginning of Chapter 2.

The second focus of this thesis is the therapeutic infusion of fluids into the human body. Such fluids, if needed to be infused in amounts of 10 units or more, must be preconditioned to a temperature of 30^{o}C prior to introduction into the body. The fluids in question are blood abetted with saline and saline proper. The technology involved in a fluid warming device involves a delicate balance because of the possibility of hemolysis of blood cells.

A fundamentals-based approach to achieve the most technologically advanced biological fluid warmer is described in Chapters 5 and 6. The critical issues addressed in the investigation is the rapidity of the achieved warming and the failsafe operation of the device. The relevant literature relating to this work is set forth in Chapter 5. The particular strength of the approach is that it synergistically encompasses both numerical simulation and complementary experimentation.

The dealt-with phenomena in the fluid warmer development encompasses: (a) three-dimensional, unsteady, laminar flow in complex fluid-flow passages, (b) unsteady conjugate convective heat transfer in the flowing fluid and conductive heat transfer in the heating means, and (c) strict adherence to reality-based operating conditions. A full-blown experimental facility was designed and fabricated to validate the numerical simulation. As with the simulation, the facility enabled high fidelity adherence to the nuances encountered in the use of fluid warming devices.

It was demonstrated that strict modeling, both in analysis and in experimentation, is able to yield outcomes that are failsafe.

It is also noteworthy that both of the investigations performed in this thesis gave rise to ill-posed mathematical problems. By ill-posedness, it is meant that some of the parameters that appear in either the governing partial differential equations or in the boundary conditions are not known *a priori*. This situation demanded that unique approaches be devised in order to obtain both the unknown parametric value and the final complete solution.

CHAPTER 2

Probe for Core Body Temperature Monitoring

2.1 Introduction to core body temperature

Core body temperature is one of the most common and important clinical measures. The commonly accepted core temperature is around 37°C; however, measured temperatures at different locations in the body may differ from this value, especially at the extremities. Rectal and other measurements taken within the body cavity may be slightly higher than oral measurements [1]. Core temperature is usually measured under the armpit, in the mouth, rectum, or ear. Depending on location, values of normal body temperatures are in following ranges:

- armpit (axillary) – 34.7 to 37.3°C
- mouth (oral, sublingual) – 35.5 to 37.5°C
- rectum – 36.6 to 38.0°C
- ear (tympanic) – 35.8 to 38.0°C

The above are surrogate measurement sites for the core temperature, but the true core temperature is considered to be the blood temperature in the brain and heart. Many practitioners accept the aforementioned referencing sites as providing adequate assessment for the core temperature [2].

To maintain and balance the temperature of the human body, thermal regulation mechanisms are operative. The temperature regulation function is housed in the hypothalamus. An increase in core temperature will result when blood flows from the skin surface to the muscle and the liver, thereby reducing the body heat loss. On the other hand, the core temperature will decrease when the blood flows to the skin surface

and causes transpiration. The monitoring of core temperature serves to provide a prognosis to detect fever, malignant hyperthermia, and hypothermia. Through transpiration, the hypothalamus tries to maintain normal body temperature. Fever is accompanied by an increase in the body temperature relative to the hypothalamus' set point of 1 to 2°C [3].

Most fevers are caused by infectious disease and are treated with antipyretic medications. When exercising vigorously in a hot environment, the rate of heat loss from the body surface is exceeded by the rate of heat generation. This situation is termed hyperthermia (heat exhaustion and heat stroke). Unlike a fever, the increase in body temperature is not controlled by the hypothalamus and rises to a level that is life-threatening with temperatures that may rise above 40°C. In this condition, physiological and cognitive performance may be decreased [4]. Mild to severe hyperthermia are treated with cooling and rehydrating with such actions as bathing in cool water and drinking water. In the condition termed hypothermia, the body temperature drops 1 to 2ºC below normal temperature. This drop inhibits normal metabolism and bodily functions. Hypothermia is due to excessive exposure to a cold environment or may be medically induced. Treating hypothermia involves bringing the person into a warm environment immediately [3].

2.2 Approaches to measure core body temperature

Existing methods to accurately measure core temperatures are, for the most part, invasive; for example, insertion of temperature probes in the rectum, nasal cavity, or esophagus. These methods are not convenient for long term monitoring as they create discomfort to an individual, especially when awake. For this and other reasons, there has been considerable motivation to use non-invasive means to measure the core temperature. Well-established non-invasive means have involved the tympanic membrane (ear), oral (mouth), and axillary (arm pit), but these have shown to have marginal sufficient accuracy [5, 62].

A study conducted by Frommelt and colleagues [6] evaluated the temperature-measurement accuracy of non-invasive devices by comparing with oral temperature measurements. The non-invasive devices were radiation-based instruments placed in the ear (tympanic) and on the forehead. The patient sample size included 84 postoperative persons within the age range of 18 to 85 years who had been released from the surgical unit within 4 to 6 hours. Both of the studied devices showed significant differences when compared to the oral, with the tympanic thermometers showing the greater deviations up to 18%.

A major uncertainty encountered when using a tympanic radiation thermometer is the need to set the emissivity value required by the device. A radiation thermometer accurately measures temperature when its tuned emissivity value is equal to the emissivity of the surface being viewed. However, the option to set the emissivity is not available on many radiation thermometers. There exists some difference of opinion as to what is an appropriate value of the emissivity to tune to [55].

Most available sensors are too large to fit into the aural canal in order to view the tympanic membrane. Another difficulty in getting an accurate measurement using a tympanic thermometer is that the temperature of the ear canal is not uniform and is different from that of the tympanic temperature membrane [56].

With regard to the use of a radiation-based instrument for the measurement of forehead temperature, the obtained information relates to the surface of the skin rather than to the temporal artery. The latter temperature depends on environmental factors such as ambient temperature, relative humidity, and convection. These factors affect the blood supply to the skin and thus create a temperature difference between the skin and the core [57].

2.3 Background on non-invasive deep temperature thermometer

A novel approach to determine core temperature from a measured value of the skin

surface was first utilized by Fox and Solman in 1971 [7]. They postulated that if the skin surface were adiabatic (zero heat flux) at the location of temperature measurement, the measured temperature would be equal to the core temperature. If valid, the method of zero heat flux provides a way to have convenient surface measurements to determine core temperature in a reliable, safe, and easy-to-use manner. In the Fox-Solman method, a device applies heat to the location on the skin surface where the temperature is to be measured. The rate of heating is made to be precisely equal to the rate at which heat would normally flow from the skin surface to the environment. The validity of this approach is based on the postulate that the attainment of zero heat flux at the skin surface guarantees that there will be no subsurface heat transfer.

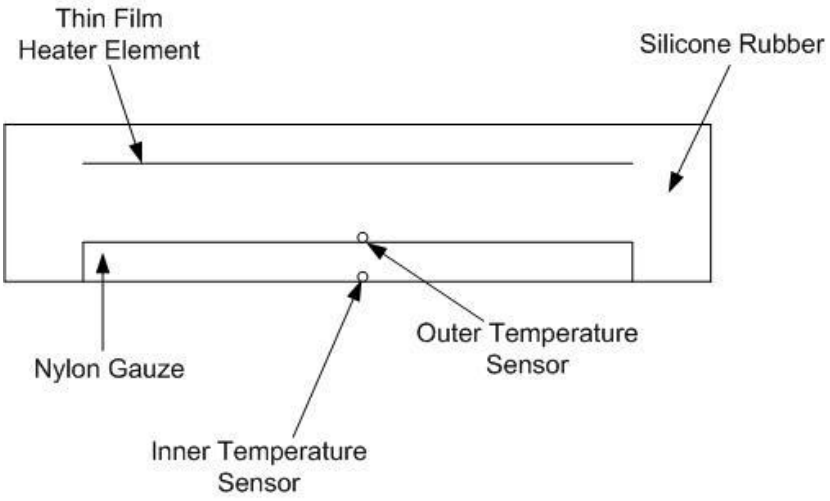

Figure 2-1. Initial muti-layered, zero-heat-flux probe design by Fox and Solman.

As is seen in the schematic diagram of Figure 2-1, the Fox-Solman probe is a multi-layer device which consists of two thermistors separated by a thermal resistance, a thin-film heating element, and nylon gauze. The probe's dimensions are 6 cm by 6 cm in planform by 0.6 cm thick. The layers are encapsulated with vulcanized silicone rubber. The inner temperature sensor is in contact with the skin and measures its temperature, purported to be the core temperature. The outer temperature sensor is positioned above the inner temperature sensor and both are below the heating element. The heater is activated when

the outer sensor has a lower temperature value than the inner sensor. When the temperatures of the inner and outer sensors are the same, it is assumed that zero heat flux prevails. The first application of this approach was to measure the temperature of the upper sternum. The measured temperatures were found to be 0.2 to 0.4º C lower when compared to other candidate core temperature sites such as the rectum and mouth [8].

Kobayashi, Memoto, Kamiya et al. improved on the Fox and Solomon zero heat flux device in 1975 to increase its accuracy. They added a metal conductive frame made of copper encapsulating the outer edge with the heater being placed on top of the covering as shown in Figure 2-2.

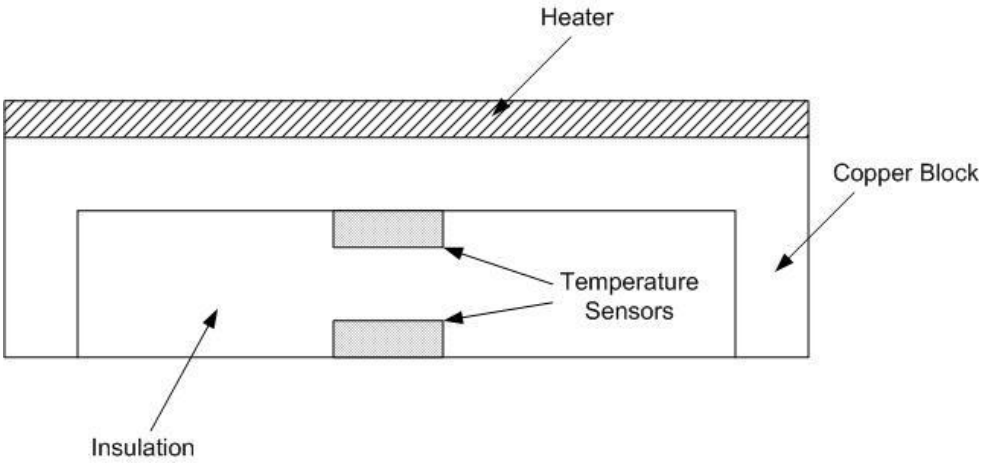

Figure 2-2. Modification of heat flux probe by Kobayashi, Nemot, Akira et al. with the addition of the copper block.

This addition was motivated to reduce the temperature difference between the two temperature sensors and to minimize extraneous heat losses. Experiments were conducted on a 10-kg mongrel dog to obtain temperatures for comparison with the rectal temperature measurements. The experiment consisted of placing the improved probe on the abdominal region of the anesthetized dog. A rubber bladder with two tubes was inserted into the dog's abdominal cavity. Warmed water was circulated through the bladder. Temperature measurements were made by the probe and of the warmed water,

and the results showed that the probe's accuracy of 0.3ºC and of 0.8-0.9ºCwhen compared against water temperatures of 34.6ºC and 41.6ºC respectively [9].

Terumo Corporation commercialized the modified probe in 1979. With a slight change from previous designs, Togawa placed an aluminum casing encompassing the entire probe to prevent radial heat flow shown in Figure 2-3 [34, 35].

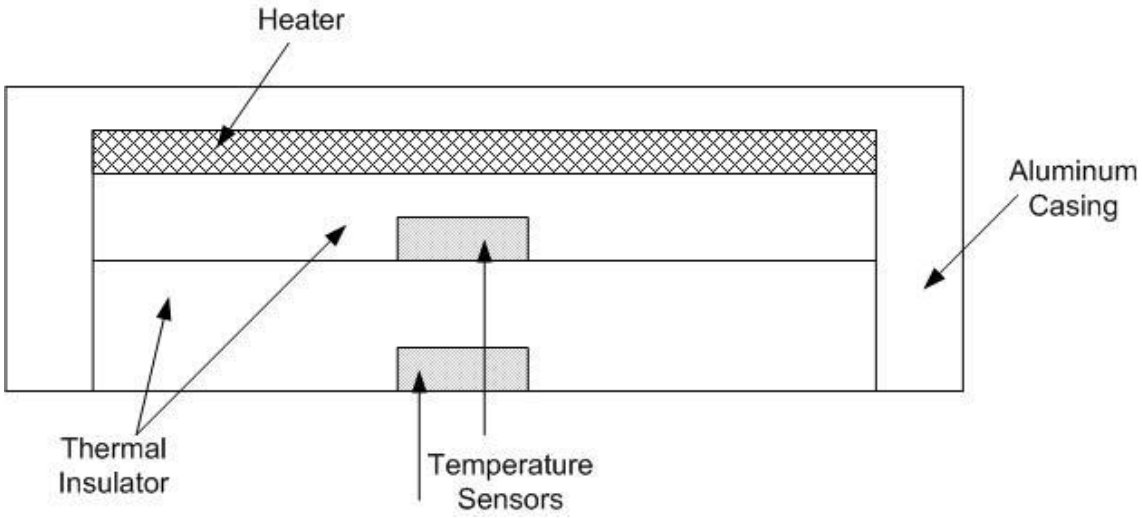

Figure 2-3. Schematic diagram of probe designed by Togawa showing an aluminum casing encompassing the components.

The diameter of the probe was 45 mm with a thickness of 13.5 mm. Testing of the probe was conducted on patients in the occipital region with accuracy within 0.1ºC when compared to the rectal temperature [10].

Binzoni and colleagues added the capability to measure both the purported core temperature and the oxidative metabolism simultaneously in 1999. They updated the Fox-Solomon probe [7] by adding two slots in the body to mount two optical fibers with end mounted prisms [11]. Their probe design is shown Figure 2-4.

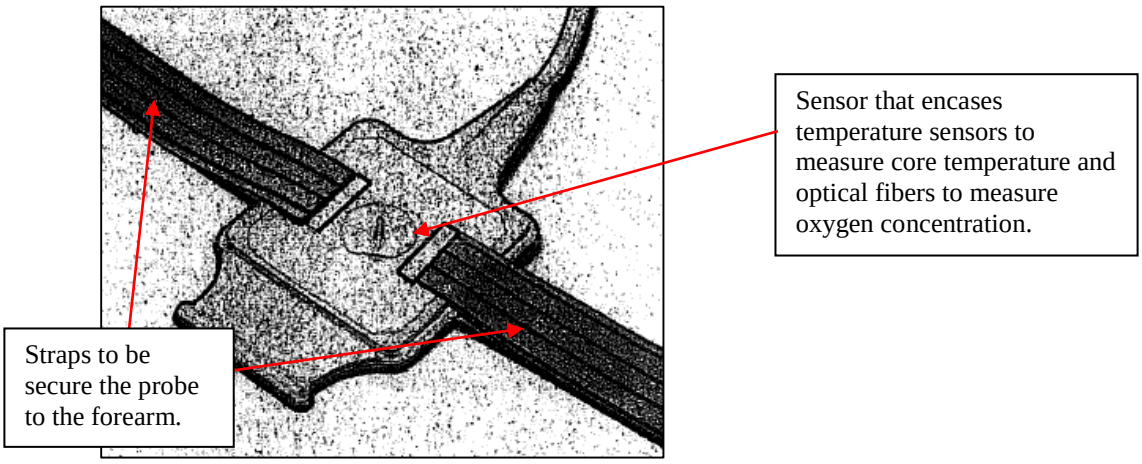

Figure 2-4. Probe design by Binzoni, Springetti, Dalton et al. that combines deep body temperature and near infrared spectrum.

The combined features of both deep body temperature and near infrared enabled both the temperature measurement of a region of 3 x 3 x 1.5 (depth) cm and changes in oxyhaemoglobin and deoxyhaemoglobin concentration in the tissue.

Further research to the original zero heat flux probes were developed in 2009 (Kimberger and colleagues [12, 54]). They developed a heat flux probe with a double sensor that calculates the core temperature with inputs from the skin temperature, heat flux through the sensors, and heat losses to the ambient from the outer surfaces. The unique feature of this design is the lack of a need for a heater. Their version of this sensor is displayed by Figure 2-5.

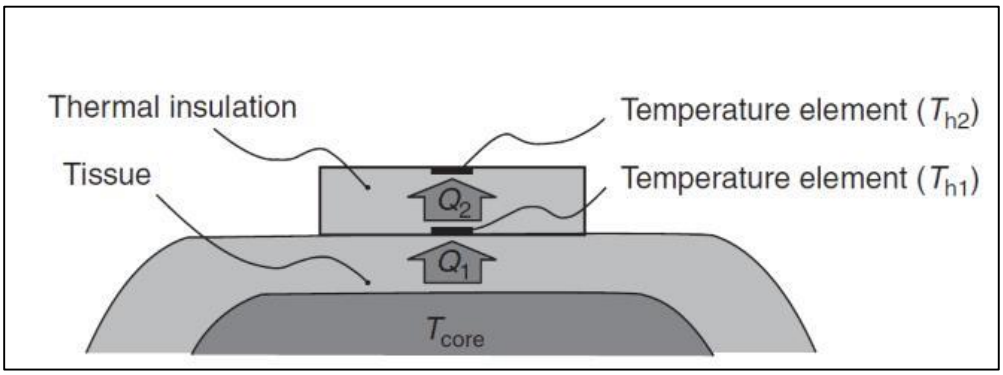

Figure 2-5. Pictorial view of double sensor temperature measurement device. The device contains two temperature probes. Sensor T_{h1} measures the skin temperature and sensor T_{h2} measures the ambient environment. An insulation disk is placed between both temperature probes.

The core temperature is calculated using estimated heat conduction values for the insulation and human tissue and along with the measured skin (T_{h1}) and ambient (Th2) temperatures. The probe was placed on the forehead and skin temperatures were recorded with the T_{h1} sensor. A necessary 2^{o}C offset was added to approximate the core temperature in order to compensate for the skin temperature being less than the core temperature. Studies [58, 59] show the need to include this offset for the final core calculation. Clinical results on perioperative and intensive care patients were ±0.5^{o}C of the esophageal temperature [12].

In 2010, Zeiner and colleagues purportedly determined core temperature with a prototype non-invasive forehead temperature measurement also using the concept of zero heat flux. The probe was comprised of flexible layers of electronics and thermal insulation. A heating element was placed on top of the probe with insulating layers on top of it. The probe was continuously monitored and adhered to the subject's forehead by velcro straps. The prototype design is shown in Figure 2-6.

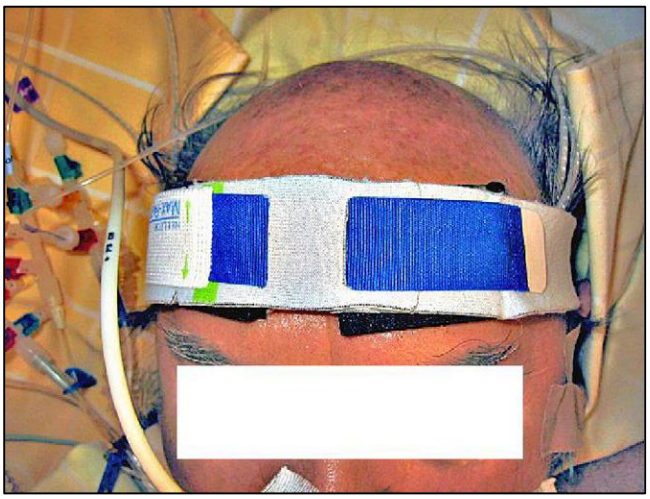

Figure 2-6. Non-invasive continuous cerebral temperature sensor placed on the patient's forehead.

The prototype probe's temperature measurement was compared to that from an esophageal for patients undergoing mild therapeutic hypothermia after cardiac arrest. The prototype probe had an accuracy of 0.6ºC [13].

Using the same probe design, Teunissen and colleagues [1] used it in a study to see if the probe could provide reliable temperatures when the body temperature was rapidly increasing and decreasing in the range of 36.5 to 38.5ºC and under hot ambient conditions. Similar to Zeiner's application [13], the probe was placed on the forehead and compared to the esophageal temperature. Results from the study showed that the probe's temperature was in agreement with the esophageal temperatures within ±0.40ºC. The conditions of the study were with an ambient of 35ºC. Teunissen concluded that these studies showed that the probe works well at room and warm ambient quiescent environments; however, the situation where the probe operates in a cooler ambient and with convective air movement needs to be investigated. In the latter setting, the temperature difference between the skin and core will be greater and more thermal insulation or a larger sensor would be required.

2.4 Fabrication of zero heat flux probe to be investigated

This section describes the first logic-based design of a zero-heat-flux temperature probe for human use. Figure 2-7 shows the probe assembly and its exploded view.

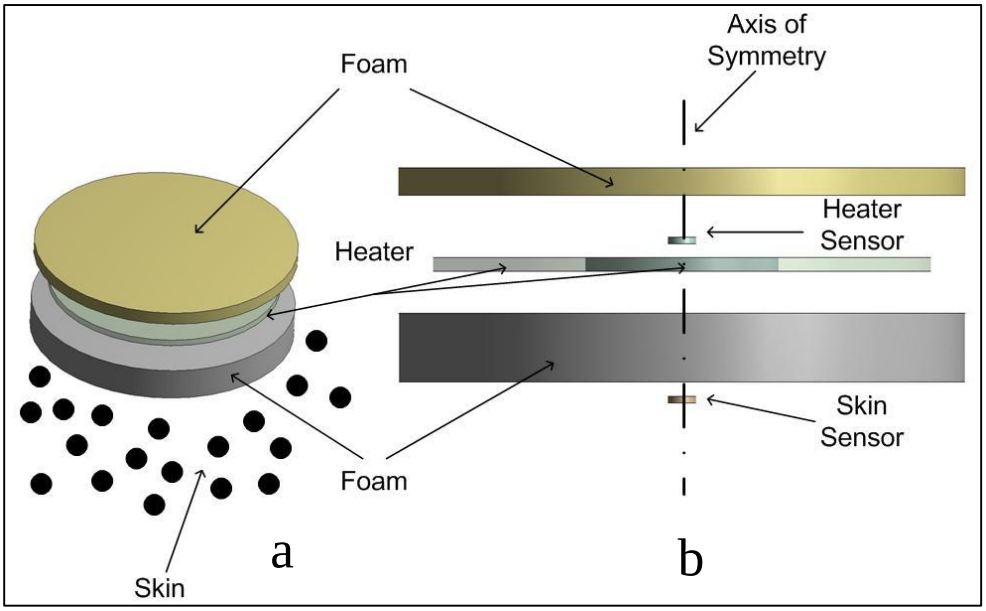

Figure 2-7. Zero-heat-flux probe assembly (a) Fully assembled pictorial view.
(b) Elevation exploded view

Common to other probe designs, this concept has a heater placed between two disks of thermal insulation; each of which is equipped with a temperature sensor. The first temperature sensor lies in the same plane as the heater shown in Figure 2-8.

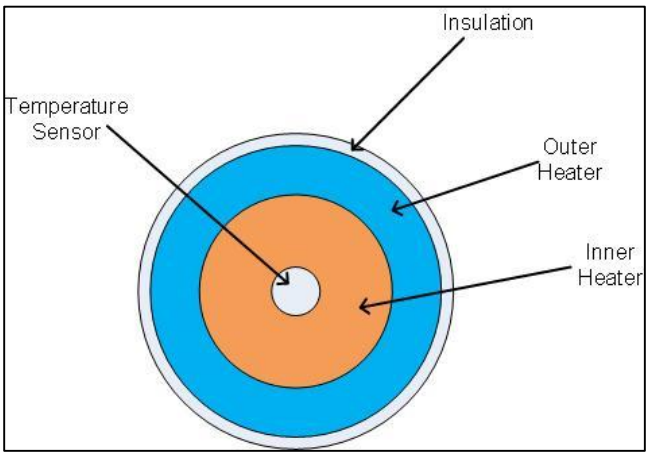

Figure 2-8. Annulus two-heater design with temperature sensor lying in the same plane as the heater.

The other sensor is adhered to the bottom insulation disk at the interface between the insulation disk and the skin of the patient (see Figure 2-7). A unique feature of this heater arrangement is that its design enables radially non-uniform heating. It is composed of two annular sections, each with a different Watt density. The motivation for this design is to minimize the radial heat loss by making use of the guard-heater principle [60].

Another design specification is to achieve a zero heat flux at the interface at the probe and the skin of the subject. To implement this goal, the two aforementioned temperature sensors were utilized. They were wired to facilitate the measurement of the temperature difference between them. The zero heat flux condition was regarded as being achieved when the temperature difference was approximately zero to within 0.1ºC. The heater power was servo-controlled to achieve this level of temperature commonality.

Previous designs (as discussed earlier) from Fox and Solman [7] and Togawa [10] only used one-element heater. To minimize radial heat loss, Togawa placed an aluminum shroud around the assembly as seen in Figure 2-3. This approach may be questioned from a heat transfer standpoint inasmuch aluminum is not an insulator. Various configurations of Togawa's design have evolved over the years, where improvements

have been to the temperature display, geometric issues of weight, diameter, and thickness as shown in Figure 2-9. However, all of the different configurations have maintained a single-element heater [14, 35].

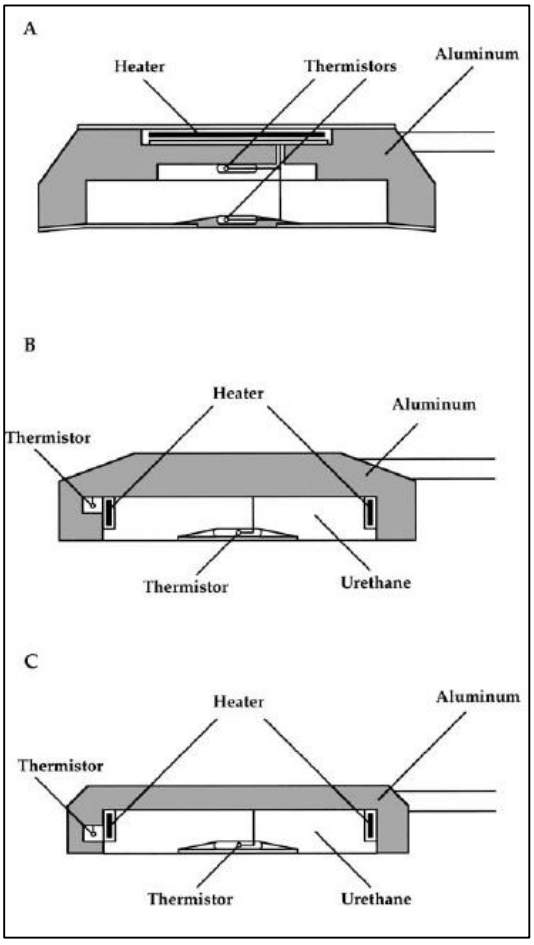

Figure 2-9. Schematic views of improved configurations of Togawa's probe design. Figure 2-9a: The probe is covered with an aluminum guard to minimize heat loss; Figure 2-9b: The circumference of the heater is lined with a heater rather than being placed in the conventional location of being atop the foam. Figure 2-9c: Same design as b, but the heat capacity, weight, and thickness of the probe have been reduced for a quicker temperature response.

2.4.1 Rationale for forehead location for probe placement

To assess for the non-intrusive location for the determination of the core temperature, a study conducted by Matsukawa, Sessler, Ozaki, et al. [15] used a commercialized Terumo temperature probe on the sternum and on the forehead, and compared the readings with a reference temperature defined as that of the esophagus. The forehead was chosen to its close proximity to the carotid artery where the body core temperature can be measured with high accuracy as shown in Figure 2-11. The study consisted of 20 patients under general anesthesia for lower-abdominal gynecological procedures lasting for at least two hours. A Terumo thermometer of 25 mm diameter was affixed to the middle of the sternum or to the mid-forehead during anesthetic induction. The accuracy of the Terumo thermometer had to be within 0.5ºC of the reference temperature to be clinically relevant. Approximately 170 temperature sets were recorded, and the esophageal temperatures ranged from 34.5 to 37ºC over the two hours. Figure 2-10 shows the Bland and Altman analyses for the sternum and forehead data.

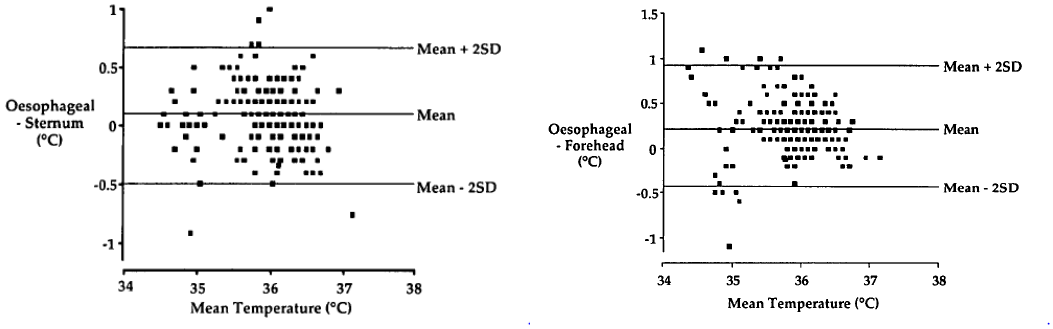

Figure 2-10. Bland and Altman type comparison of esophageal temperatures with sternum and forehead - Matsukawa, Sessler, Ozaki, et al. [15]

The foregoing figures display the difference between the esophageal temperatures and the test site of either the sternum or forehead on the ordinate axis. The abscissa axis shows the mean temperature between the esophageal and test site. The conclusion drawn by the authors of the study is that the use of deep tissue monitoring at the sternum and forehead are both adequate for clinical use since those temperatures were within 0.5ºC of the reference temperature.

Another study conducted by Harioa, Masukawa, Ozaki et al. [17] evaluated the accuracy and precision of the forehead temperature measurement and compared it with blood temperature that served as the reference. As in the previous study performed by Matsukawa, Sessler, Ozaki, et al.[15], the Terumo temperature probe was used as the measuring device for the forehead. The objective was to determine if the core temperature could be measured at the forehead within 0.5ºC of the reference temperature. The study consisted of 41 patients undergoing abdominal and thoracic surgery under general anesthesia for at least three hours. The probe was securely placed on the forehead with tape 20 minutes before anesthesia induction; and the blood temperature was measured with a thermistor in the pulmonary artery catheter. Results show that the blood temperatures ranged from 33.3º to 37ºC, and the forehead measurement correlated well and within the prescribed 0.5ºC.

The studies described in the preceding paragraphs appear to support the forehead as a suitable site for measuring the core temperature. There is, however, some uncertainty in their findings. The study by Matsukawa and co-workers [15] explicitly stated that the placement of the temperature probe was at the *mid-forehead*, whereas the precise placement of the probe in the Harioa study [17] was not specified. In the view of the present writer, a better placement might have been at the lateral edges of the forehead since the carotid artery passes beneath those locations. However, this issue must remain moot since insufficient evidence is not available for resolving it.

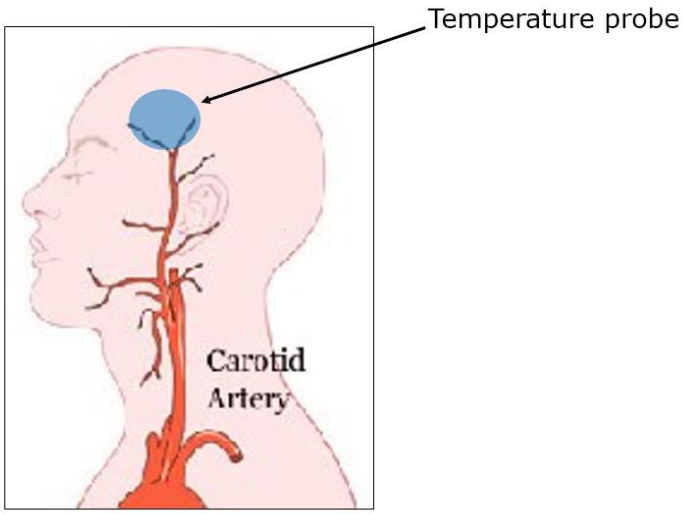

Figure 2-11. Location of temperature probe on the lateral sides of the forehead.

2.5 Physical modeling of forehead and probe assembly

The selected model of the forehead consists of four tissues layers, including the outer skin, inner skin, fat, and bone as shown in Figure 2-12. The probe assembly is placed in intimate contact on top of the skin layer. The figure identifies the various layers and includes the relevant boundary conditions.

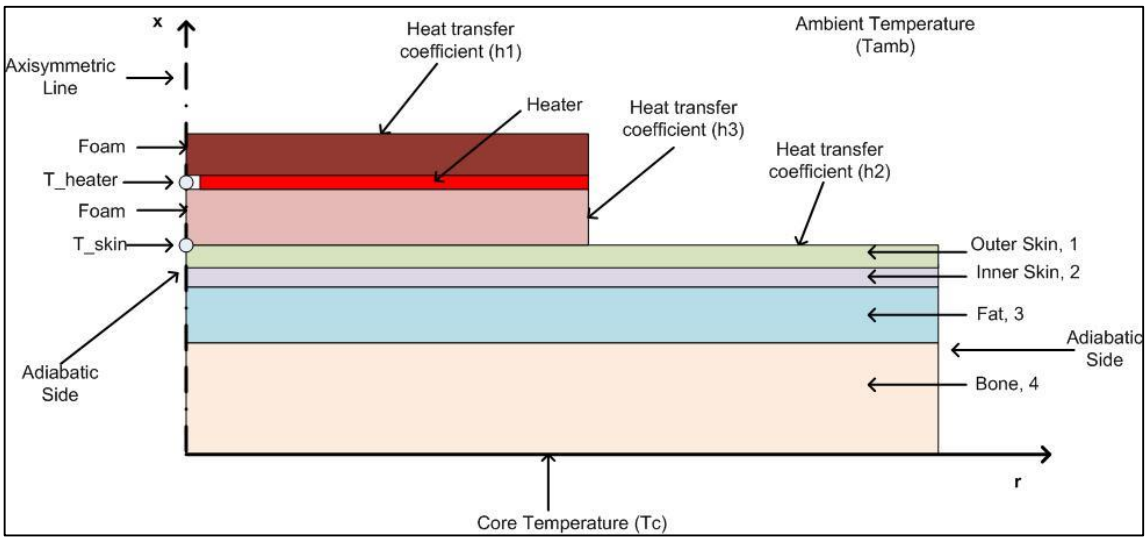

Figure 2-12. Model of the tissue layers with attached probe assembly.

2.6 Governing equations

A numerical simulation model of the tissue bed pictured in Figure 2-11 was developed here based on the Pennes bioheat transfer equation [18]

$$(\rho c)_i \frac{\partial T_i}{\partial t} = k_i \left[\frac{1}{r}\frac{\partial}{\partial r}\left(r\frac{\partial T_i}{\partial r}\right) + \frac{\partial^2 T_i}{\partial x^2}\right] + \omega_i(\rho c)_b(T_a - T_i) + Q_{m,i} \qquad (2\text{-}1)$$

where ρ_i, c_i, and k_i are the density, specific heat, and thermal conductivity of the tissue layer i. In addition, ω_i is the volumetric blood perfusion rate per unit tissue volume, and $Q_{m,i}$ is the volumetric rate of metabolic heat production in each layer. Other symbols include T_i, the temperature of tissue i, and T_a, the arterial blood temperature. The subscript i in Equation (2-1) identifies the four layers of tissues of outer skin (1), inner skin (2), fat (3), and bone (4) in Figure 2-11.

The simulation model also encompasses the probe assembly. The assembly has three distinct layers including two disk-like pieces of insulation and the heater which is placed in-between the two. The heater is modeled as an applied heat flux for the assembly. The heat transfer within each of the insulation layers utilizes the First Law of Thermodynamics combined with the Fourier law of conduction, stated below

$$(\rho c)_f \frac{\partial T_f}{\partial t} = k_f \left[\frac{1}{r}\frac{\partial}{\partial r}\left(r\frac{\partial T_f}{\partial r}\right) + \frac{\partial^2 T_f}{\partial x^2}\right] \qquad (2\text{-}2)$$

where k_f , ρ_f, and c_f are properties of the foam disks. The heater is prescribed as a heat flux modeled at the interface between the foam layers.

The Pennes equation [18] was originally used to predict temperature fields in the human forearm. It is a modification of the conventional heat conduction equation with added terms representing perfusion and metabolic heat generation. The profusing blood is modeled as an isotropic heat source/sink and is proportional to the blood perfusion rate.

The energy carried by the profusing blood is proportional to the difference between the arterial and the local tissue temperatures. This equation has been a useful and successful tool for bio-heat analyses. The use of the Pennes equation has led to good agreements between its temperature predictions and those of experiments in kidney cortexes [19], in the canine brain [20], and in canine prostates [21].

To facilitate the analysis, the assemblage of tissue and non-tissue layers displayed in Figure 2-11 is regarded as stack of plane layers. For this planar model to be a valid representation, it is necessary that the total thickness of the tissue assemblage be small compared to the radius of the head assumed to be sphere. The total thickness of the tissue layers is approximately 10 mm, while the radius of a normal adult head is about 100 mm [23]. This order of magnitude difference is sufficient to validate the plane-layer model.

2.6.1 Solution domain

The solution domain is modeled as a cylinder whose axis is perpendicular to the upper skin layer. The cylinder can be envisioned as consisting of an array of disks each of which corresponds to a tissue layer or an element of the probe. The outer radius of the cylinder was chosen to be large enough so that the presence of the probe does not interfere with the axial heat flow at that radius. Therefore, at radii beyond that corresponding to the outer radius of the cylinder, it is appropriate to assume that radial variations of the temperature vanish. This assumption is equivalent to an adiabatic boundary at the cylinder outer radius. That outer radius is not known *a priori*; it will be found during the course of the numerical solutions. Initially, it will be assumed that the critical radial distance is equal to twice the radius of the probe.

2.6.2 Material properties and boundary conditions

The research of Weinbaum and colleagues [22] found that the differences in the anatomy of the blood vessels in the various layers of tissue affect heat transfer. For the outer layer of skin, there is no perfusion there because there are no blood vessels. At the exposed

surface of the skin, there is heat loss by both radiation and convection. To deal with these heat transfer mechanisms, the model will be based on a literature value of heat transfer coefficients for natural convection. That model also will include a radiation contribution whose magnitude will be developed here from first principles. For each tissue-tissue interface, both the temperature and heat flux are continuous. At the base of the lowest tissue layer, the normothermic 37ºC temperature will be imposed. Furthermore, the arterial blood temperature is assumed to have a constant value equal to 37ºC. Table 2-1 displays the thickness of the individual layers and their material properties.

Table 2-1. Material properties of bone, fat, skin, blood and foam and their thicknesses [23, 50].

	t (mm)	k (W/m K)	c (J/kg K)	ρ (kg/m^3)	Q_m (W/m^3)	ω (kg/m^3 s)
Bone	5.4	1.0	1700	1500	130	0.15
Fat	3.0	0.2	2390	1050	130	0.2
Inner skin	1.0	0.384	3570	1130	500	1.5
Outer skin	1.0	0.384	3570	1130		
Blood			3800	1050		
Foam	5.0	0.045	1400	123		

In the present configuration, the diameter of the assembled probe is 41 mm which aligns closely with Togawa's commercially released probe diameter of 45 mm [10]. The top and bottom foam thicknesses are 2 and 3 mm respectively. The diameter and total thickness dimensions are acceptable from the standpoint of not being overly intrusive when placed on the forehead.

2.7 Natural convection heat loss mechanism

A combined convection and radiation boundary condition is applied to the exposed surfaces of the probe and skin. In the environment in which the probe will be used, it is expected that there would be a minimum level of air movement. For this situation, fluid motion is not generated by any external source such as a fan or blower, but only by density differences in the fluid due to temperature gradients. The fluid velocity at points

remote from the probe and forehead will be zero. In the air near the probe and skin, there will be fluid motion if there is a temperature difference between these surfaces and the ambient. This motion occurs because of density differences caused by the aforementioned temperature differences. The buoyant force can create motions in different directions depending on whether the surface temperature either exceeds or is less than the ambient and on the direction of the gravity force. In principle, natural convection is a non-linear function of the temperature difference between the surface and the fluid. However, since the temperature differences in the present situation are small, the non-linearity has no material effect. An illustration of natural convection motion is presented in Figure 2-13.

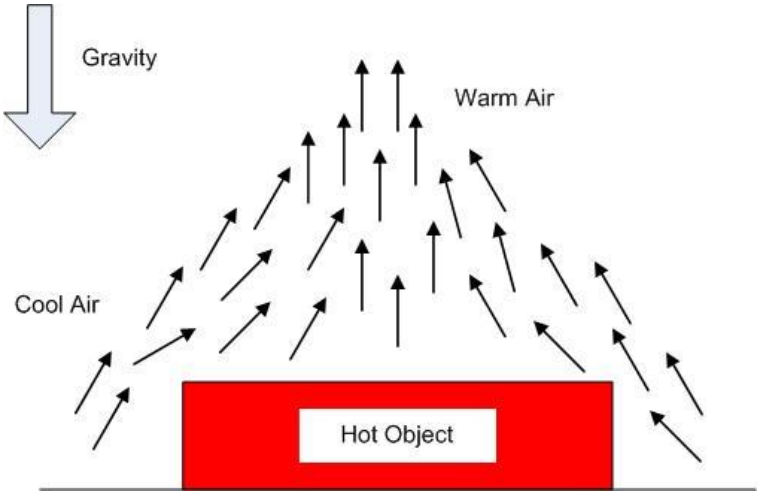

Figure 2-13. A representative depiction of the natural convection process.

For the natural convection situation that is relevant here, a well-accepted correlation is used to obtain the heat transfer coefficient. That equation is

$$\overline{Nu}_f = C(Gr_f Pr_f)^m \qquad (2\text{-}2)$$

where $\overline{Nu}_f$ is the surface-average Nusselt number, Gr_f is the Grashof number, Pr_f is the Prandtl number, and C and m are constants [24]. The f subscript indicates that the

properties in dimensionless groups are evaluated at the film temperature which is the average of the ambient and surface temperatures. The characteristic dimension to be used in the Nusselt and Grashof numbers depends on the geometry at hand.

For vertical surfaces, the height L of the surface is the characteristic dimension. Past research has shown that when the boundary-layer thickness is small compared with the diameter D of a cylinder, the heat transfer for a cylinder may be calculated using equations for vertical plates. The criterion to treat a cylinder as a vertical plate [25] is defined by the following criterion

$$\frac{D}{L} \geq \frac{35}{Gr_L^{1/4}} \qquad (2\text{-}3)$$

The Grashof number definition equation for vertical cylinders treated as a flat plate is

$$Gr_L = \frac{g\beta(T_s - T_\infty)L^3}{\nu^2} \qquad (2\text{-}4)$$

This equation is the ratio of buoyancy to viscous forces, where g is gravity, β is the thermal expansion coefficient, T_s is the surface temperature, T_∞ is the ambient temperature, and ν is the kinematic viscosity. For a vertical surface, the heat transfer coefficient for natural convection is obtained by evaluating

$$\frac{\bar{h}L}{k_f} = \overline{Nu}_f = 0.59(Gr_f Pr_f)^{1/4} \qquad (2\text{-}5)$$

where k_f is the conductivity of the fluid, and $\bar{h}$ is the average natural convection heat transfer coefficient [26-29].

For horizontal surfaces, correlations exist for both air heated from below and heated from above. The present horizontal surface corresponds to the heated from below category, so

that the equation to be used to calculate the heat transfer coefficient for natural convection is [30, 31]

$$\frac{\bar{h}L}{k_f} = \overline{Nu}_f = 0.54(Gr_f Pr_f)^{1/4} \qquad (2\text{-}6)$$

Equation (2-6) is similar to Equation (2-5) except that the characteristic dimension L is defined as the surface plane area divided by the perimeter that bounds the area.

2.8 Radiation heat loss mechanism

To obtain the heat transfer by radiation, the exposed surfaces of the probe are regarded as a hot object that is radiating energy to its cooler surroundings. Since the air is transparent to thermal radiation, the surroundings constitute all the surfaces in the space in which the patient is situated. Figure 2-14 presents a schematic diagram for the analysis of the radiation heat transfer at the exposed surfaces of the probe and skin. For the analysis, it is advantageous to create an enclosure to facilitate taking account of all radiation streams as shown in Figure 2-14, the enclosure for the present analysis consists of physical walls, forehead, and probe. For small temperature difference, radiation can be linearized.

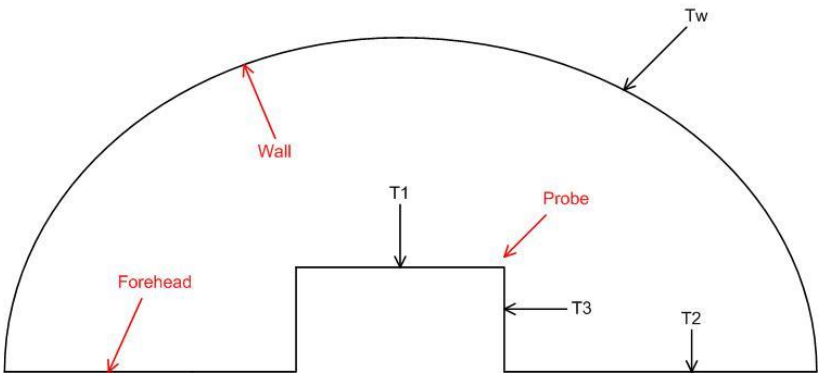

Figure 2-14. Radiation schematic of the model comprising the four participating surfaces where, T is the temperature of the surfaces.

It is assumed that each of the participating surfaces has a uniform temperature, but each has a different temperature. The probe is comprised of both surfaces 1 and 3 while the forehead is surface 2. The radiation incident on surface 1 is only influenced by the surrounding physical walls, while surfaces 2 and 3 are influenced by each other and by the surrounding surfaces. The radiation analysis is performed by making use of the radiosity method. The radiosity *r* is the rate at which radiant energy leaves a surface per unit area. It consists of the sum of two components: emission and reflection. The emission per unit area is given by

$$\epsilon_j \sigma T_j^4 \qquad (2\text{-}7)$$

in which ϵ_j is the emissivity of the surface, σ is the *Stefan-Boltzmann constant* (whose value is $5.7*10^{-8}$ W/m^2K^4), and T_j is the absolute temperature of the surface. The subscript *j* identifies the surface in question. The other component of the radiosity, the reflection radiation per unit time and area, is

$$\rho_j i_j \qquad (2\text{-}8)$$

in which ρ_j is the reflectivity of surface *j*, and i_j is the rate at which radiation arrives at j per unit area.

To determine the rate of heat transfer at any surface *j*, it is convenient to draw an observation line slightly displaced above the surface as depicted in Figure 2-15. The

radiant energy leaving the surface per unit time and area is depicted by the radiosity *r*. The quantity *i* denotes the rate at which radiation arrives at the surface per unit area. The rate of heat transfer per unit area *q* at the surface *j* follows as

$$q_j = r_j - i_j \qquad (2\text{-}9)$$

and for a surface area A_j , the overall rate of heat transfer Q_j is

$$Q_j = q_j * A_j \qquad (2\text{-}10)$$

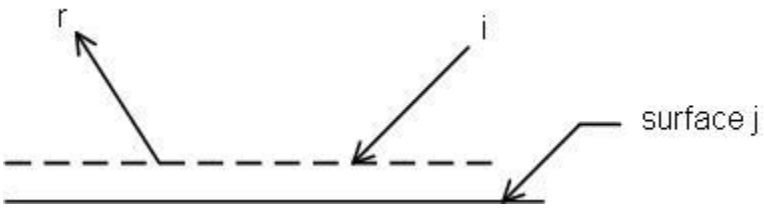

Figure 2-15. Schematic diagram to illustrate the evaluation of the rate of heat transfer at a surface *j*.

The foregoing methodology will now be applied to the surface *j = 1*. Observation of Figure 2-14 indicates that the radiation incident on surface 1 originates from the external surfaces whose temperature is T_w. Regardless of the actual emissivity of those surfaces, there is a theorem that states that if the surfaces that form an enclosure are isothermal, the radiation streaming within the enclosure is black body radiation σT_w^4. In the present instance, the requirements for the validity of theorem are not precisely fulfilled.

However, since the external radiating surroundings have a surface area that is much greater than the combined surface areas of 1, 2, and 3, it is deemed sufficient to use the theorem. Therefore, i_1 is equal to σT_w^4. The radiosity r_1 can be written as

$$r_1 = \epsilon_1 \sigma T_1^4 + \rho_1 i_1 \qquad (2\text{-}11)$$

In general, the reflectivity ρ is equal to $(1 - \alpha)$ for an opaque surface, where α is the absorptivity. There are no tables of α in the literature, but it can be argued that $\alpha = \epsilon$ if the emitted and incident radiations span the same range of wavelengths. This condition is fulfilled in the present situation, enabling the elimination of ρ_1 from Equation (2-11) in favor of $(1 - \epsilon)$. Finally, the rate of heat transfer at surface 1 can be obtained from Equations (2-9), (2-10), and (2-11) as

$$Q_1 = A_1[\epsilon_1 \sigma T_1^4 + (1 - \epsilon_1)\sigma T_w^4 - \sigma T_w^4] = \epsilon_1 \sigma (T_1^4 - T_w^4) A_1 \qquad (2\text{-}12)$$

To extract a radiation heat transfer coefficient from Equation (2-12), it is appropriate to use the definition

$$(Q_1)_{rad} = \bar{h}_{rad,1} A_1 (T_1 - T_w) \qquad (2\text{-}13)$$

When this defining equation is combined with Equation (2-12), there results

$$\bar{h}_{rad,1} = \frac{\epsilon_1 \sigma (T_1^4 - T_w^4)}{(T_1 - T_w)} \qquad (2\text{-}14)$$

When the difference between the values of T_1 and T_w is very small, the binomial theorem can be used, giving

$$(T_1^4 - T_w^4) = 4(T_1 - T_w)\overline{T^3} \qquad (2\text{-}15)$$

With this, Equation (2-14) becomes

$$\bar{h}_{rad,1} = 4\epsilon_1 \sigma \overline{T^3} \qquad (2\text{-}16)$$

For foam, $\epsilon_1 \sim 0.9$. Also, $\overline{T} = \frac{1}{2}(T_1 + T_w) = \frac{1}{2}[(273.15 + 37) + (273.15 + 20)] = 301.65K$. The introduction of the values of σ, ϵ_1, and $\overline{T}$ into equation (2-16) yields $\bar{h}_{rad,1} = 5.6 \frac{W}{m^2 K}$.

For surface 2, the incident radiation i_2 has both contributions from surface 3 and from the surrounding environment. To determine the contributions from surface 3, it is first necessary to quantify the radiosity r_3 of the latter surface. The radiation leaving surface 3 in all directions is $r_3 A_3$. From Figure 2-13, it is clear that only a fraction of that radiation will arrive at surface 2. The theory of thermal radiation uses a view factor to quantify the

fraction of radiation leaving a surface *k* that arrives at surface *j;* that view factor is written as F_{k-j}. Another corollary from radiation theory is called the Reciprocity Rule, which states

$$A_k F_{k-j} = A_j F_{j-k} \qquad (2\text{-}17)$$

With the use of the view factor F_{k-j}, the radiation leaving surface 3 and arriving surface 2 is $r_3 A_3 F_{3-2}$. In addition, the radiation arriving at surface 2 from the surroundings is $\sigma T_w^4 A_2$. When these contributions are added, there results

$$A_2 i_2 = r_3 A_3 F_{3-2} + \sigma T_w^4 A_2 \qquad (2\text{-}18)$$

It is convenient to simplify Equation (2-18) by using the reciprocity rule, the application of which leads to

$$i_2 = r_3 F_{2-3} + \sigma T_w^4 \qquad (2\text{-}19)$$

Next, the radiosity of surface 2 is written as

$$r_2 = \epsilon_2 \sigma T_2^4 + \rho_2 i_2 = \epsilon_2 \sigma T_2^4 + (1 - \epsilon_2)(r_3 F_{2-3} + \sigma T_w^4) \qquad (2\text{-}20)$$

By the combination of Equations (2-19) and (2-20), the rate of heat transfer at surface 2 follows as

$$(Q_2)_{rad} = A_2[\epsilon_2 \sigma T_2^4 + (1 - \epsilon_2)(r_3 F_{2-3} + \sigma T_w^4) - r_3 F_{2-3} - \sigma T_w^4] \qquad (2\text{-}21)$$

To complete Equation (2-21), the radiosity r_3 is needed

$$r_3 = \epsilon_3 \sigma T_3^4 + \rho_3 i_3 = \epsilon_3 \sigma T_3^4 + (1 - \epsilon_3)[r_2 F_{3-2} + \sigma T_w^4] \qquad (2\text{-}22)$$

Note that when Equation (2-22) is substituted into Equation (2-21), the resulting equation contains three temperatures T_2, T_3, and T_w. If it is desired to transform the equation for $(Q_2)_{rad}$ into a form involving a radiation heat transfer coefficient and a difference between two temperatures, the presence of the aforementioned three temperatures provides a roadblock. To gain perspective about this possible dilemma, it is appropriate to quantify the relative magnitudes of the respective contributions of the environmental radiation and the radiation from surface 2 to $(Q_2)_{rad}$. Inspection of the geometry of the situation (Figure 2-14) suggests the view factor $F_{2\text{-}3}$ must be much less than 1. To this end, a search was made of the available view factor tabulations. That search provided Figure 2-16 and the accompanying Equation (2-23). With respect to the figure, the vertical cylinder corresponds to surface 2 and the plane annulus represents surface 3. When the appropriate dimensions are introduced into Equation (2-23), it is found that $F_{2\text{-}3}$ = 0.028. This very small view factor value suggests that the impact of the radiation arriving at surface 2 from surface 3 can be neglected. When this conclusion is implemented in Equations (2-21) and (2-22), there follows

$$(Q_2)_{rad} = A_2[\epsilon_2 \sigma T_2^4 + (1 - \epsilon_2)\sigma T_w^4 - \sigma T_w^4] = \epsilon_2 \sigma (T_2^4 - T_w^4) A_2 \qquad (2\text{-}23)$$

Since this equation is identical in form to Equation (2-12) after appropriate changes of subscripts, the mathematically development described subsequent to Equation (2-12) follows without modification and leads to $\bar{h}_{rad,2} = 5.6 \frac{W}{m^2 K}$.

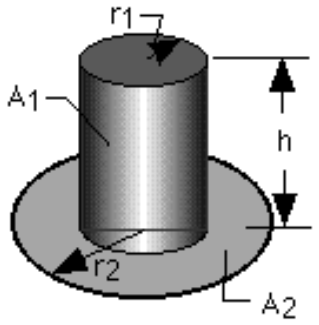

Figure 2-16. View factor for finite area of an outer surface of a cylinder to the finite area of an annular disk at the bottom of the cylinder [36].

The governing equation for the view factor in Figure 2-16 is [36]

$$F_{1-2} = \frac{B}{8RH} + \frac{1}{2\pi}\left\{cos^{-1}\left(\frac{A}{B}\right) - \frac{1}{2H}\left[\frac{(A+2)^2}{R^2} - 4\right]^{\frac{1}{2}} \times cos^{-1}\left(\frac{AR}{B}\right) - \frac{A}{2RH}sin^{-1}R\right\} \qquad (2\text{-}23)$$

where $R = r_1/r_2$, $H = h/r_2$, $A = H^2 + R^2 - 1$, *and* $B = H^2 - R^2 + 1$

The use of the same thought process as before leads to the radiation arriving at surface 3 as

$$i_2 = r_2 F_{3-2} + \sigma T_w^4 \qquad (2\text{-}24)$$

where $F_{2\text{-}3}$ is, in terms of the notation of Figure 2-15, equal to $F_{1\text{-}2}$.

By the use of Equation (2-22) for the radiosity for surface 3 and Equation (2-24) for the incident radiation, the rate of heat transfer at surface 3 is

$$(Q_3)_{rad} = A_3[\epsilon_3 \sigma T_3^4 + (1-\epsilon_3)(r_2 F_{3-2} + \sigma T_w^4) - r_2 F_{3-2} - \sigma T_w^4] \qquad (2\text{-}25)$$

where r_2 is provided by Equation (2-20), $\epsilon_3 \sim 0.9$ for skin, and $F_{3\text{-}2}$ is 0.465 from Equation (2-23).

Furthermore, $(Q_3)_{rad}$ may be equated to

$$(Q_3)_{rad} = \bar{h}_{rad,3} A_3 (T_3 - T_w) \qquad (2\text{-}26)$$

which leads to a radiation heat transfer coefficient at surface 3 as $\bar{h}_{rad,3} = 7.1 \ \frac{W}{m^2 K}$.

The overall heat transfer coefficient for the surfaces in question is then obtained by summing up the natural convection and radiation coefficients, with the outcome

$$\bar{h}_{total} = \bar{h}_{nat\ conv} + \bar{h}_{rad} \qquad (2\text{-}27)$$

2.9 Heaters

Simulations of the probe design will include either one or two heaters as shown in Figure 2-17. In both cases, the heat flux at each heater will be assumed to be steady and uniform, but the not necessarily the same values. Two temporal conditions will be investigated: steady-state and transient. The numerical simulations were performed for both of the heater configurations, while the experimental work was carried out for the two-heater setup because it provided a more demanding situation for the validation of the simulation results.

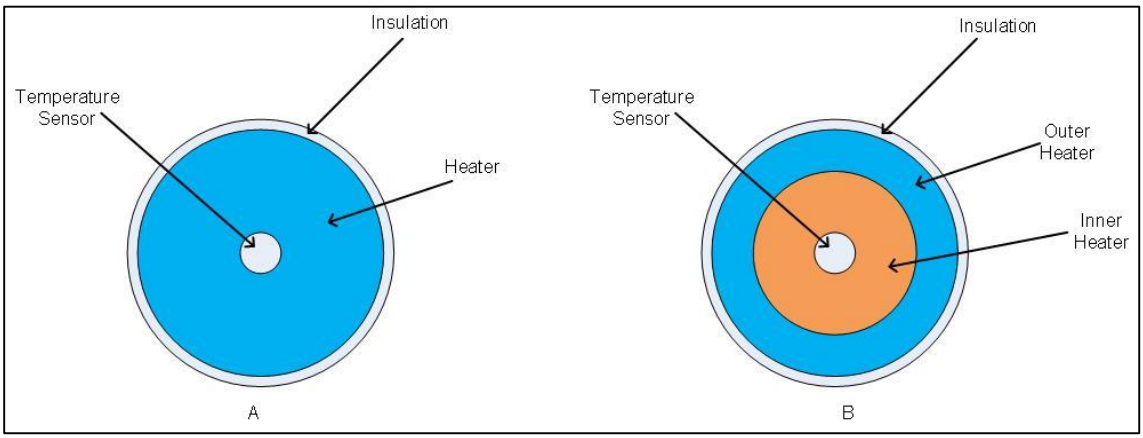

Figure 2-17. Views of heaters

a. Schematic of single heater, b. Schematic of two independently wired heaters.

2.10 Numerical solutions

The governing differential equations, namely Equations (2-1) and (2-2), were discretized by the finite volume method. Subsequent to the discretization and meshing, the solution domain encompassed 1.5 million nodes. Mesh independence was established by running selected cases making use of 2.5 million nodes. The difference between the skin surface temperatures predicted by these differently composed meshes was less than 0.01^{o}C.

The actual numerical solutions were obtained by means of a commercial software package ANSYS CFX 14.0. A single computer run for the transient situation required approximately two days for completion; a substantially shorter time was sufficient for the steady-state simulations.

2.11 Numerical solutions protocol

Numerical solutions for both the one- and two- heater designs were obtained. For both cases, a uniform heat flux is prescribed for each of the heaters. In the case of two heaters, each of the heaters has a different uniform heat flux. Figure 2-18 displays an overview of the scenario used to achieve the predicted skin temperature (T^*) with the heat flux as a prescribed input.

2.11.1 One-heater case

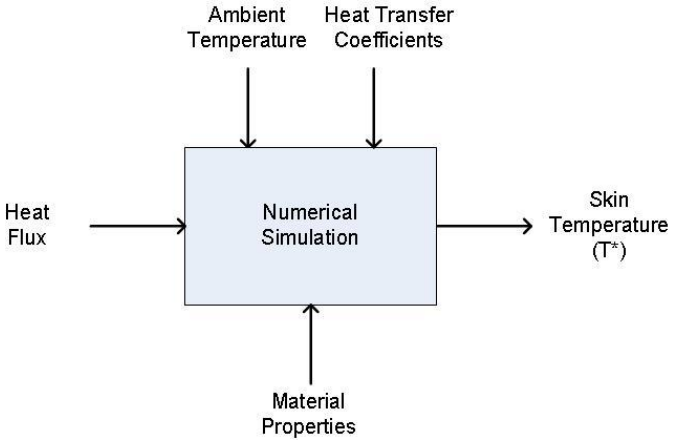

Figure 2-18. Simulation schematic that shows input parameters to achieve an output value for the skin temperature for the one-heater case.

The strategy to solve the numerical simulation is an *inverse method* using an iterative process. The current situation is ill-posed in that the unknown is the rate of heat input. The objective is to minimize the difference between the predicted skin temperature and the assigned 37^{o}C core temperature. The data inputs to the numerical simulation are ambient and core temperatures, heat transfer coefficients, material properties, and tentative heat flux values while the output is the skin temperature.

A training period was pursued to establish a qualitative relationship between incremental changes of heat flux and corresponding changes of the predicted skin temperature. Subsequently, the input-output sequence connecting the heat flux and the skin temperature was automated. A graph of T_{skin} versus heat flux was generated to be used in the feedback loop system to determine the heat flux.

The computational scheme for the one-heater case is shown in Figure 2-19.

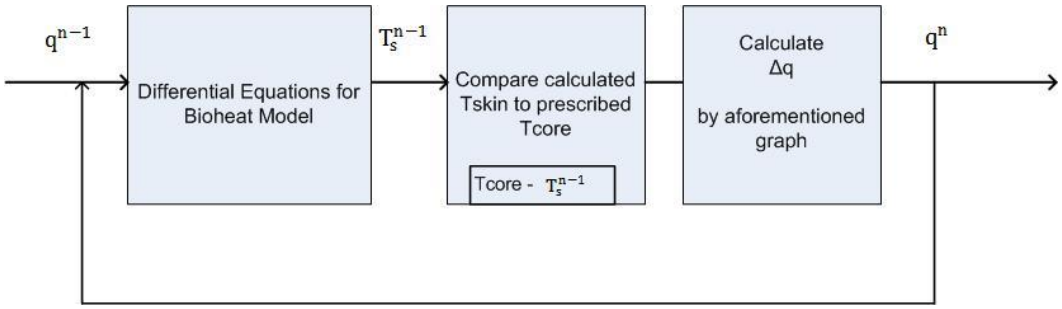

Figure 2-19. Computational schematic to solve for heat flux values to match skin to core temperature where q is the heat flux and T_s is the calculated skin temperature at the probe axis.

For the first iteration, the heat flux value was taken to be zero. The approach is to increase the heat flux value until the skin and core temperatures match. The heat flux value is used as input for the heat conduction model, and the output of the model is a skin temperature. The skin temperature is then compared to the core temperature and the difference is computed. If the temperature difference is greater than the prescribed tolerance, then the next iteration is executed with a new heat flux value. The graph created during the training period is used to assist computing a new heat flux value. The next heat flux value is computed by using the algorithm

$$q^n = q^{n-1} + \Delta q \qquad (2\text{-}28)$$

The change in heat flux is then computed through Equation (2-29)

$$\Delta q = \frac{dq}{dT_s}(T_s^n - T_s^{n-1}) \qquad (2\text{-}29)$$

For each new computed heat flux and skin temperature, these values are inputted into the graph created during the training period in order to determine a revised value of $\frac{dq}{dT_s}$ for each iteration run.

To guarantee convergence, it is deemed appropriate to use the method of underrelaxation. To facilitate the description of the method, envision an iterative process in which three

successive iterations are identified by the numbers *(n-1)* and *n*. Let the input to the *(n-1)* iteration be denoted as q_{input}^{n-1} and the output by q_{output}^{n-1}. For ordinary iterations,

$$q_{output}^{n-1} = q_{input}^{n} \qquad (2\text{-}30)$$

However, for a situation prone to instability and divergence, underrelaxation is a mandatory approach. Let Ω be designated at the underrelaxation factor. Then,

$$q_{input}^{n} = q_{input}^{n-1} + \Omega[q_{output}^{n-1} - q_{input}^{n-1}] \qquad (2\text{-}29)$$

The case of Ω = 1 reduces to ordinary iteration. To dampen tendencies toward instability and divergence, let Ω < 1. In fact, it has been the writer's experience that near the initiation of an iterative process, there is a strong tendency for instability to occur. To mitigate this tendency, Ω values as small as 0.01 may be necessary. As the process approaches convergence, larger values of Ω are appropriate.

2.11.2 Two-heater case

For the two-heater system, the scheme is similar to the one-heater case, but the goal of minimizing the radial temperature variation along the skin surface can also be addressed because of the additional degree of freedom afforded by the second heater as shown in Figure 2-20.

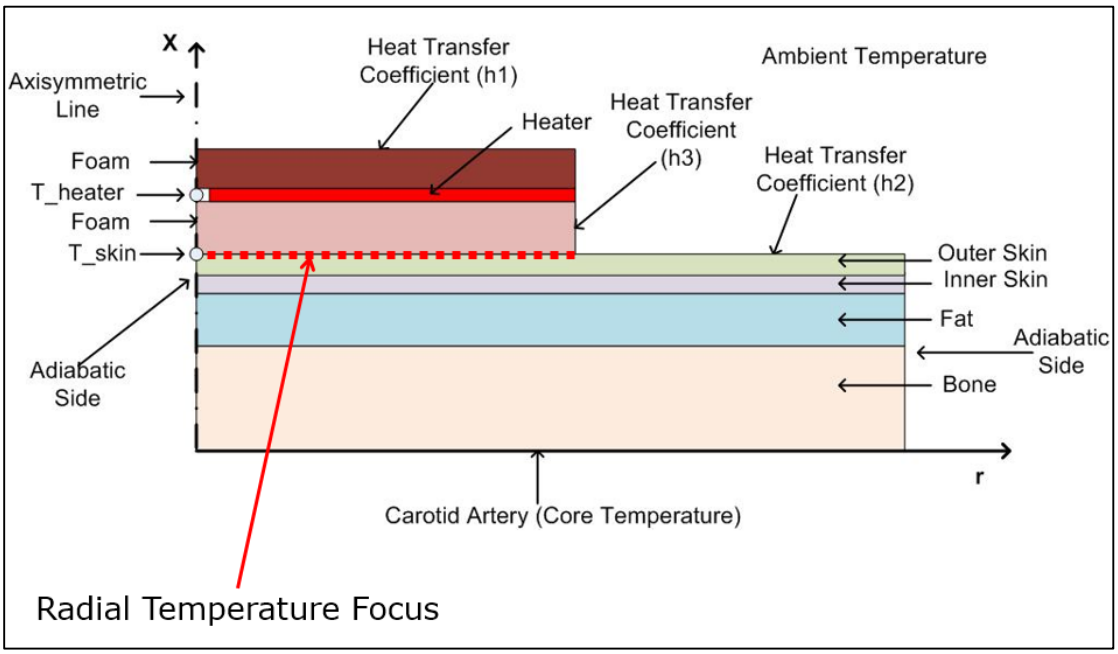

Figure 2-20. Schematic of a two-heater system. The line along which the radial temperature variation is to be minimized is identified in the figure.

The rationale behind the two-heater system is that a higher heat flux on the outer heater compared to the inner one would impede the radial heat loss. The solution scheme for the two-heater case is similar to that for the one-heater case and is shown in Figure 2-21. Since there may be an indefinite number of solutions for the two-heater case, a relationship between the two heaters needs to be established. A training period to establish the relationship between the heaters showed that the heat flux value for the outer heater should not exceed 1.3 times that for the inner heater. The computational scheme for the two-heater case follows that of the one-heater design.

The imposed goal of minimizing the radial temperature variation on the skin surface between the axis of the probe and its outer edge required an additional step in the iteration process. At the end of a given iteration, the skin temperature at the axis T_S was compared with the temperature at the edge of the probe T_R. On the basis of what was learned during the training period, a change in the heat flux for the outer heater was made to diminish the temperature difference $(T_S - T_R)$. This approach proved to be successful.

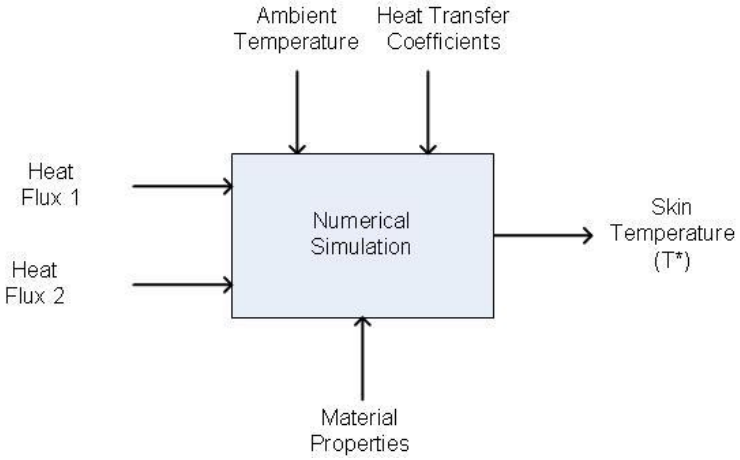

Figure 2-21. Simulation schematic for the two-heater case that shows input parameters to achieve an output value for the skin temperature and the temperature difference (T_S - T_R)

2.12 Results and discussion for a one-heater system

2.12.1 Transient operating scenarios

One operating scenario (Scenario 1) for the use of temperature probe is as follows: prior to the placement of the probe on the forehead of the patient, there is an already established thermal steady state within in the tissue bed behind the forehead. That steady state consists of a core temperature of 37°C and heat loss from the exposed faces of the forehead by natural convection and radiation to a 20°C ambient. Then, a transient is initiated by placing the probe having a temperature of 20°C on the forehead. It was envisioned that prior to its placement on the forehead, the probe had equilibrated with the 20°C environment. At the instant that the probe makes contact with the forehead, heating is initiated immediately. The predicted skin temperature during the transient is displayed in Figure 2-22. As can be seen in the figure, the skin temperature rises quickly at first and then proceeds more slowly to a steady-state value which is achieved after 12 minutes of operation.

It is worthy of note that the time to achieve steady state is affected by the On-Off characteristic of the heater control system. The control algorithm is based on allowing a

temperature difference between the heater and skin thermistors of 0.1°C when the heater temperature is below that of the skin. If this tolerance is exceeded, the heating is initiated. If the skin temperature exceeds that of the heater, no heat is applied.

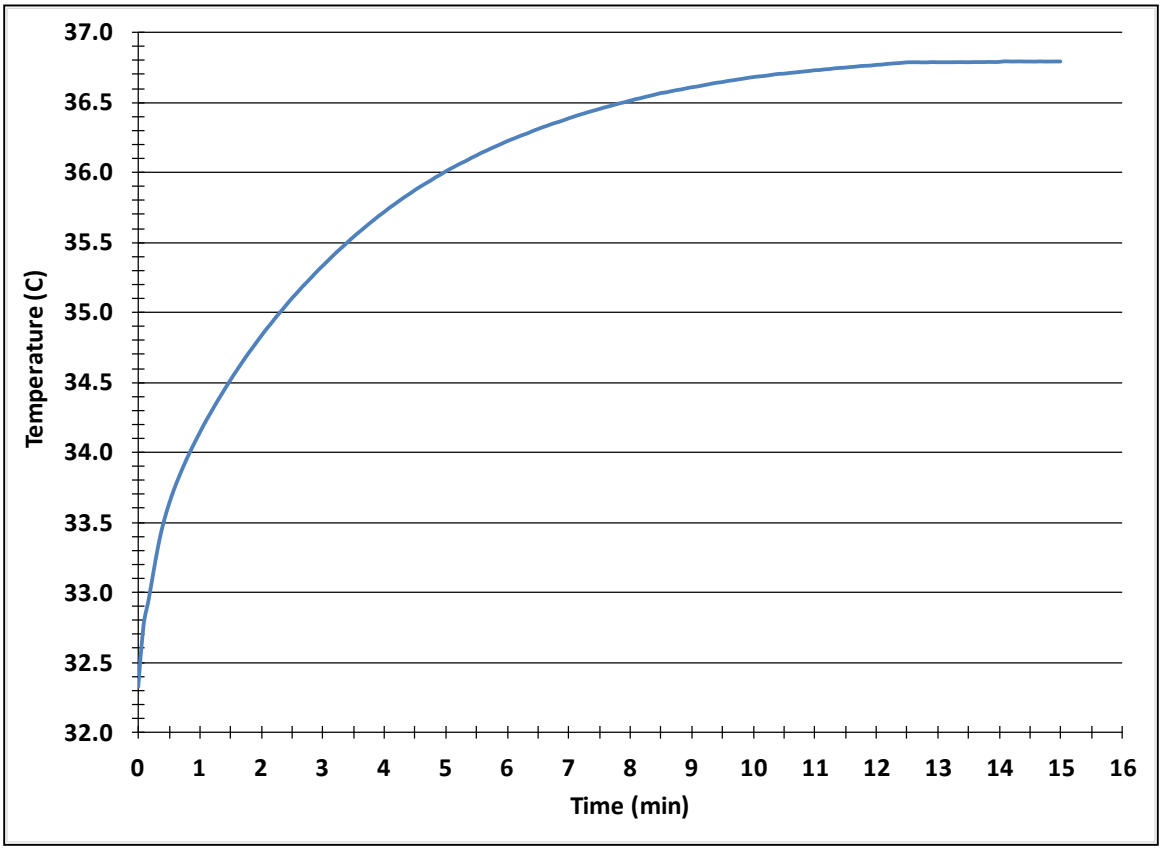

Figure 2-22. Transient variation of the skin temperature corresponding to Scenario 1.

For the second operating scenario (Scenario 2), the probe is envisioned to be in contact with the forehead, but without the heater being functionally involved. The two media, the probe and the tissue bed, are allowed to come to thermal equilibrium under the condition that (a) the temperature is 37°C at the deepest tissue layer, (b) heat loss by natural convection and radiation takes place at the exposed surfaces of the probe and the forehead, and (c) the heater is not activated. Once steady state has been established for the probe-tissue system, the heating function is initiated and heating occurs as governed by the On-Off control algorithm. The transient temperature variation at the skin surface

corresponding to Scenario 2 is displayed in Figure 2-22. Inspection of Figure 2-22 reveals that the transient wanes into steady state after about eight minutes subsequent to the initiation of heating. This performance is, from the standpoint of time to achieve steady state, advantageous compared to that exhibited for Scenario 1.

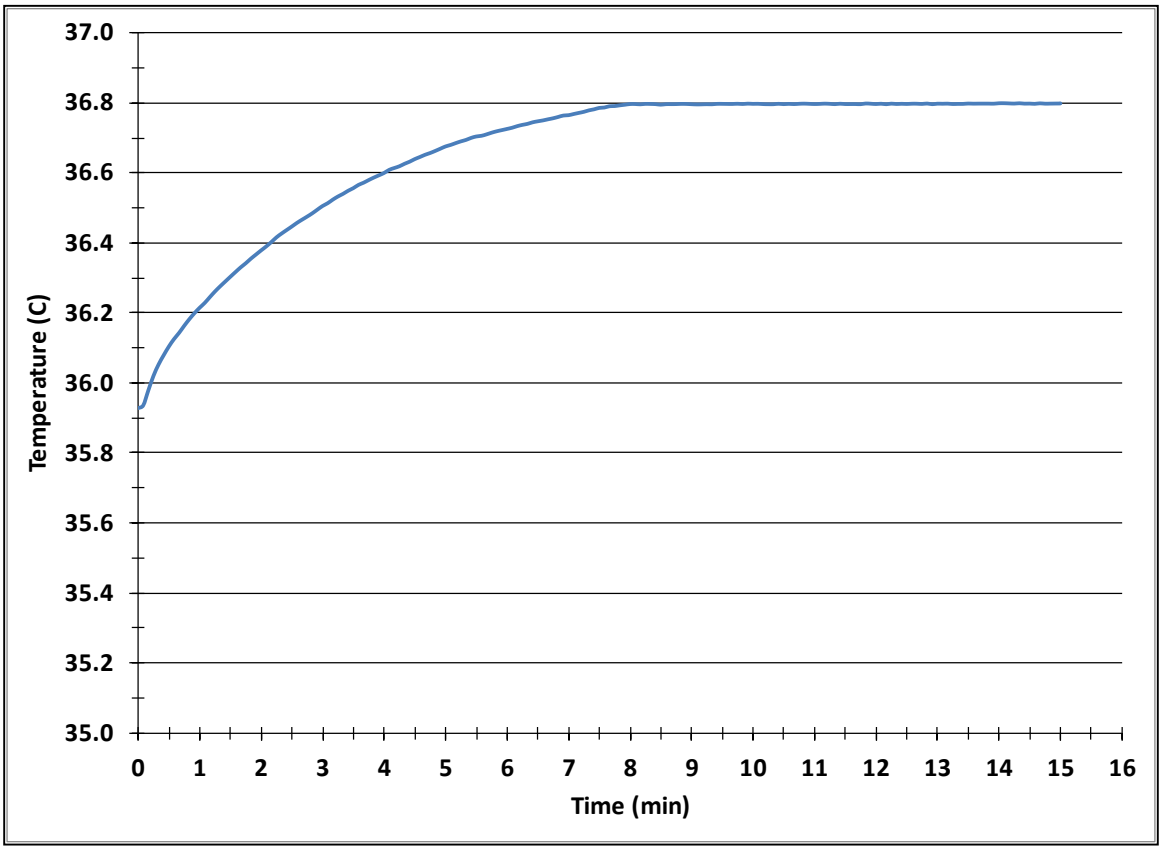

Figure 2-23. Transient variation of the skin temperature corresponding to Scenario 2.

Other scenarios may be envisioned. For example, suppose that the probe, equilibrated to a temperature of 20^{o}C, is put in place on a forehead whose backing tissue is at steady state. However, heating is not initiated immediately but is delayed for an arbitrary period of time which is shorter than that needed for the entire probe-tissue system to achieve steady state. For that situation, the transient behavior of the skin temperature would fall somewhere between the graphical information conveyed in Figures 2-22 and 2-23.

2.12.2 Steady-state results

Both transient scenarios become steady state, as witnessed by Figures 2-22 and 2-23. The details of the steady-state solution will now be conveyed by graphical means. The first figure to be presented, Figure 2-24, is a color contour diagram of the temperature field encompassing both the probe and tissue layers. It can be seen from the figure that the volume occupied by the near-axis portion of the probe and the tissue beneath it experience steady-state temperatures in the range between 36.6 and 37.0°C. This is a very affirmative finding. The skin-surface temperature is contained within that range over the inner half of the probe, but experiences a decrease as the radial distance from the axis increases. Owing to that decrease, the skin temperature variation under the probe ranges from 35.4 to 36.8°C. This variation does not in any way diminish the quality of the information obtained from the probe.

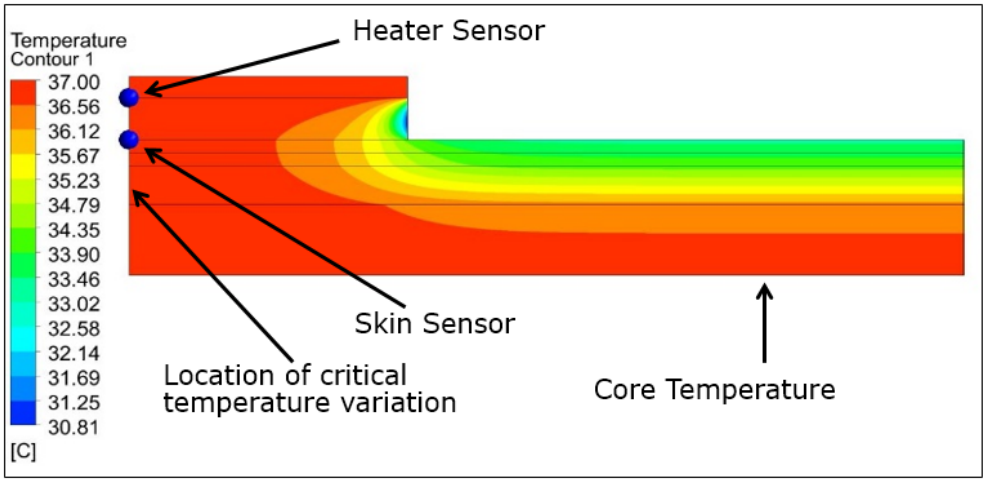

Figure 2-24. Color contour temperature diagram.

Another facet of the steady-state results is the vertical temperature variation over the distance between the lowest tissue layer and the top of the probe. This information is presented in Figure 2-25. The figure shows the vertical-axis temperature variation plotted along the ordinate and the position along the vertical axis is the depicted on the horizontal axis. Overall, the variation extends from 36.8 to 37.0°C. The low point,

36.8°C, occurs at the skin temperature measurement location. In this light, the information provided by the probe is seen to be deviant by 0.2°C from the core temperature. Since the acceptable deviation is 0.5°C [16], the probe performance is acceptable.

Further inspection of Figure 2-25 indicates a sharp break in the slope of the temperature distribution at the interface between the bone and fat layers. This discontinuity can be attrributed to a large change in the thermal conductivities of these media. Also in evidence is slight rise in temperature between the bottom and top surfaces of the probe. This occurrence is due to the presense of the heater.

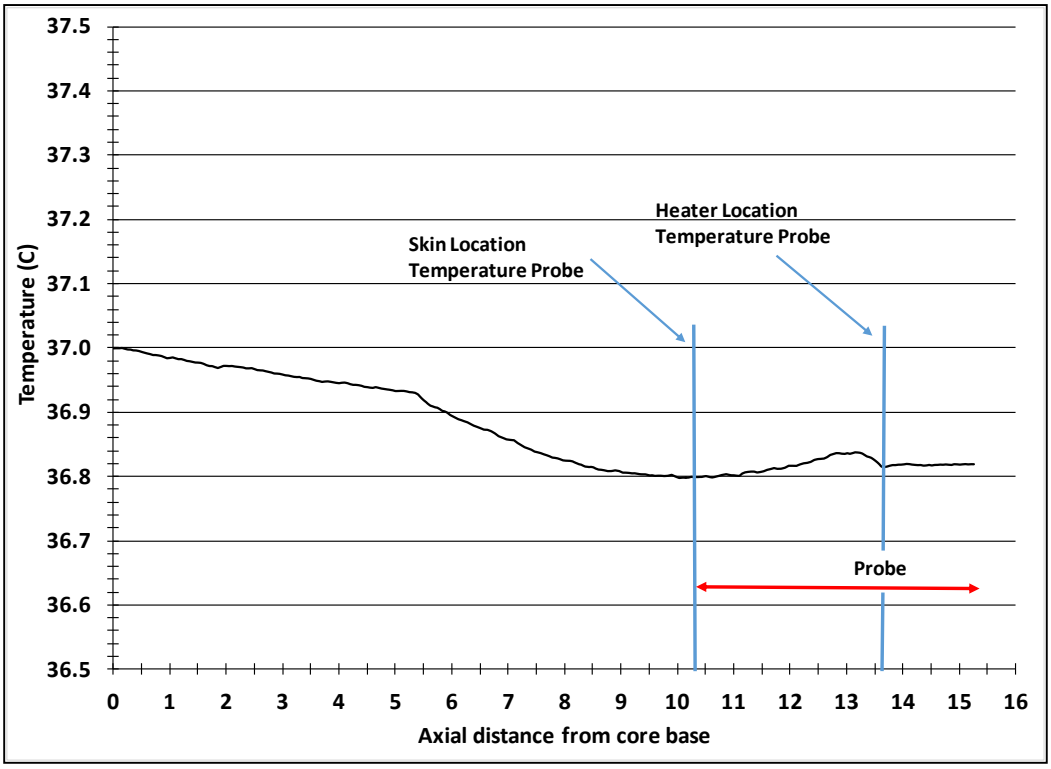

Figure 2-25. Temperature distribution along the vertical axis from the lowest layer of tissue to the top of the probe.

To complement the axial temperature variation conveyed in Figure 2-25, the radial variation of the temperature along the skin surface will be shown in Figure 2-26. It can

be seen that the temperature decreases monotonically across the radial extent of the probe, with the range being from 36.8 to 35.4°C. The decrease continues but with diminishing slope out to a radial coordinate of 35 mm. At the latter location, the temperature is 33.3°C.

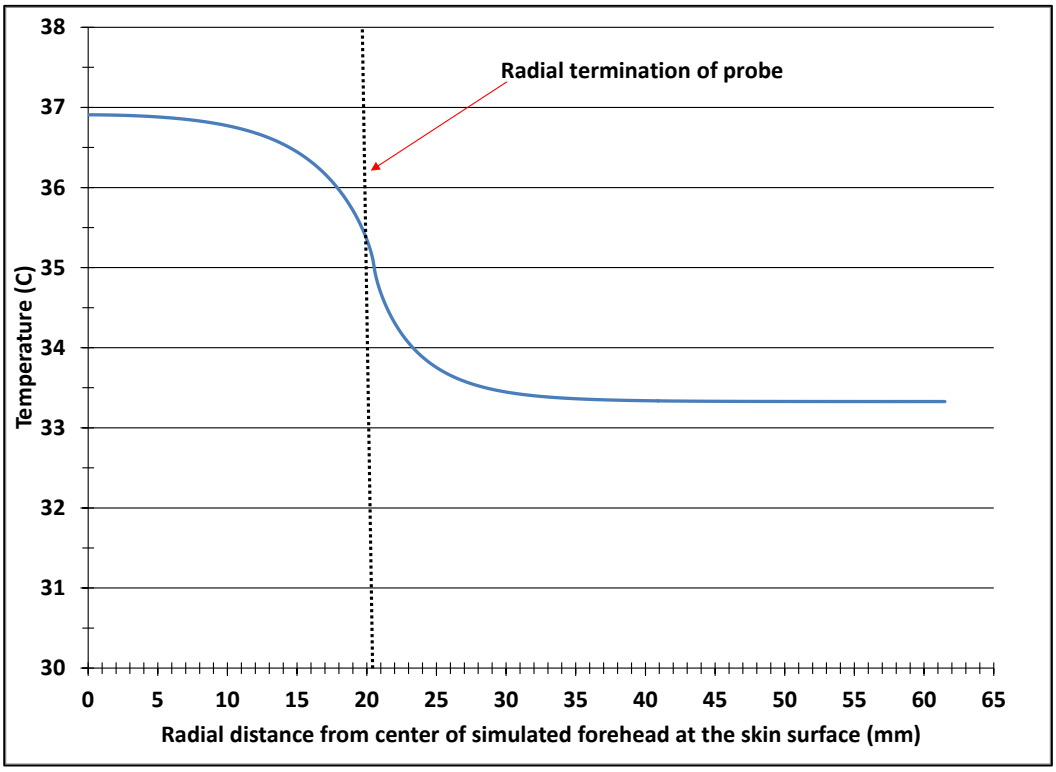

Figure 2-26. Skin surface temperature as a function of radial distance.

The heat transfer taking place within the probe-tissue system is best viewed by means of vector diagrams. The first of these diagrams, Figure 2-27, displays vectors whose lengths are proportional to the rate of heat flow. The shortest of the heat flow vectors are situated in the upper portion of the probe. This outcome is clear testimony to the effectiveness of the disk-heater system in suppressing heat transfer. That suppression is also evidenced by the directions of heat flow revealed by the vectors. It can be seen that the heat is diverted radially outward in order to avoid the blockage imposed by the disk-heater system. At radial distances that extend beyond the probe by about 15 mm, the radial component of the heat flow disappears, and a one-dimensional upward pattern takes over.

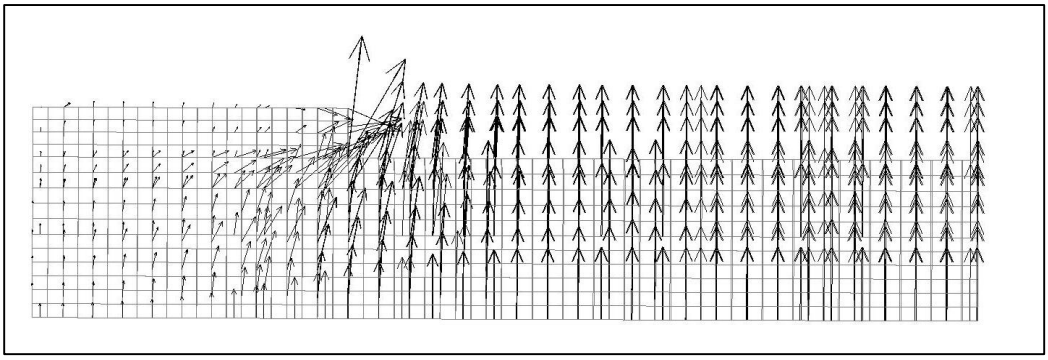

Figure 2-27. Heat flow vectors whose lengths are proportional to the magnitudes of the heat transfer rates.

The issue of heat flow direction is optimally viewed when the lenghts of the heat flow vectors are uniform rather than being proportional to the magnitude of the flow. Figure 2-28 has been prepared in this regard. The figure shows that there is, in fact, a slight imperfection in the disk-heater system inasmuch as heat does escape from the upper surface of the probe into the ambient.

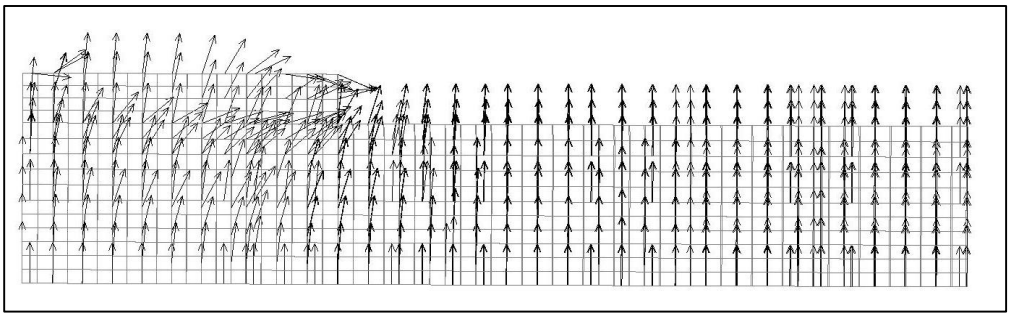

Figure 2-28. Heat flow vectors of uniform length.

2.12.3 Sensitivity study of natural convection heat transfer coefficients

To quantitatively evaluate the sensitivity of the skin temperature results to the input values of the natural convection heat transfer coefficients, supplementary numerical solutions have been performed making use of coefficient values that differ by either 10% greater than the originally selected values or 10% less than the originals. The results

corresponding to these situations are conveyed Figure 2-29.

The figure conveys the variation of the skin temperature as a function of the inputted heat flux, respectively for the three natural convection conditions investigated. In this regard, it is noted that separate heat transfer coefficients were employed for each of the exposed surfaces of the probe and forehead. Each of these individual coefficients were scaled by the same percentages as designated in the foregoing. For the results presented in the figure, the radiation heat transfer coefficients were held constant.

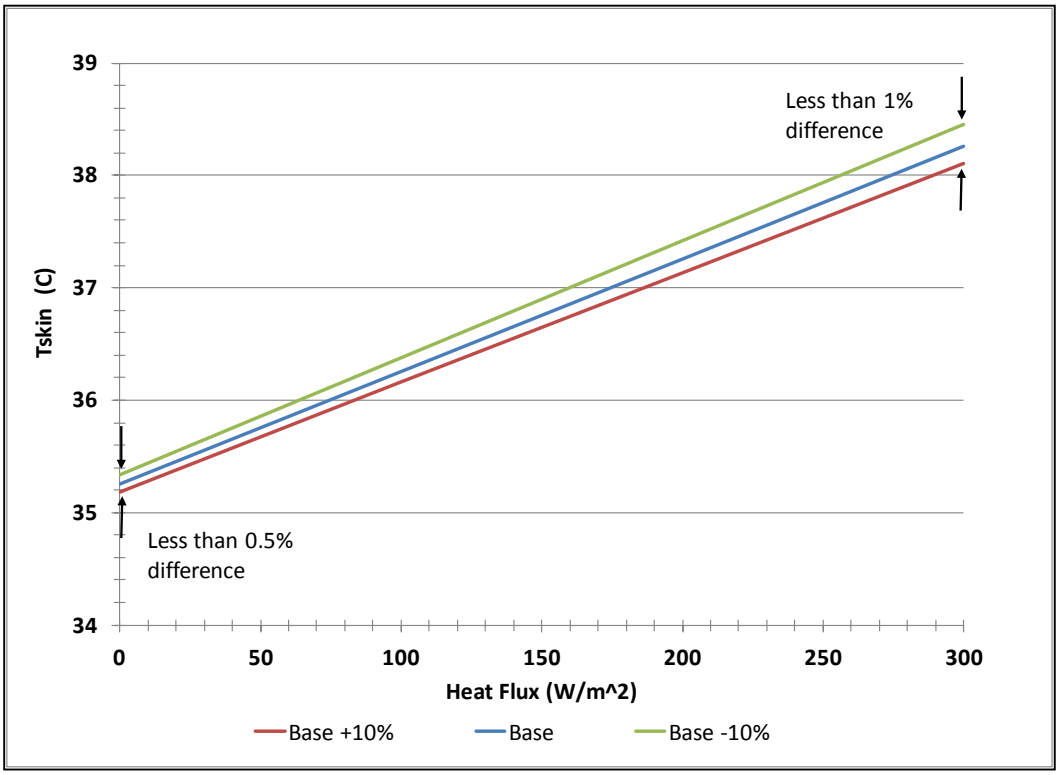

Figure 2-29. Predicted skin temperatures corresponding to natural convection heat transfer coefficients that are 1.1 and 0.9 times the base value, and compared with results obtained for the base value.

The main message expressed by Figure 2-29 is that the variations in the predicted skin-surface temperatures are well within 0.5ºC tolerance. At the lowest heat flux, the

difference in the skin-surface temperature corresponding to a 20% variation in the heat transfer coefficient was approximately 0.2°C. On the other hand, at the highest investigated heat flux, the corresponding variation was 0.35°C.

2.13 Results and discussion for a two-heater system

An alternative design of the temperature probe included a two-heater system. The motivation for considering that enhancement was to diminish the radial variations of the skin surface temperature underneath the temperature probe. The innermost heater consisted of a circular annulus, while the outer heater was another annulus. With regard to dimensions, the diameter of the inner heater was 14.5 mm, and the overall diameter of the two-heater system was identical to that of the one-heater setup.

Numerical simulations were performed for the two-heater system under the condition that the inner heater had a fixed heat flux while the outer-heater heat flux was varied parametrically. The resulting radial temperature variations at the skin surface are displayed in Figure 2-30. It can be seen from the figure that the radial dropoff of the skin temperature beneath the probe is delayed when two heaters are used. The degree of delay increases as the heat flux applied by the outer heater is increased. It is also seen that the outer heater, when operated at the higher heat fluxes, causes a slight increase of the skin temperature at the point of measurement. This increase is on the order of 0.1°C.

Although the use of a two-heater system does delay the temperature dropoff compared to that for a one-heater arrangement, the delay appears to have no practical effect.

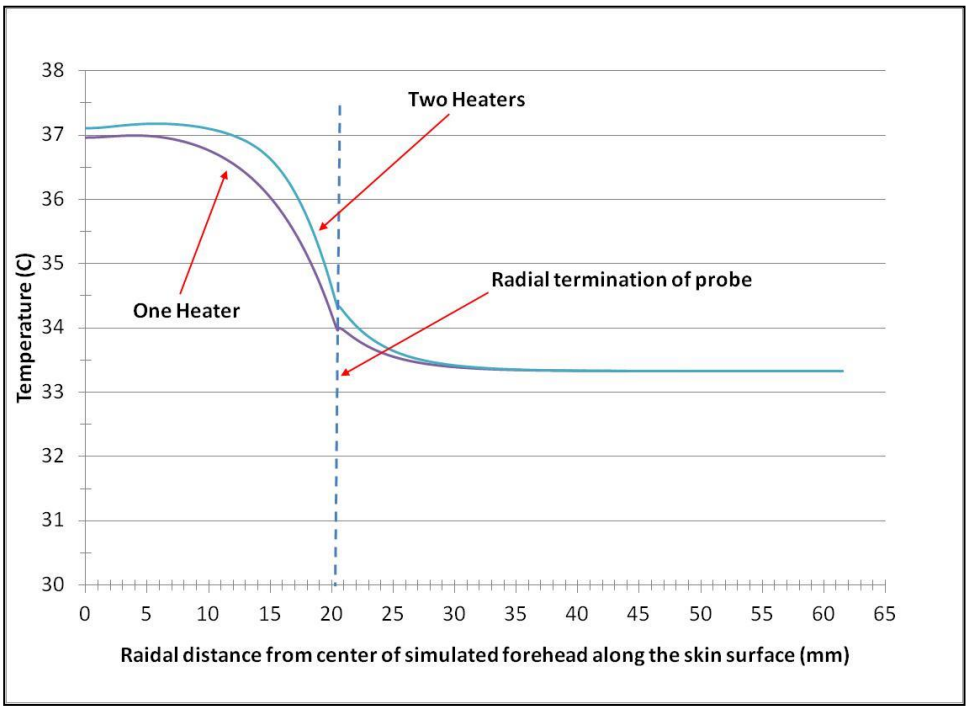

Figure 2-30. Radial temperature distribution for one and two-heater systems.

2.14 Outcomes of Chapter 2

The focus of this chapter was to model and implement the numerical simulation of the operating characteristics of a temperature probe whose underlying principle is the attainment of an adiabatic boundary condition at the exposed surface of the probe. The modeling effort included a variety of probe configuration and operating conditions as follows: two distinct transient applications of the probe and two heater designs. Each of the transient scenarios represented a limiting case. With regard to heater design, both a single heater spanning the diameter of the probe and a two-heater arrangement spanning that same distance were evaluated.

Both transient scenarios achieved steady state results that were in mutual agreement. The time to achieve steady state ranged from 8 to 12 minutes, for the respective transients.

Attention was also focused on the radial variation of the temperature along the skin surface as well as the axial temperature variation between the core value and that of the

skin surface. For both of the aforementioned heater arrangements, the radial temperature variation at the skin surface beneath the probe displayed a dropoff with increasing distance from the probe axis. However, the dropoff did not cause any ambiguity in the skin temperature measured at the axis. The difference between the assigned core temperature of 37^{o}C and the measured skin surface temperature was 0.2^{o}C. That temperature difference is well within the targeted accuracy of 0.5^{o}C.

The numerical simulations took account of heat transfer between the surrounding ambient and the exposed surfaces of the probe and the skin. Both natural convection and thermal radiation were taken into account. With regard to natural convection, an uncertainty analysis based on a 20% variation of the heat transfer coefficient was performed. The outcome of that study indicated an insensitivity of the skin surface temperature prediction, with the response to the imposed variation of 0.1^{o}C.

The clear message of the results of this chapter is that the probe which was analyzed performed well within the design targets.

CHAPTER 3

Experimental Evaluation of Temperature Probe

3.1 Introduction

To confirm the design based on the numerical simulations, an ex-vivo experimental apparatus was fabricated and operated. The apparatus made use of surrogate media to represent the tissue bed and the body core temperature. The measured surrogate skin temperature was compared with the simulated body core temperature, and this comparison is the metric used to characterize the accuracy of the design.

Another evaluation of the accuracy of the design was afforded by clinical data [49]. The subject pool consisted of 111 persons encompassing newborns to adults of age over 21. The subjects included both genders and broad ranges of weight and height. The totality of data will be assessed both globally and from the standpoint of age, gender, height, and weight. The forehead temperatures determined by the probe were compared with either that of rectal or oral measurements.

3.2 Experiment setup

The apparatus that was fabricated for the experimentation is pictured in Figure 3-1. The key components of the apparatus are: (a) the temperature probe whose performance is to be evaluated, (b) a slab of HDPE (high density polyethylene) which serves as a surrogate for the several layers of tissue that occur in the natural measurement environment, (c) an aluminum plate which includes a serpentine flow passage through which temperature-controlled water is circulated, (d) a thermostatically-controlled water bath which is part

of a closed recirculation loop that provides a constant flow of water to the aluminum plate, (e) closed-cell polystyrene insulation, cut and pieced to surround the entire apparatus, and (f) data acquisition system. The aluminum plate in conjunction with the temperature-controlled circulating water served to impose the equivalent of the body core temperature at the lower face of the HDPE block. To ensure good thermal contact between the aluminum plate and the HDPE block, thermal grease was employed.

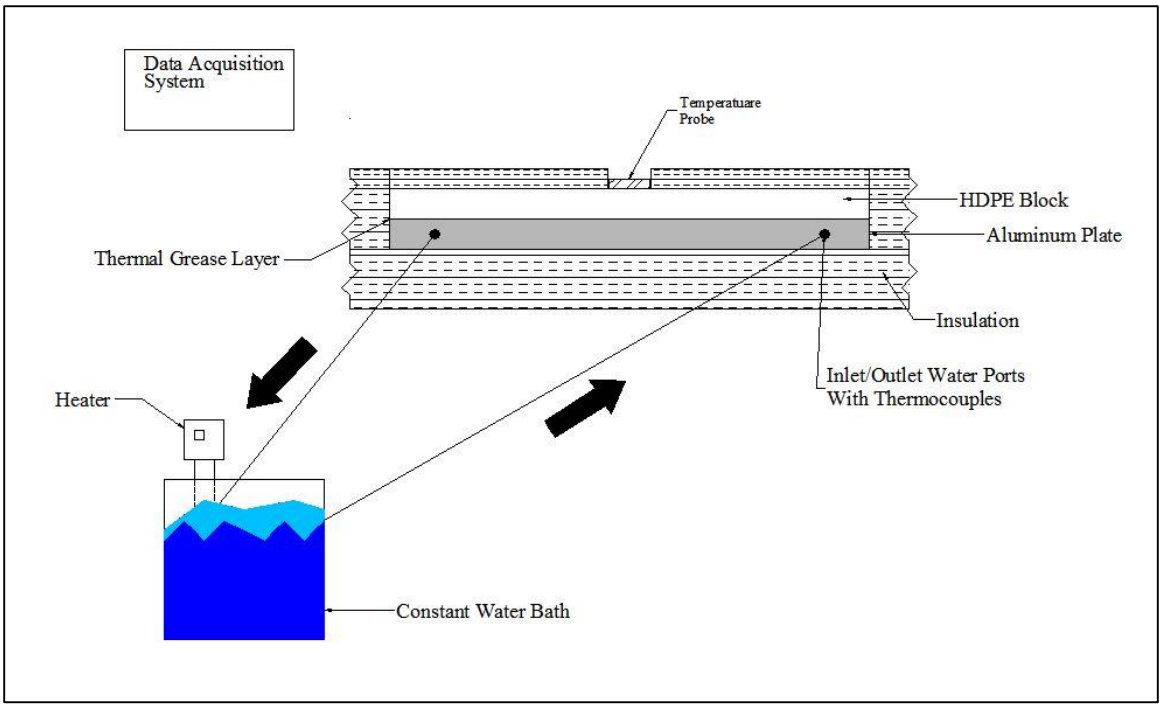

Figure 3-1. Experiment setup for modeling the performance of the temperature probe.

To provide perspective for the choice of HDPE as a surrogate, its thermophysical properties are displayed in Table 3-1. The table also includes the tissue layers and their properties that are being replaced by the surrogate medium. The averages of the respective properties are listed and compared with those of HDPE. From the comparisons, it is seen that the average values of the tissue properties are not precisely coincident with those of HDPE. However, it was judged that the deviations would not affect the validation of the probe performance. As an alternative surrogate medium, consideration was given to low-density polyethylene (LDPE). The thermophysical

properties of LDPE are also listed in Table 3-1. Inspection of the table shows that the properties of HDPE are closer to those of the tissue bed than are the properties of LDPE.

Table 3-2. Thermophysical properties of HDPE compared to skin [50].

	k (W/m K)	c (J/kg K)	ρ (kg/m^3)	t (mm)
Bone	1.0	1700	1500	5.4
Fat	0.2	2390	1050	3.0
Inner skin	0.38	3570	1130	1.0
Outer skin	0.38	3570	1130	1.0
Average (k, c, and ρ)	0.49	2808	1203	10.4
HDPE	0.46	2300	950	12.7
LDPE	0.33	2100	910	

The thickness of the HDPE block is 0.5 inches (12.7 mm) with planform dimensions of 12 inches by 12 inches. These planform dimensions are larger than those of the forehead, but this dimensional difference is irrelevant because the extended surface is adiabatic. The aluminum plate has the same footprint as the HDPE block. Due to the continuous flow of temperature-controlled water through the plate and its high conductivity, the interface between the aluminum plate and the surrogate HDPE can be regarded as having a precisely known and uniform temperature.

A photograph of the experimental setup viewed from a near-plan-view orientation is displayed in Figure 3-2. The circular feature centered in the photograph is the temperature probe to be evaluated. Under normal operating conditions, the probe would be intimately surrounded by insulation. However, for the purpose of the photograph, the insulation had been withdrawn. Three temperature sensors are identified in the figure. Thermocouple 1 (TC 1) is adhered to the exposed surface of the surrogate skin. The temperatures of the two thermistors situated inside the probe were controlled to be equal so that the "skin" surface would be adiabatic. The first thermistor is positioned adjacent to the heater. The second one, the "skin" thermistor, is in direct contact with upper surface HDPE which serves to represent the outer skin surface.

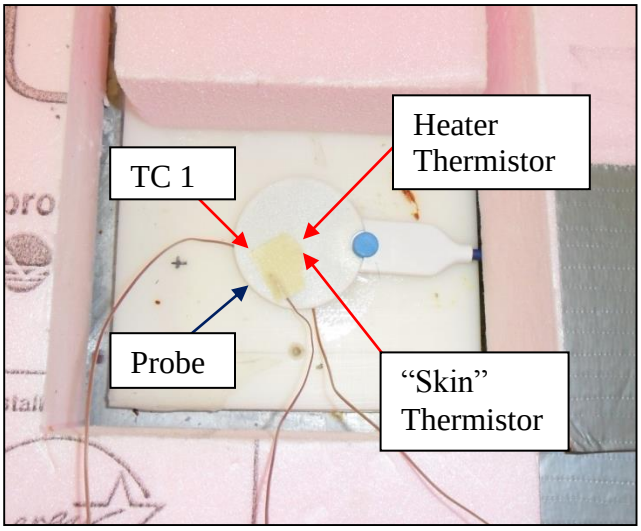

Figure 3-2. Near plan view of the test setup.

3.2.1 Calibration method for thermistors

The quality of the experiments is highly contingent on the accuracy of the instrumentation. In this regard, calibration of the thermistors is an essential task to be performed prior to the initiation of the experimentation.

A thermistor is a temperature-sensitive resistor whose resistance significantly varies as its temperature changes. It is a semiconductor made from metallic oxide powders, molded into a small bead, disk, wafer, or other shape, sintered at high temperatures, and then coated with epoxy or glass. The resulting device exhibits an electrical resistance that is very sensitive to temperature change. Furthermore, in contrast to the behavior of a reference resistance thermometer, the electrical resistance of a thermistor decreases with temperature increases [51].

The Steinhart-Hart equation is used to describe the resistance of a thermistor as a function of temperature [52]. The equation, given a resistance, calculates the temperature of a thermistor at that given resistance as shown in Equation 3-1.

$$\frac{1}{T} = A + Bln\left(R\right) + C\left(ln\left(R\right)\right)^3 \quad (3\text{-}1)$$

where *T* is the temperature (in Kelvin), *R* is the resistance at *T* (in ohms). *A, B, C* are the Steinhart-Hart coefficients. When the coefficients for the equations are not given, they must be determined by experiments. This determination is performed here by taking three accurate measurements of resistance at selected temperatures and then solving a system of three simultaneous, non-linear algebraic equations. This process yields values of the coefficients *A, B,* and *C* that are introduced into the Steinhart-Hart equation.

For the present investigation, the evaluation of the coefficients was performed at temperatures of 29, 37, and 42ºC. These temperatures span the relevant range of the probe. The probe was placed into a subsequently sealed polyethylene bag and immersed into a temperature-controlled water bath. Once the waterbath reached the set temperature, the resistance of the probe was read by a LabVIEW data acquisition system. The waterbath temperatures were measured by a NIST-traceable thermometer whose smallest scale division was 0.05ºC. Table 3-2 lists the raw data from the calibration.

Table 3-3. Resistance measurements of thermistor at various waterbath temperatures.

Waterbath Temperature (^{o}C)	Measured Resistance (Ω)
29.3	8504
37.3	6373
42.3	5353

The calculated Steinhart-Hart *A, B,* and *C* coefficients based on the data of Table 3 are *A* = $8.50*10^{-4}$, *B* = $2.59*10^{-4}$, and *C* = $1.53*10^{-7}$ respectively. A check of the coefficients showed that an input resistance of 6373Ω into Equation (3-1) yields a temperature of 310.4 K (37.3ºC).

3.2.2 Experimental data

Traces of the skin temperature variations experienced by the skin thermistor are displayed in Figure 3-3(a) as a function of time for operating Scenario 1 (see Section 2.12.1). As is mandatory for any well-executed experiment, replicate data runs were carried out. In the present instance, three independent data runs were performed, each utilizing a different probe. In addition to the experimental data displayed in the figure, the results of the numerical prediction are also presented. It can be seen from the figure that the replicate data are not precisely congruent, especially at early times. As the data approach steady state, the replicate results are virtually identical. Of particular interest is the time required to achieve steady state. That time is somewhat dependent on the tolerance allowed in the steady-state definition. If the accepted accuracy criterion of 0.5^{o}C [16] is invoked, then the steady-state time for the three data sets is 3.5 minutes.

The numerical predictions depart moderately from the experimental results. If the 0.5^{o}C tolerance is allowed for the determination of the steady-state time, it is found that steady state is achieved at 5.5 minutes. Therefore, the numerically determine steady-state time is conservative.

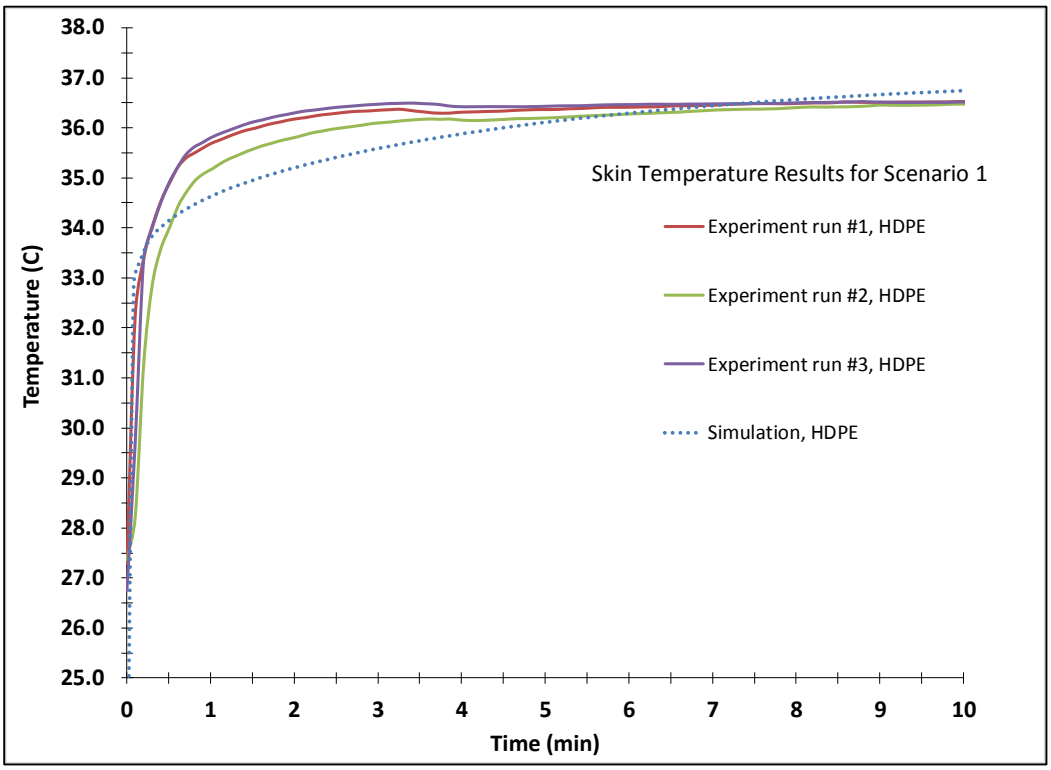

Figure 3-3(a). Comparison of simulation and experimental skin surface temperature results for operating Scenario 1. The experimental data were obtained by use three separate probes.

A presentation, similar to that of Figure 3-3(a), is made for the results of Scenario 2 and presented in Figure 3-3(b). As can be seen from the figure, the three replicate data runs are in excellent agreement, in contrast to the experimental behavior presented Figure 3-3(a). These different behaviors can be attributed to the relative ease of setting up the initial conditions for the experiments of Scenario 2 compared with the complex initial setup of Scenario 1. From the standpoint of steady-state times, the simulation-based results and that of the experimentation are approximately equal to one minute, if the 0.5^{o}C tolerance is allowed.

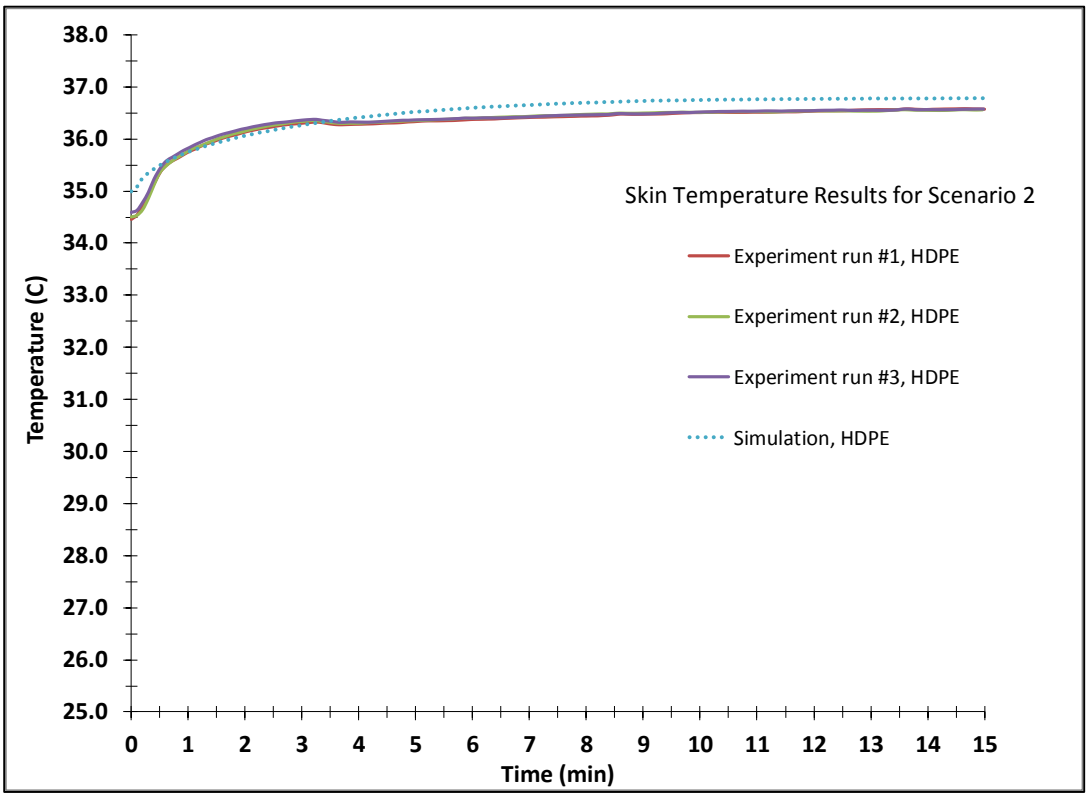

Figure 3-4(b). Comparison of simulation and experimental skin surface temperature results for operating Scenario 2. The experimental data were obtained by use three separate probes.

The steady-state temperatures extracted from data runs additional to those of Figure 3-3 are presented in Figure 3-4. The probes used for the results of the latter figure were different from those used for the former. Figure 3-4 is subdivided into three parts (a-c), with each part dedicated to presenting data each of three different measurement sites: (a) skin, (b) atop the HDPE slab, and (c) heater. For each of parts (a), (b), and (c), three replicate data runs were performed. All of the data fell in the range between 37 and 38^{o}C because the temperature of the circulating water exceeded 37^{o}C in every one of the data runs. Consequently, the ordinate range for each of the three parts of the figure corresponds to those temperatures.

In general, for each measurement site, the data for the three replicate experiments are in generally good agreement. The spread among the data at each site is in the range of 0.2 – 0.4ºC. Since the accepted standard for the measurement of the temperature is an accuracy of 0.5ºC [16], the replicate runs can be accepted as demonstrating and acceptable level of performance.

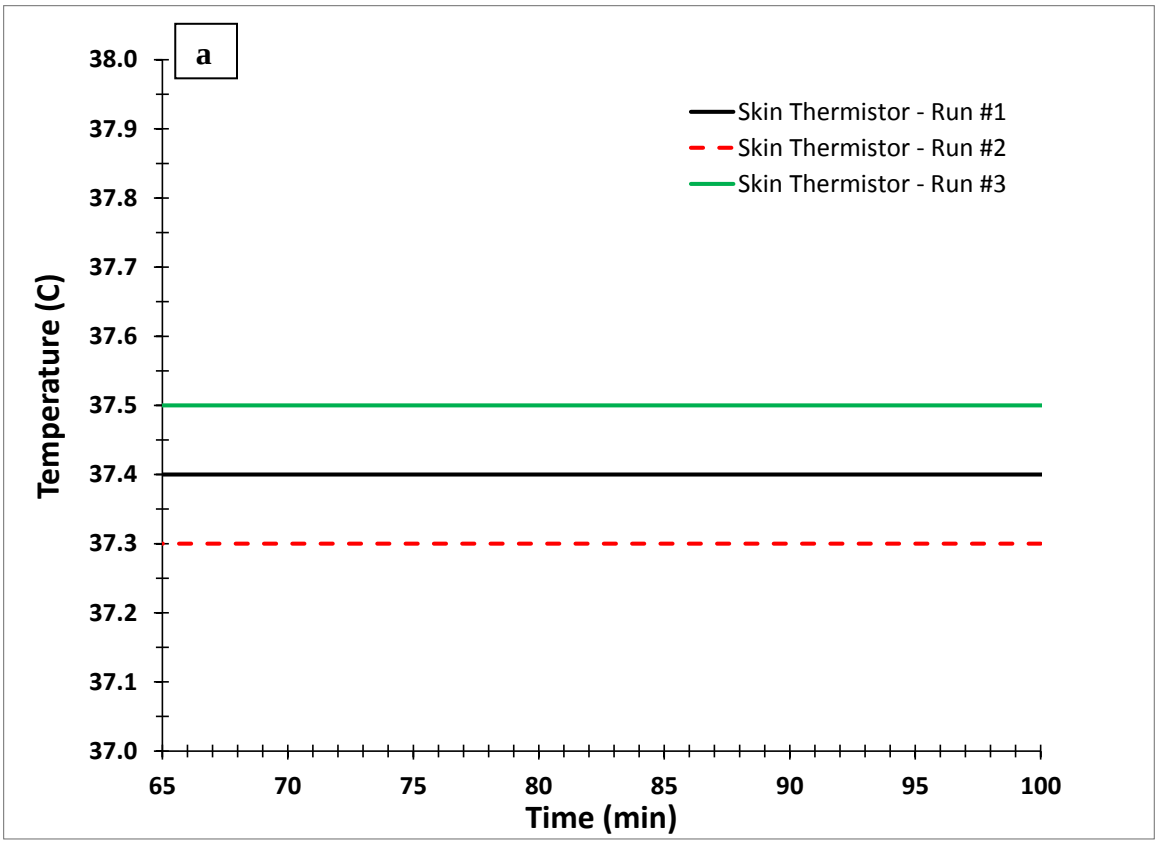

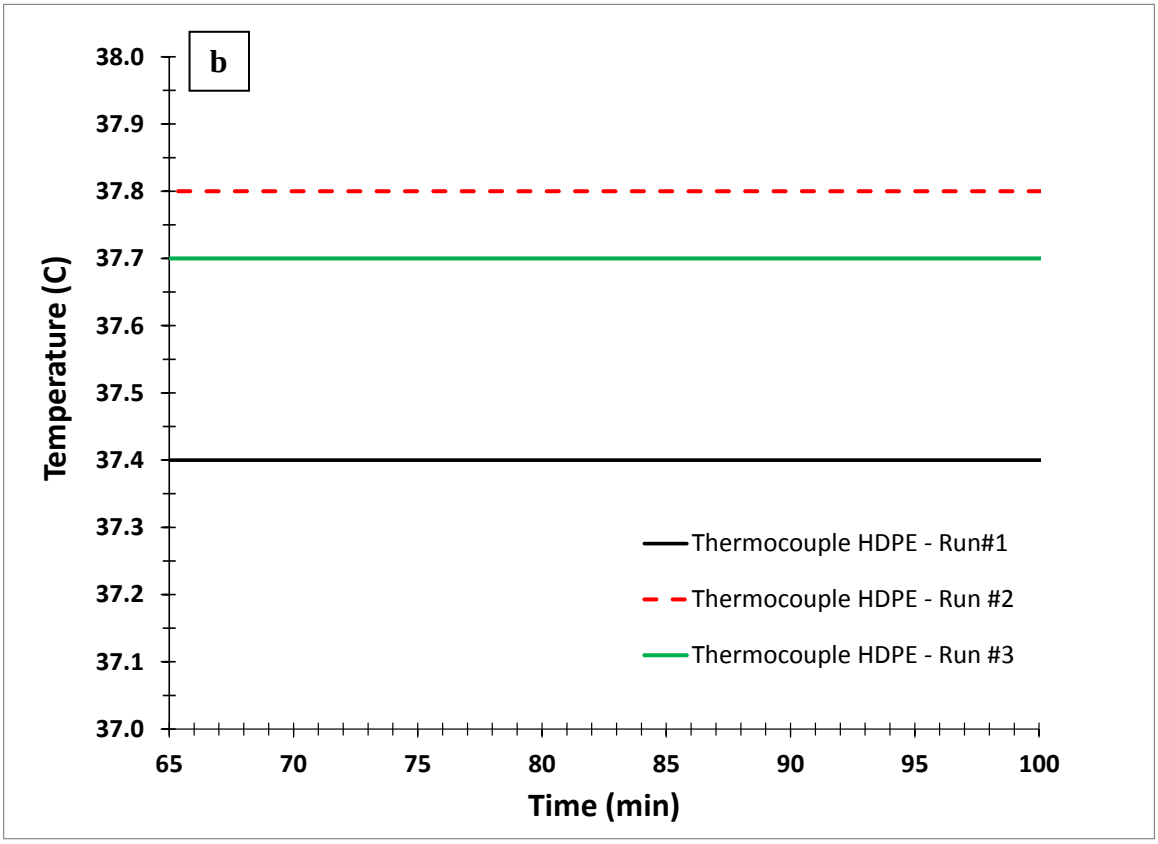
b
38.0
37.9
37.8
37.7
37.6
37.5
37.4
37.3
37.2
37.1
37.0
Temperature (C)
65
70
75
80
85
90
95
100
Time (min)
Thermocouple HDPE - Run#1
Thermocouple HDPE - Run #2
Thermocouple HDPE - Run #3

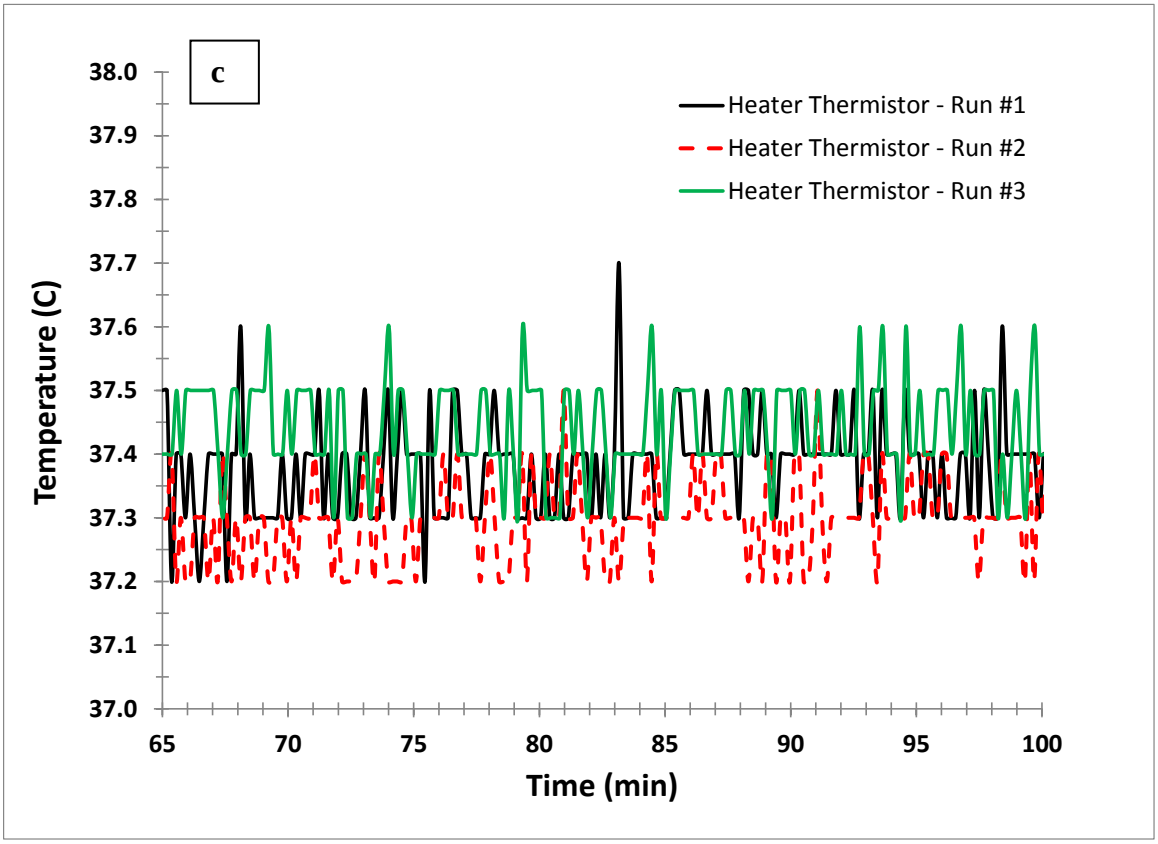

Figure 3-5. Temperature measurements for three different probe runs with (a) skin thermistor results, (b) HDPE thermocouple results, and (c) heater thermistor results.

The nature of the temporal variations displayed in the respective (a), (b), and (c) parts of Figure 3-4 differ. The first of the figures, (a), shows the thermistor temperature values with a difference among the three replicate runs to be 0.2^{o}C. Furthermore, in (b), the temperature values of the HDPE using thermocouples have a temperature difference of 0.4^{o}C. In contrast, the oscillatory heater-adjacent thermistor values in (c) are due to the On/Off nature of the heater control.

3.3 Processing of clinical data

Clinical data relating to the performance of the probe were collected, providing considerable information with regard to the accuracy of the probe [49]. All told, 90 patients were involved in the clinical tests. For each patient, the steady-state temperature

reported by the probe was compared with a temperature measured at a would-be trusted measurement site. The trusted site was under the tongue (oral). However, the oral site is by no means the site of choice among medical practitioners. Rather, the preferred site is the esophagus [16, 62]. To obtain the esophageal temperature, it is necessary that the subject swallow the temperature sensor. Since the clinical studies were performed at several locations in a short period of time, it was found impractical to make use of the esophagus temperature measurement, and the oral measurement was used as a default. The use of the oral measurement is sub-optimal and, in all likelihood, contributed to creating unrealistic deviations of the temperatures measured by the probe and by the oral method [53, 61]. Table 3-4 lists both the age range and gender of the participants.

Table 3-4. Breakdown of the number of patients enrolled in the study by age and gender.

	Subjects	Male	Female
1 year < Age < 5 years	30	19	11
5 years < Age < 12 years	20	6	14
12 years < Age < 21 years	20	11	9
Age > 21 years	20	8	12
Total	90	44	46

The first analysis used to extract conclusions from the collected data involved determining, for each participant, the difference between the temperature measured by the probe and that determined orally. These differences were plotted for each participant as a function of number between 1 and 90. The outcome of this processing activity is displayed in Figure 3-5. Inspection of the figure shows that the great majority of participants provided probe temperatures that exceeded the oral value. All of the positive values of the temperature difference were averaged, yielding the result 0.504^{o}C with a standard deviation of 0.267. This outcome is very slightly in excess of the acceptable accuracy standard of 0.5^{o}C [16]. However, since the reference temperature used to form the difference is the less-than-precise oral value, the grounds for faulting the probe are very fragile. It appears that there is a consensus that orally measured temperatures are lower than actual body core temperatures [53]. If this is true, then the positive

temperature differences exhibited in Figure 3-5 should diminish, and the positive differences would average to a value below 0.5ºC. If the negative difference values are averaged, the result is 0.376ºC with a standard deviation of 0.293. This is an acceptable outcome.

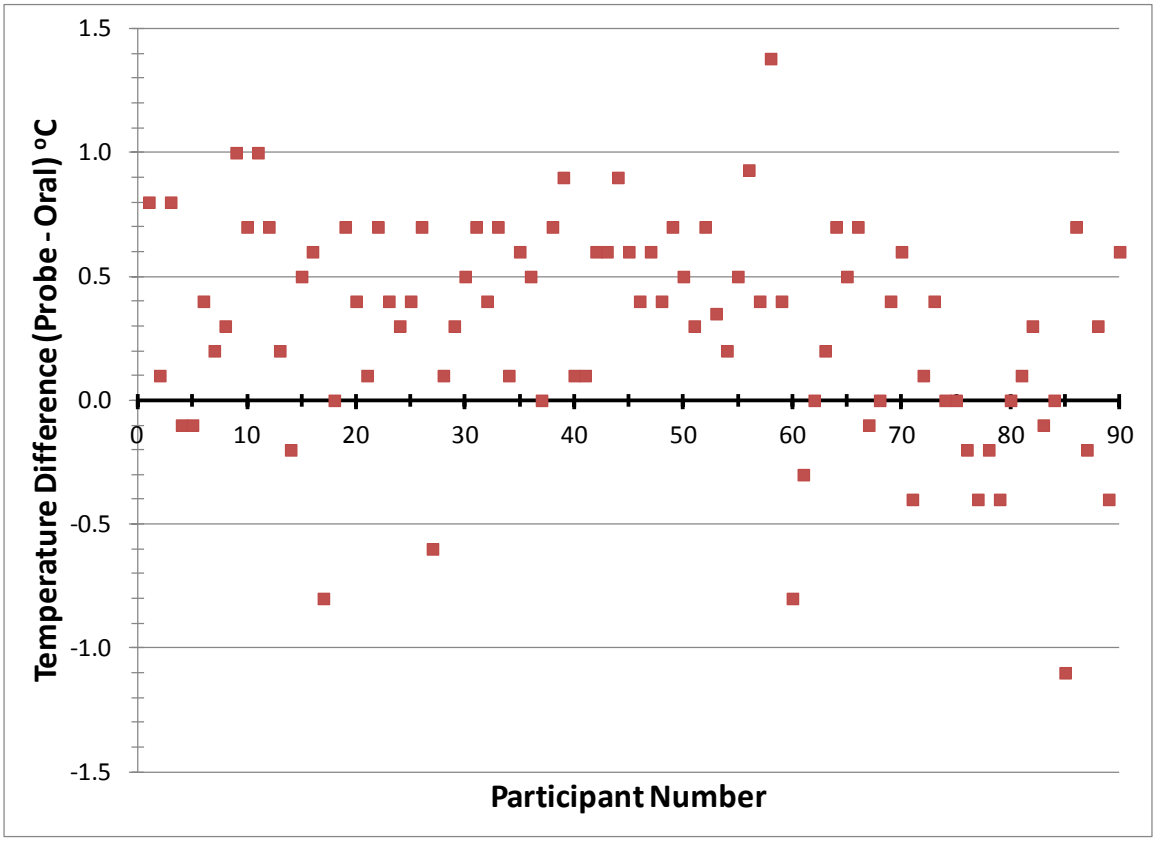

Figure 3-6. Temperature difference (probe – oral) distribution as a function of participant number.

An alternative analysis of the basic clinical data can be made by grouping the results according to gender. The outcome of such a grouping is presented in Figure 3-6. Inspection of the figure reveals that, once again, positive temperature differences are more frequently encountered than are negative differences. For the positive difference situation, the mean difference among females was found to be 0.540ºC, while the corresponding difference for males was 0.473ºC. If standard deviations are used to quantify the temperature differences, the female/male values would be 0.259/0.273. For

the negative differences, the female and male averages were 0.409ºC and 0.317ºC respectively. The corresponding standard deviations for the negative differences are 0.339/0.194. It is difficult to draw definitive conclusions about female and male behaviors from the stated averaged differences and standard deviations. For positive averaged differences, the values for the different genders are more or less the same, while for the negative differences, the respective gender values differ significantly. This outcome may be attributed to small number of available negative-difference values.

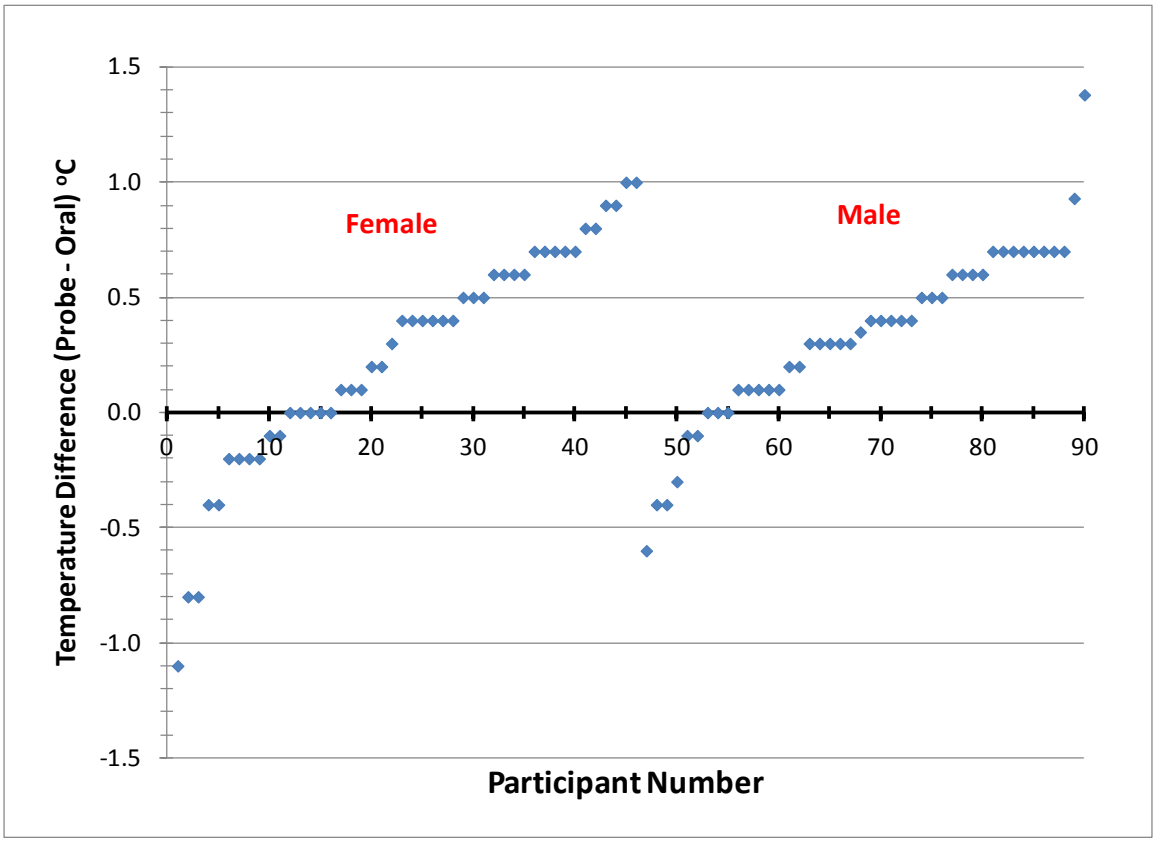

Figure 3-7. Temperature difference (probe – oral) distribution as a function of gender.

Analysis of the clinical data was also performed on the basis of age. In the age group between 5 and 12 years, all of the temperature deviations were positive. In the next group, ages 12 to 21, the positive deviations outnumbered the negative deviations. For the adults, 21 years of age and greater, there was a balance of the number of positive and

negative temperature differences. These outcomes can be attributed to the patience of the participants of different ages.

3.4 Outcomes of Chapter 3

Experiments were performed to validate the temperature probe design that had been created on the basis of numerical simulations. A validation of the predicted results is regarded as being mandatory.

The experimental work reported in this chapter consisted of two independent activities. In the first, a surrogate setup was designed and fabricated to facilitate the collection of highly accurate temperature data at a simulated skin surface and at a simulated body core. The experimental setup enabled precise control of the operating conditions and, thereby, provided a valid test of the simulation-based design. Three independent replicate data runs were performed. The differences between the measured skin temperature and that of the simulated core for the respective data runs were 0.1^{o}C. Since the accepted standard of temperature measurement accuracy is 0.5^{o}C [16], the satisfactory performance of the probe is thereby established.

The second evaluation of the probe design was based on clinical data [49]. A total of 90 subjects, spanning the ages of one to > 21, participated in the clinical experiments. The clinical sample included both males and females. Temperature measurements by the probe were compared with those measured orally. Oral temperatures do not represent the measurement of choice among medical practitioners, but they were the most convenient temperature standard for the clinical evaluations. There is substantial evidence [53] that oral temperature measurements are generally low compared with the body core temperature.

The majority of temperature differences (probe – oral) were found to be positive. For the entire 90-person sample, the average value of the positive temperature differences was found to be 0.504^{o}C, while the average of the negative temperature differences was

0.376ºC. On the other hand, the standard deviations for the two categories were 0.267 and 0.293ºC. The recognition that orally measured temperatures tend to be low suggests that the aforementioned temperature differences should be modified, to an uncertain extent. Consideration of the factual outcomes conveyed in the preceding paragraphs leads to the conclusion that the accuracy of the probe is within the accepted standard of 0.5ºC.

CHAPTER 4

Attainment of Faster Temperature Response and More Compact Geometry

4.1 Introduction

The current probe has a foam disk placed between the axial locations of two thermistors to create a zero heat flux probe. Simulation results conveyed in Figure 2-21 have shown that it could take up to 12 minutes to reach an equilibrium temperature in a scenario in which the probe is at an initial temperature of 20^{o}C. This chapter will look into ways to improve on the response time, both for Scenarios 1 and 2 that are defined in Section 2.12.1.

4.2 Thermal response corresponding to replacement of foam by aluminum

The first step in evolving a redesign that enables a much faster response of the probe is to replace the foam disk with an aluminum one while keeping all the dimensions the same. The rationale for choosing aluminum is that its thermal conductivity value is approximately 3000 times that of foam. From Chapter 2, the two scenarios for which the revised probe needs to be investigated are 1) the probe is initially at 20^{o}C while the tissue layer is initially in equilibrium with the surroundings and 2) the probe and skin are initially both at steady state with the surroundings. For this investigation, the heater is assumed to consist of a single circular element.

Figure 4-1 shows the results of the predicted skin temperature response obtained due to the replacement by aluminum for both scenarios. The figure contains four curves, two of which may be regarded as baselines because they correspond to the case in which the foam is in place. The other two curves are for aluminum which has replaced the foam.

From the inspection of the figure, it is seen that the replacement of the foam disk by an aluminum one gives rise to major changes in the temperature versus time trace. In particular, in the case of Scenario 1, the use of aluminum instead of foam gives rise to a detrimental response. The relatively low initial temperature of the probe is captured by the aluminum which reduces the measured skin surface temperature to an unacceptably low value. Furthermore, the rate of recovery of the skin surface temperature is also slowed by the significant heat capacity possessed by the aluminum.

If attention is refocused on Scenario 2, it is seen that the replacement of foam by aluminum has a positive effect. Instead of the seven minutes duration needed to achieve steady state with the foam in place, the aluminum enables steady state to be attained within a half minute. This outcome encourages further study with regard to varying the dimensions of the aluminum disk. The motivation for further study is twofold: (a) to further reduce the response time and (b) to diminish the material cost of the aluminum. In view of the importance of cost issues, the direction of further study is to diminish the thickness of the aluminum.

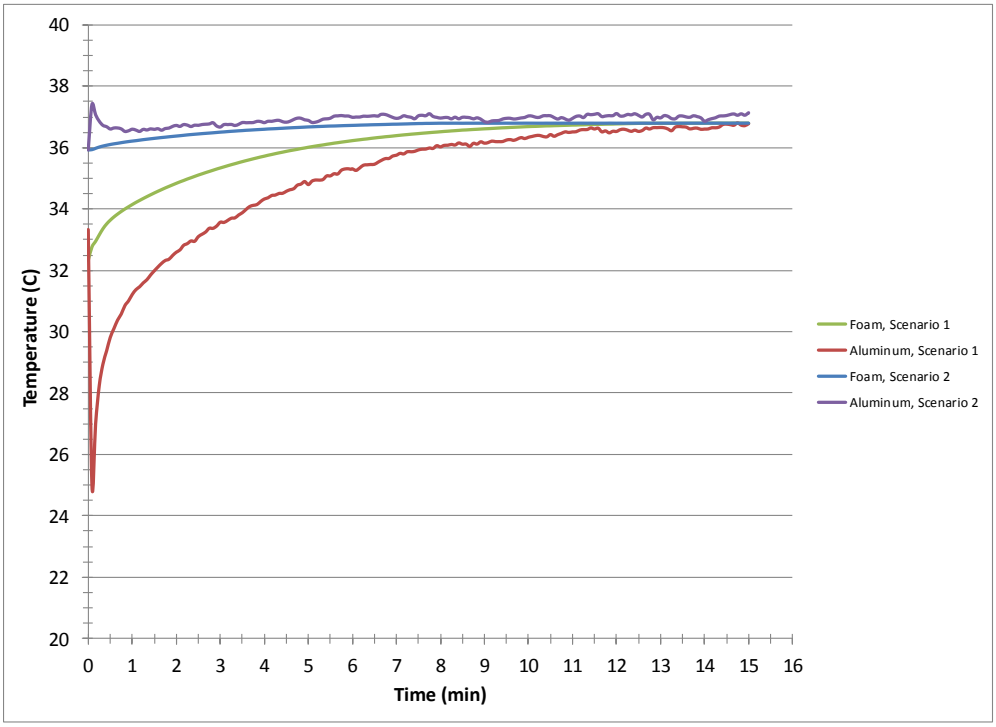

Figure 4-1. Response of the predicted skin surface temperature to foam and aluminum disk materials.

4.2.1 Tailoring the thickness of the aluminum disk

A restriction to the degree of thickness reduction of the aluminum disk is that its thermal resistance might become too small to enable the temperature difference across it to serve as an indicator of the rate of heat transfer passing through it. In addition, a too-thin aluminum disk would not successfully support the heater. With these cautions in mind, the reduction in the aluminum-disk thickness was limited to 1.8 mm, leading to a disk thickness of 1.5 mm.

Plotted in Figure 4-2 are the predicted skin surface temperature results corresponding to parametric values of aluminum disk thickness from 3.3 to 1.5 mm, the former being the original thickness. The figure conveys information for eight cases. The first two in the order listed in the figure correspond to the original baseline case where foam served. The next two in the listed order may be regarded as secondary baseline in which aluminum

has replaced foam while maintaining the original thickness. The other results corresponding to various reduced thicknesses.

To provide perspective for the results, it may be noted that for aluminum to be used instead of foam, it is necessary that its equilibrium temperature is very near that of the skin surface. This requirement cannot be fulfilled for Scenario 1 where the probe is at an initial temperature of 20^{o}C. It is clear that the use of an aluminum disk does not diminish the time to achieve steady state for Scenario 1.

For Scenario 2, it can be seen by the figure that rapid attainment of steady state is achieved for all of the investigated disk thicknesses. For all thicknesses, steady state sets in well before a half minute. The steady-state value correspond to use of aluminum differs by 0.1^{o}C compared with that of foam.

This outcome is strong suggestion that the replacement of the foam by aluminum is worth pursuing.

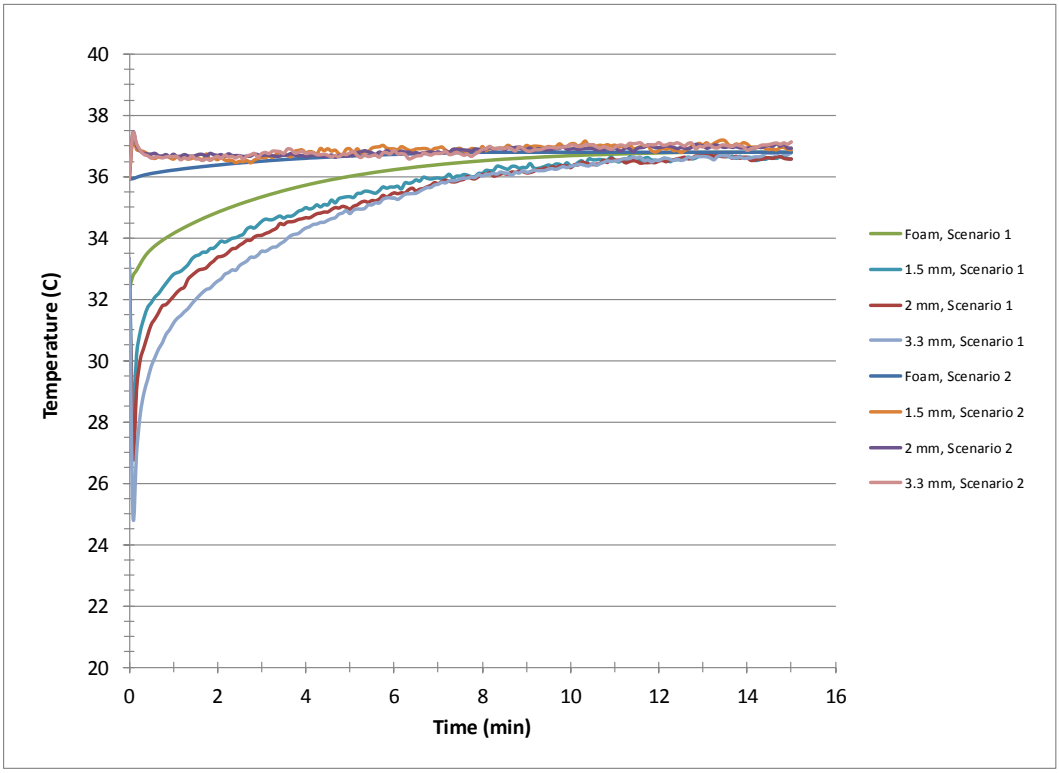

Figure 4-2. Response of skin temperature for different aluminum thicknesses.

4.3 Probe compactness

There are at least two significant motivations for investigating the characteristics of a probe having a smaller radius than the original radius of 20.5 mm. One of these is that a smaller diameter probe could be accommodated on foreheads having smaller overall dimensions. The other motivation is that the material cost of the probe could be diminished.

The first step is to create a baseline situation against which to compare any changes in radius. To this end, Figure 4.3 has been prepared. The figure shows baseline information in the form of radial temperature variations along the skin surface for the original probe radius probe of 20.5 mm for both foam and aluminum disks. Also displayed in the figure are radial temperature distributions for aluminum probes of having thicknesses of 1.5 and 2 mm.

Inspection of the figure shows that from the standpoint of providing an accurate temperature result at the point of measurement, disks of foam and of aluminum both perform satisfactorily. There is, however, an important difference in the detail. Whereas, the temperature drops off across the radial extent of the probe when the foam is in place, no such dropoff occurs when aluminum is used as the disk material. In fact, the uniformity of the temperature is independent of the disk thickness.

With aluminum, the radial temperature is constant compared to foam due to having a higher thermal conductivity value. Taking advantage of this, the probe can be halved in its diameter and still prove to be effective as seen in Figure 4.4. This outcome encourages examination of the use of aluminum disks of different radii.

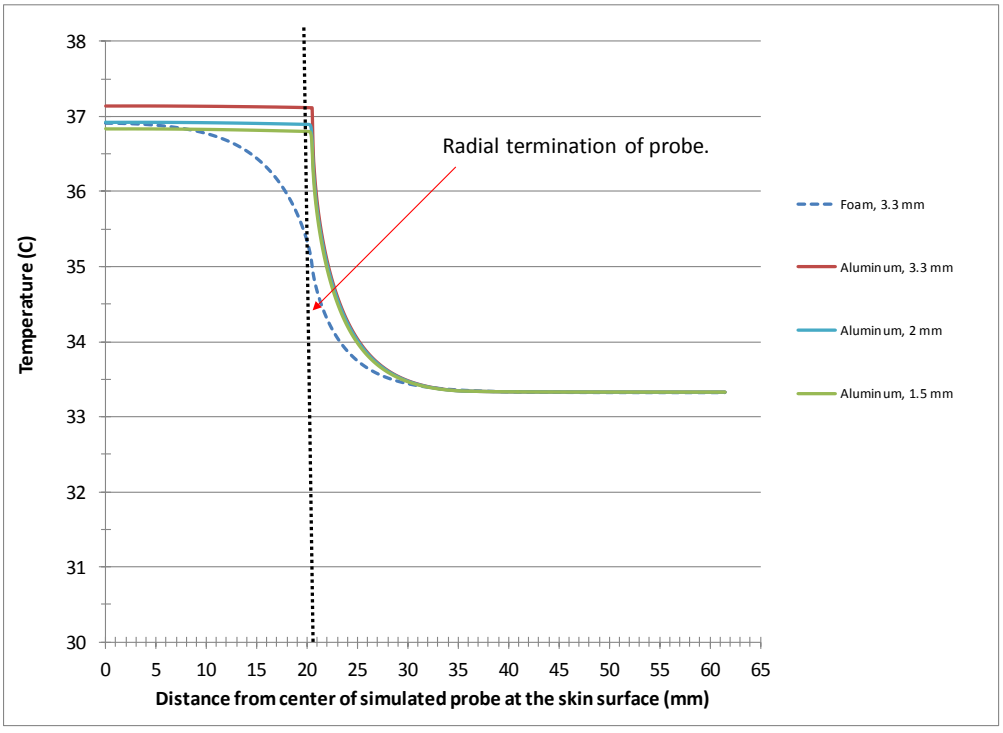

Figure 4-3. Steady-state radial temperature distributions comparing foam to various aluminum thicknesses for the original probe radius of 20.5 mm.

The implementation of aluminum disk having radius of 10 mm, half of the original, gives rise to results set forth in Figure 4.4. It is seen from the figure that constancy of the radial temperature distribution continues to hold for the half probe radius.

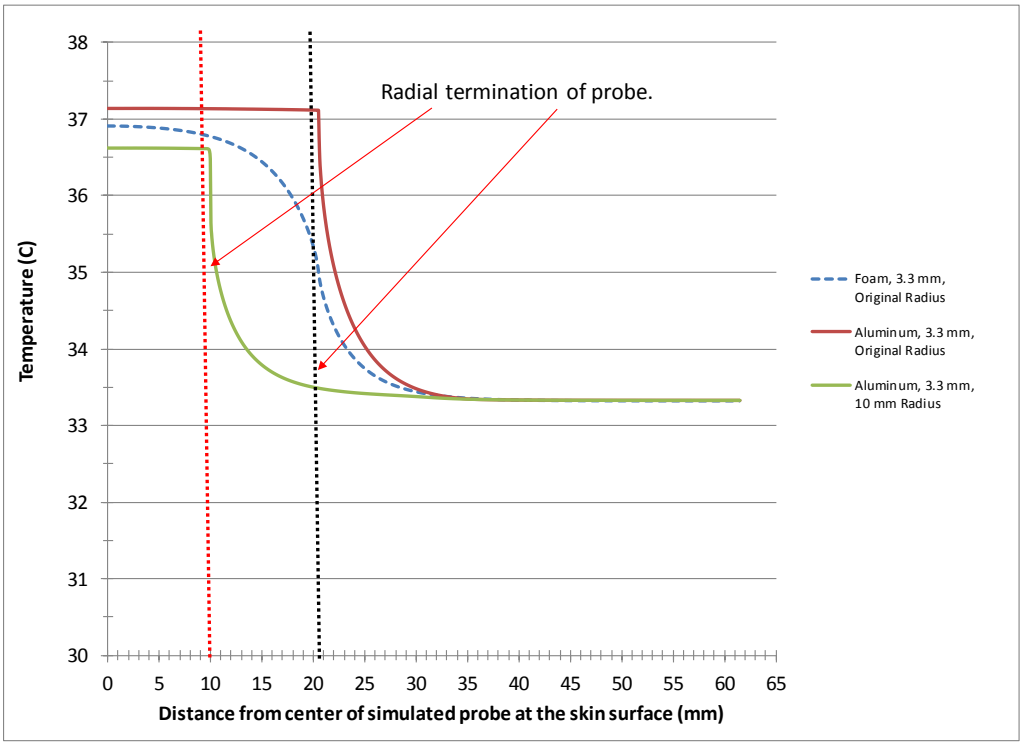

Figure 4-4. Radial temperature distribution comparing foam, original probe radius of 20.5 mm, and reduced radius of10 mm for aluminum.

It remains to examine whether the reduced radius probe has temperature response time that remains satisfactory. To this end Figure 4.5 has been prepared. The figure is restricted to Scenario 2 based on the previous findings that Scenario 1 has undesirable temperature response. Two curves are displayed in the figure, one for the original probe design based on a foam disk of 20.5 radius and the other for an aluminum disk of 10 mm radius, with both disks having common thickness of 3.3 mm. The figure shows a response time for the aluminum disk that is substantially less 0.5 minute. On the other hand, the foam disk response is about eight minutes. It is believed that the same rapid response would hold for thinner aluminum disks such as a thickness 1.5 mm.

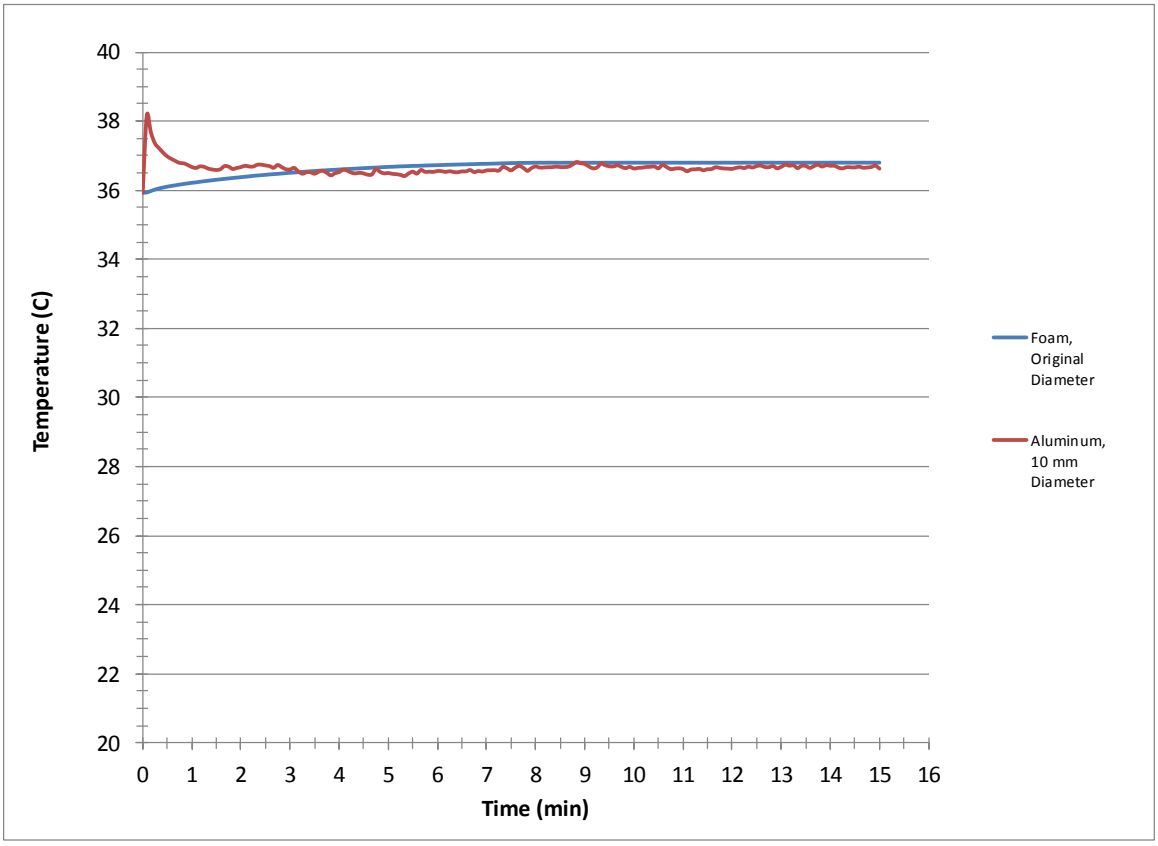

Figure 4-5. Response of skin temperature comparing foam to a 10 mm diameter aluminum probe.

4.4 Outcomes of Chapter 4

The focus of this chapter was to quantify the temporal and spatial response of the predicted skin surface temperature to a change in material of the disk that supports the heater. Although the investigation included both Scenarios 1 and 2, it became evident that the response to Scenario 1 of all investigated probe manifestations could not be made to be satisfactory. On the other hand, it was demonstrated that a great improvement in response time could be achieved for Scenario 2 by replacing the original foam disk by an aluminum disk.

Regardless of the thickness of the aluminum disk, the time to achieve steady state was found to be less than 0.5 minutes.

Another outcome of the chapter was the demonstration that the aluminum-based probe could function equally well if its radius were cut in half. This outcome was supported by two independent findings. One of these is that the radial temperature distribution along the skin remained constant for both the original and diminished probe radius. The other is that the response time corresponding to small radius probe was of the same order as that for the larger radius probe.

CHAPTER 5

Experimental Evaluation of Baseline Fluid Warming System

5.1 Introduction

Fluid warming devices are widely utilized to provide body fluids of appropriate temperature such as blood and saline during the course of operations. The need for blood or saline infusion may be due to many causes. Hypothermia often occurs in anaesthetized or sedated patients [37], especially in trauma patients [38]. Rapid infusion of unwarmed blood may result in lowering the core temperature [39] which in effect cause cardiac arrhythmias, coagulopathy, and increased mortality rates [40, 41]. However, regardless of the cause, the need for a fluid-warming device is universal.

The research described in this chapter was motivated by the need to quantify the characteristics of the current version of a widely accepted and utilized fluid warming device [42, 43]. It is intended to use this information as a baseline on which to design an improved version of the device to more effectively deliver the therapeutic action. The guidelines for the redesign of the device will be provided by the use of numerical simulation. That simulation, to be set forth in Chapter 6, requires validation which will be provided by comparing the predictions of the simulation to the experimental findings of the present chapter. Once verified, the simulation model will be used to create an optimized design of the fluid warming device.

5.2 Description of a fluid warming device

5.2.1 Overall device description

An external view of the fluid warming device showing its housing is presented in Figure 5-1. As seen there, the housing incorporates a slot for the insertion of a key heat exchanger component, termed the *disposable*, which warms either a room-temperature fluid (saline) or a refrigerated fluid (blood) to a preselected temperature appropriate for infusion into a human body. The casing is equipped with a digital display which shows the temperature of the fluid at the exit of the device. Also, there is a handle which enables convenient transport, and fittings which are used for affixing the device to an IV pole.

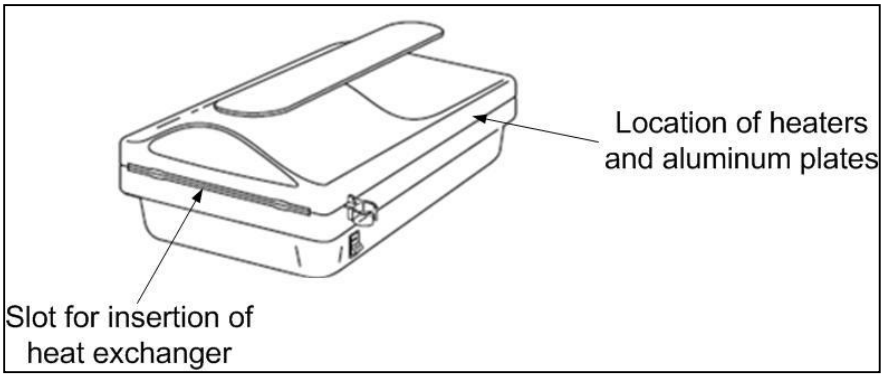

Figure 5-1. External view of the fluid warming device.

A second external view, displayed in Figure 5-2, shows the disposable partly in place. The tubing that can be seen in the figure provides the means by which fluid is introduced into the heat exchanger and subsequently, after being heated, is extracted.

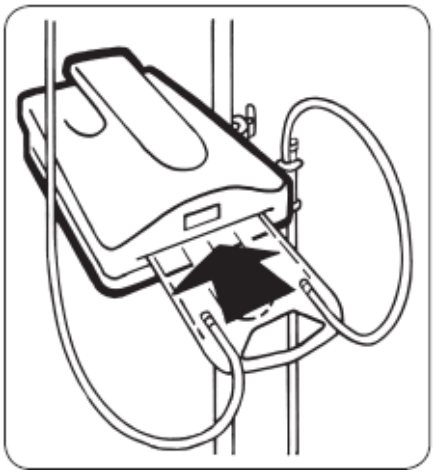

Figure 5-2.External view of the fluid warming device with the disposable partly in place.

5.2.2 The disposable

A definitive view of the disposable is shown in Figure 5-3. The disposable is constructed of polyvinylchloride (PVC) whose wall thickness is 0.004 inches. Upon entering the disposable, the fluid encounters the first of four legs of a serpentine path. At the downstream end of the final leg, the heated fluid exits into a plastic tube which conveys it to a point of use. Each leg of the disposable is actually a flat rectangular duct. The duct dimension that is seen in the figure is one inch. The depth of each duct is 0.040 inches so the rectangular-cross-sectional aspect ratio is 25.

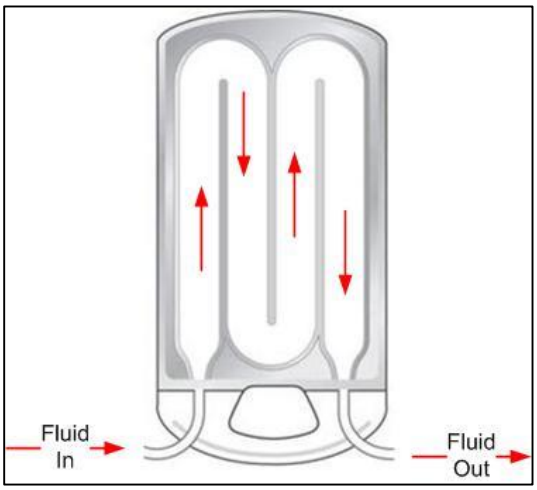

Figure 5-3. Detailed view of the disposable.

The fluids in question are delivered to the disposable via a circular tube. Immediately upon entering the disposable, the fluid encounters a tapered enlargement. The total angle of enlargement is approximately 30 degrees. It has been demonstrated [47] that for total enlargement angles greater than seven degrees, the flow does not follow the contour of the bounding walls. Such flows are termed separated flows.

It is expected that the flow separation will be neutralized before the fluid arrives at the 180° bend at the exit of the first leg. The fluid exiting that bend will have a highly nonuniform velocity profile and may experience a new flow separation as it executes a 180-degree turn. Once again, it is expected that wall friction will neutralize both the nonuniformity and flow separation prior to the exit of the second leg. This pattern of flow disturbance and neutralization is expected to continue until the exit of the disposable. Just downstream of the exit, there is a contraction whose action will tend to further regularize the flow.

5.2.3 The heaters

The heating of the participating fluid is accomplished by thermal interaction of the disposable with specially designed and fabricated heating elements. A pictorial view of one of the heating elements is displayed in Figure 5-4. The pictured heating element interfaces with one of the surfaces of the disposable. An identical heater interfaces with the other surface of the disposable. For orientation purposes, it is relevant to note that the fluid enters the disposable at the upper left of the photograph and exits at the lower left. Each heater consists of traces of resistance material deposited on an aluminum plate whose thickness is 0.25 inch.

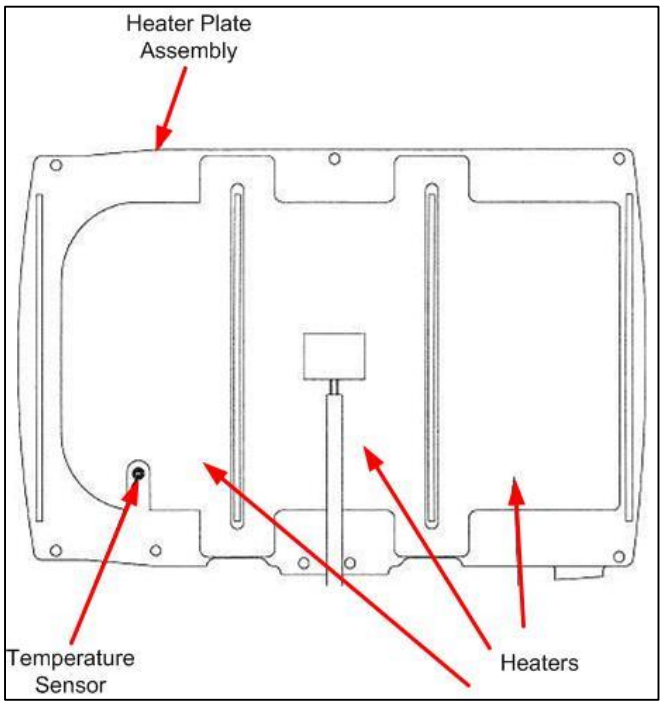

Figure 5-4. Pictorial view of one of the heating plates for the fluid warming device.

The wiring is such that the leftmost and central heater banks provide the same heating power density, whereas the power density at the rightmost heater is at a lesser level. Once the heaters have been set up, their power apportionment is fixed.

5.2.4 Temperature sensor

Heater operation is on an ON/OFF protocol. At the lower left of the Figure 5-4, just upstream of the fluid exit, is an installed temperature sensor. A detailed diagram of the sensor and its installation is exhibited in Figure 5-5. As seen there, the temperature of the sensor is influenced both by its contact with the disposable and by its aluminum-plate surroundings. The sensor is a Resistance Thermometer Device (RTD). The heater On operation is activated when the measured temperature is 0.1^{o} C below the setpoint value. The Off operation is initiated when the temperature measurement is 0.1^{o} C above the setpoint value.

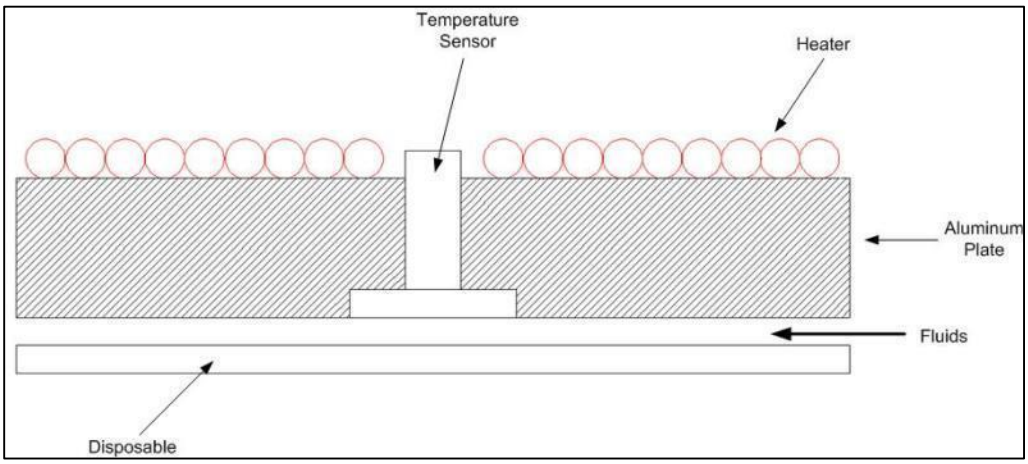

Figure 5-5. Detailed diagram of installed temperature sensor.

In Figure 5-6, the composition of the temperature sensor is shown. It consists of a RTD element epoxied into a tin-plated copper case. Twenty-two gauge TFE (teflon) stranded wires are adhered to the RTD element. Polyolefin shrink tubing encapsulates the entire temperature sensor assembly. The resistance of the RTD element used in the experiment is 100 Ohm at 0ºC, Platinum DIN Class "A". This type of element provides high accuracy with a temperature range between -50ºC to 135ºC.

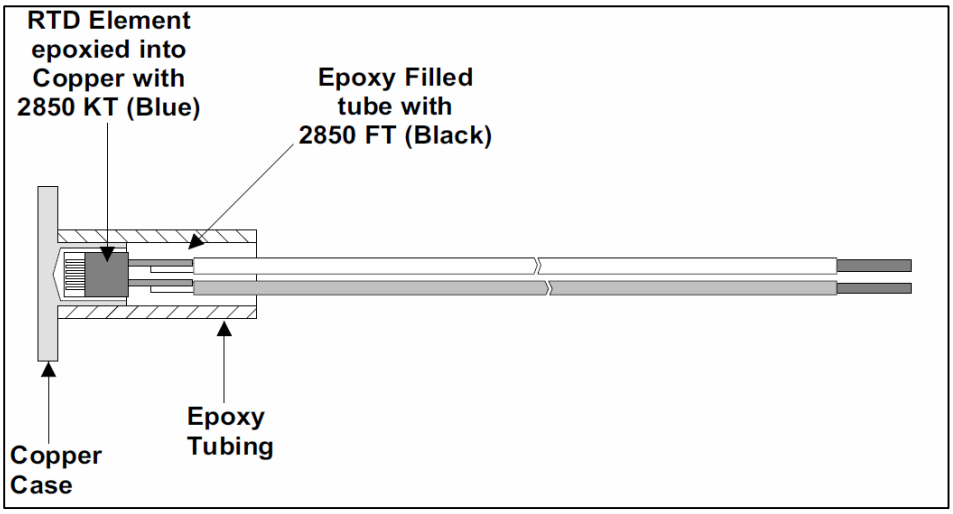

Figure 5-6. Detailed diagram of composition of temperature sensor used.

5.3 System Operations

5.3.1 Start-up transient

The critical issue with regard to startup is the recognition that no fluid is to be infused into the patient at temperatures below 20^{o}C [48, 63]. To deal with this restriction, a startup procedure is implemented. Prior to the initiation of startup, clamps situated both upstream and downstream of the disposable are closed. To initiate startup, power is applied to the heaters in order to bring the internal hardware up to the temperature setpoint value. At that moment, the clamps are opened and saline is infused into the disposable where it remains until warmed fluid is needed by the patient. If blood is required, the upstream and downstream clamps are both open, thereby admitting blood into the disposable. The blood displaces the saline and continues to flow through the warming unit until no further infusion is needed by the patient.

5.3.2 Steady-state operation

As long as the temperature measured at the exit of the disposable is at the setpoint value, steady-state operation will occur. On the other hand, if the measured temperature exceeds that of the setpoint, the heating power will be turned off. This action will reduce the measured temperature and will cause the heating to resume if its value falls 0.1^{o}C below the setpoint. This On/Off operation, if it occurs, corresponds to a periodic steady state.

5.3.3 Stop-flow condition

When the attending physician deems that no further fluid infusion is needed, the output of the heating unit must be halted immediately. This outcome is achieved by closing a clamp that is positioned downstream of the exit of the heating unit. This clamping operation does not automatically discontinue the delivery of electric power to the heaters. As a consequence, it is highly likely that the measured exit temperature will exceed the

setpoint value, resulting in a cessation of the delivered power. However, heat may still be transferred to the fluid that is captive in the disposable, the heat source being the elevated temperature of the aluminum walls that bound the disposable.

Since it is likely that further infusion will be needed at a later time, it is imperative to maintain the viability of the blood that is captured within the disposable during the stop-flow period. It is also recognized that the viability of the blood would be destroyed if its temperature were to exceed 48^{o}C [44, 64]. To avoid that overtemperature, the heat capacity of the aluminum plates has to be designed so that the heat outflow from the plates into the captive fluid cannot exceed the critical 48^{o}C value.

5.4 Data collection and post processing

The elements that comprise of the experimental setup system are shown in Figure 5-7. To facilitate explanation of the elements, it is convenient to follow the path of fluid flow. For the experiments, the working fluid was saline.

The starting point of the flow path is the peristaltic pump. Pumps of this type impart a periodic fluctuation in the flow rate. The output of the pump is ducted to a refrigerated bath by means of plastic tubing. A separate length of plastic tubing is used to extract the cooled fluid from the bath. This decoupling of the lines of input and extraction are sufficient to dampen the fluctuations imparted by the peristaltic pump.

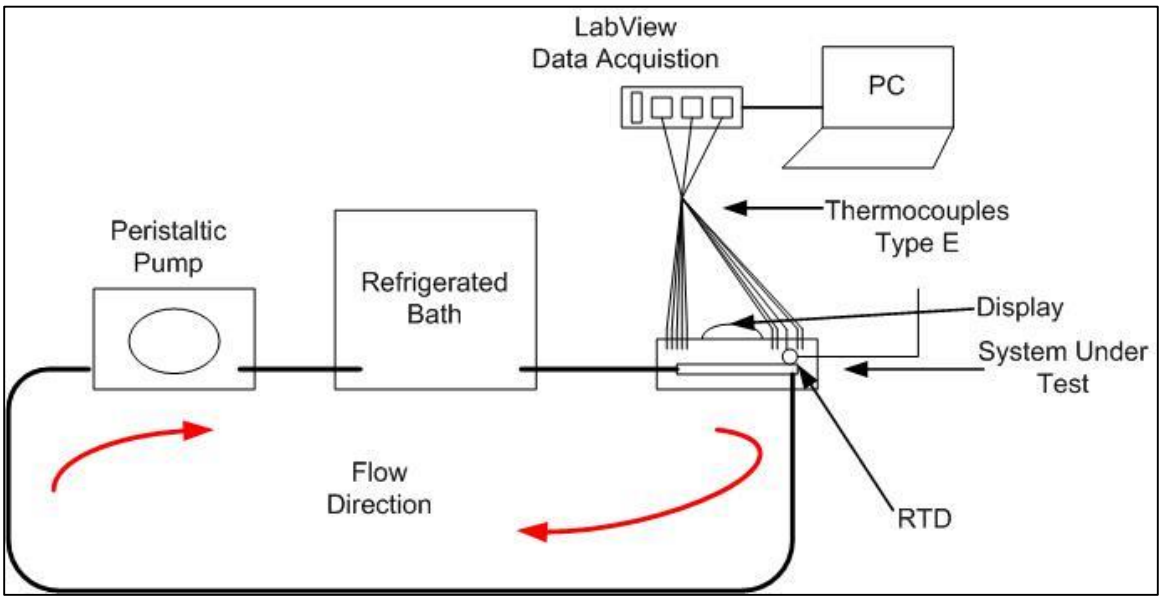

Figure 5-7. Experimental test setup.

The fluid enters the disposable at a temperature of 10^{o}C and experiences the heating process that has been described earlier in this chapter. The fluid exiting the disposable is looped back to the peristaltic pump, thereby closing the system. The returned fluid is tempered while passing through the refrigerated bath.

Further inspection of the Figure 5-7 shows the manner of temperature measurement and control. The temperature measured by the embedded RTD device is sent to the controller, where it is compared with the preset setpoint value. As explained earlier, that comparison dictates the off-on cycle of the heating power. Also shown in Figure 5-7 are leader lines that schematically depict thermocouple leads. These thermocouples are attached to one of the heating plates, and the locations of those thermocouples are in Figure 5-8. It is relevant to note that the thermocouples are attached to the face of the heating plate which interfaces with the disposable. The thermocouple outputs are read and recorded by a LabView^{TM} data acquisition system. That system converts the thermocouple EMFs to temperatures. The temperatures are displayed as a function of time on the screen of a monitor.

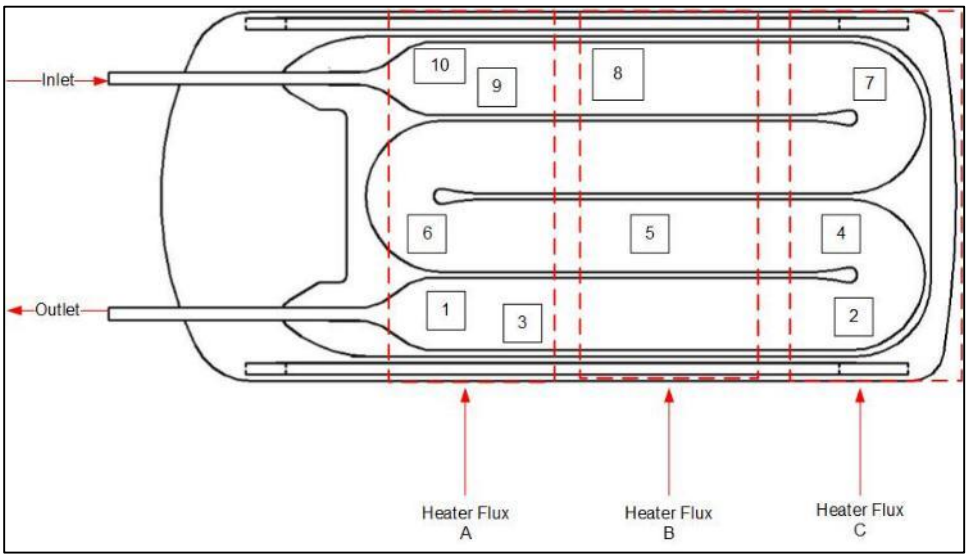

Figure 5-8. Map of thermocouple locations on disposable with locations of heaters superimposed.

In addition to the aforementioned measurement of the heater face temperatures, thermocouples were also installed to measure the temperature of the fluid entering the disposable and leaving the disposable. The rationale motivating these placements is the need to know the fluid bulk temperatures at inlet and exit. The knowledge of those temperatures, used in conjunction with the First Law of Thermodynamics, enables the calculation of the heat absorbed by the fluid as it passes through the disposable.

The installation of the fluid-measuring thermocouples is shown in Figure 5-9. To facilitate this measurement, a tee-joint is inserted in the plastic tubing which respectively delivers fluid to the inlet and exit of the disposable. The thermocouples enter the respective tee-joints through their off-line openings and are positioned in the inline path of the fluid.

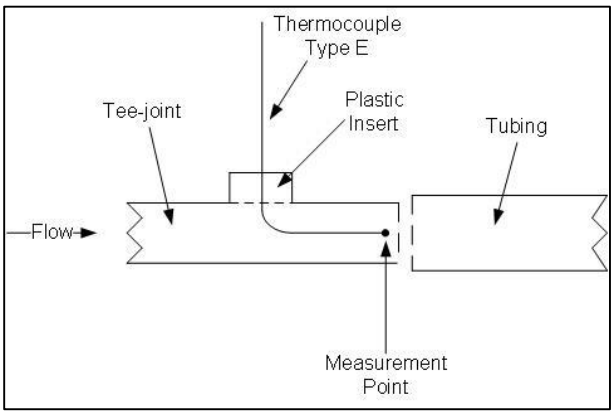

Figure 5-9. Deployment of a thermocouple to measure the temperature of the fluid entering the disposable and leaving the disposable.

The bulk temperature is sometimes referred to as the mixed-mean temperature. It is the mass-weighted-average temperature of the fluid that passes through the entire cross section. This recognition motivates a concern that a single-point temperature measurement as indicated in Figure 5-8 might differ from the mixed-mean temperature. To examine this concern, a special experiment was performed in which the downstream end of the tee-joint was open, and the fluid issuing from it was captured in a beaker equipped with a magnetic stirrer and a thermocouple. The in-line thermocouple reading was compared with that of the thermocouple immersed in the well-stirred bath. Typically, the difference in the temperature readings was approximately 0.3^{o}C. This difference may be compared with the temperature difference between the inlet and exit of the disposable, which is typically in the order of 17^{o}C. In this light, the temperature measurement approach using the tee-joint was judged to be adequate.

The thermocouple wire used for the temperature measurements is type E. The choice of this type was made on the basis of three characteristics: (a) highest EMF per degree among all common thermocouple pairs, (b) lowest thermal conductivity among all common thermocouple pairs, and (c) inert to moisture. The wire diameter chosen for the fabrication of the thermocouple was 0.005 inches (0.127 mm), thereby further minimizing possible heat conduction along the thermocouple wires [65].

A unique technique was used to affix the thermocouples to the face of the aluminum heater plates. As a first step, a groove was indented into the plate surface by means of a sharp-pointed chisel made of hardened steel. The aluminum displaced by this operation was pushed to the sides of the groove. The thermocouple junction was carefully inserted into the groove, and a flattened rod was used to move the displaced aluminum atop the embedded thermocouple. As a result, the thermocouple junction was buried within the plate to a depth of approximately 0.001 inch (0.0254 mm).

5.5 Results and discussion

5.5.1 Patterns of fluid flow

The pattern of fluid flow varies along the length of the serpentine flow passage in the disposable as various geometric features are encountered. The first feature is a rapidly enlarging cross-sectional area as the fluid passes from a small-diameter tube into the inlet of the passage. As mentioned earlier, the rapid enlargement gives rise to a zone of flow separation and recirculation since the fluid is not able to follow the contour of the bounding wall. To verify this hypothesis, a flow visualization experiment was performed by means of dye injection.

Figure 5-10 illustrates the experimental approach. The figure shows the part of the flow passage that is immediately downstream of the inlet. The location of dye injection is clearly indicated. A small bolus of blue dye was introduced into the flow by a syringe. Care was taken to ensure that the tip of the syringe was situated very close to the wall of the passage and did not penetrate the core of the flowing fluid. The injected bolus remained in the near-wall region where it was injected, as can be seen in Figure 5-10. The captive nature of the injected bolus is a clear indication of the captive eddy which characterizes fluid recirculation.

Figure 5-11 is included here to validate the presence of the recirculation zone. It displays the streamline pattern of the flow entering the passage, obtained by numerical simulation (to be described in Chapter 6). The simulation outcome also exhibits a zone of flow separation.

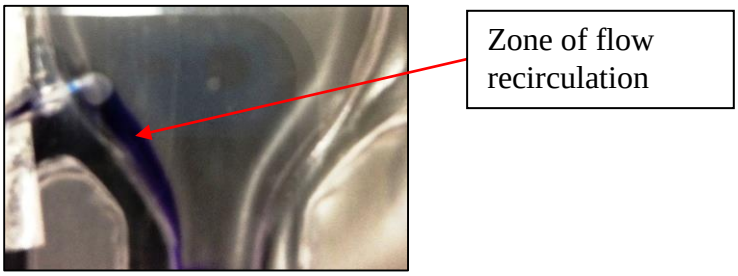

Figure 5-10. Photograph displaying the dye-injection visualization of a portion of the recirculation zone.

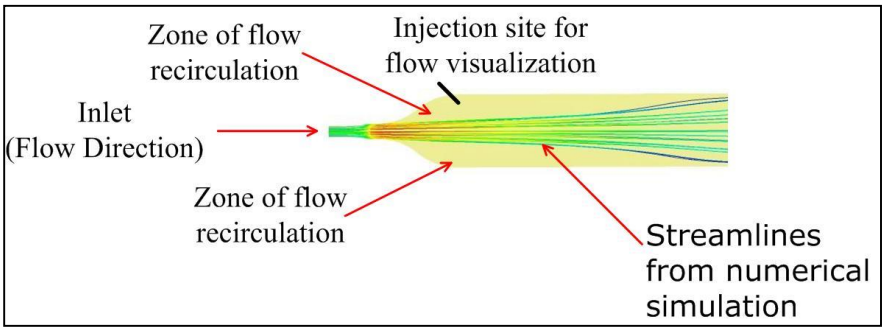

Figure 5-11. Numerically predicted recirculation zones at the inlet of the passage and the specification of the point of dye injection.

5.5.2 Temperature results

Temperature measurements were obtained for two different operating conditions. For operating condition #1, the following operating variables were imposed: (a) inlet gauge pressure = 300 mmHg, (b) inlet temperature = 10^{o}C, (c) saline flow rate = 30 L/hr, and (d) ambient air temperature = 20^{o}C. The second operating condition, #2, is defined by operating variables (a), (b), and (d) from the foregoing, with the saline flow rate of 9

L/hr. The temperature results for these operating conditions are conveyed in Figures 5-12 and 5-13, respectively. Attention will first be focused on Figure 5-12.

5.5.2.1 High flow rate (30 L/hr)

Figure 5-12 displays the timewise variations of the temperature at the locations, shown in Figure 5-8, of the 10 thermocouples that were affixed to the surface of one of the heater plates that is in contact with the disposable. In addition, the temperatures at the fluid inlet and exit are also given. The temperature of the ambient surrounding the experimental device is also shown in the figure.

Attention is directed to the two black vertical lines which correspond respectively to the moment of time at which fluid flow was initiated and to the instant at which stop flow was imposed. For times between t = 0 and the initiation of fluid flow, the disposable was filled with stagnant fluid. This time interval was provided to enable the aluminum heater plates and the stagnant fluid to come up to near-operating temperature.

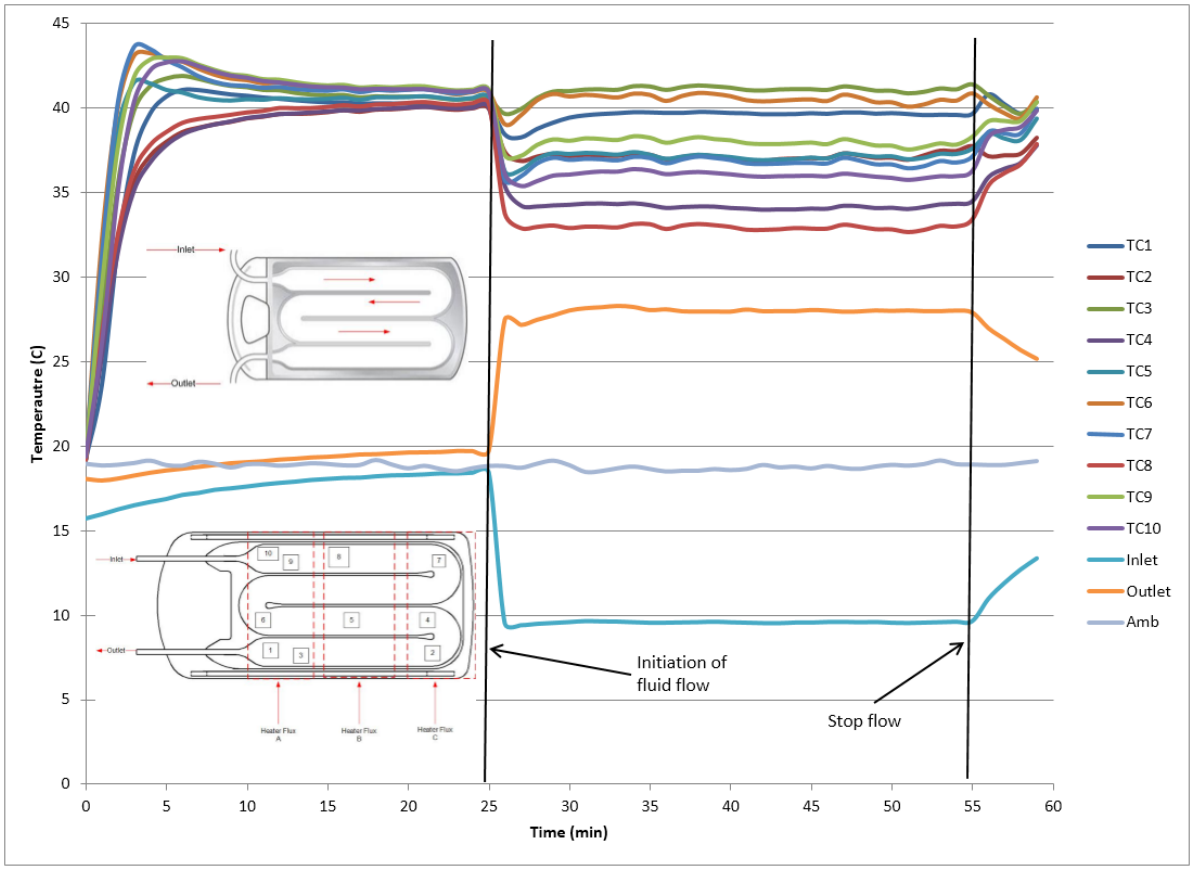

Figure 5-12. Temporal temperature variations for operating condition #1 with a flowrate of 30 L/hr.

Inspection of the figure reveals a number of thermal responses to the imposed operating conditions. At the start of heating when there is no fluid flow, a sharp temperature rise at all thermocouple locations is in evidence. The temperatures measured upstream (inlet) and downstream (exit) of the disposable experience incremental increases due only to heat conduction. Further examination of the thermocouple responses in the time period prior to fluid flow initiation reveals temperature overshoots at the majority of the measurement locations. This behavior is an artifact of the control system which turns off the heater power at temperatures that exceed the setpoint of 41°C. It may also be noted that three of the measured temperatures do no display overshoot behavior. This may be attributed to either a near-edge positioning or the presence of a stiffening bar.

Focus will now be shifted to the period of time between the onset of fluid flow and before the imposition of the stop-flow condition. Immediately after the initiation of fluid flow, all measurement locations experience a temperature drop off, as does the fluid inlet temperature. In contrast, the fluid outlet temperature experiences a sharp rise. Subsequently, a steady-state operation sets in during which all of the measured temperatures are more or less independent of time.

The behavior of the array of thermocouples is not uniform during the aforementioned time interval. The majority of the thermocouples experience temperature recovery subsequent to their initial drop offs. That recovery is due to the heating of the fluid from the aluminum plates. The extent of the recovery is different at different measurement locations. The differences in the extent of the recovery can be attributed to one of two causes: (a) the proximity of the location in question to the fluid inlet and (b) the power applied to the heating segment where the thermocouple is situated.

The imposition of the stopflow condition gives rise to a variety of temperature responses. In that regard, it is relevant to note that the stopflow condition does not automatically turn off the heater power. The behaviors of the inlet and outlet temperatures follow expected patterns, specifically, the inlet temperature rises and the outlet temperature drops. The embedded thermocouples whose temperatures are highest experience a slight increase due to stop flow, and this increase results in a cutoff of heater power. The power cutoff causes a temperature drop at those locations. At all other thermocouple locations, the response to stopflow is an increase of temperature. This behavior is a result of thermal energy flowing from the aluminum heater plates into the stationary fluid.

5.5.2.2 Low flow rate (9 L/hr)

Focus is now redirected to condition #2 which is defined by its flow rate of 9 L/hr. Aside from this crucial difference, all of the other operating conditions are identical to those of

condition #1. The temperature-time results for condition #2 are exhibited in Figure 5-13. The structure of the figure is similar to that used for Figure 5-12.

An overall inspection of Figure 5-13 suggests certain similarities with what has been displayed in Figure 5-12, but also reveals some significant differences. One of the major differences is that the temperature traces for the period of no flow have been omitted from Figure 5-13 since the results for that period are indifferent to the magnitude of the flowrate that is imposed later. The timescale for this figure begins at the onset of fluid flow. During this period, the vertical ordering of the respective temperatures differ slightly from that which was existent in Figure 5-12.

The most major observable difference between the figures during the steady-state is the outlet temperature. At the lower flow rate, the residence time of the fluid in the disposable is considerable longer than that experienced by the fluid at the higher flow rate. As a consequence of the longer residence time, the fluid is considerably more heated and experiences higher temperatures. At stop flow, the temperature traces seen in Figure 5-13 all experience a common behavior which is a temperature rise.

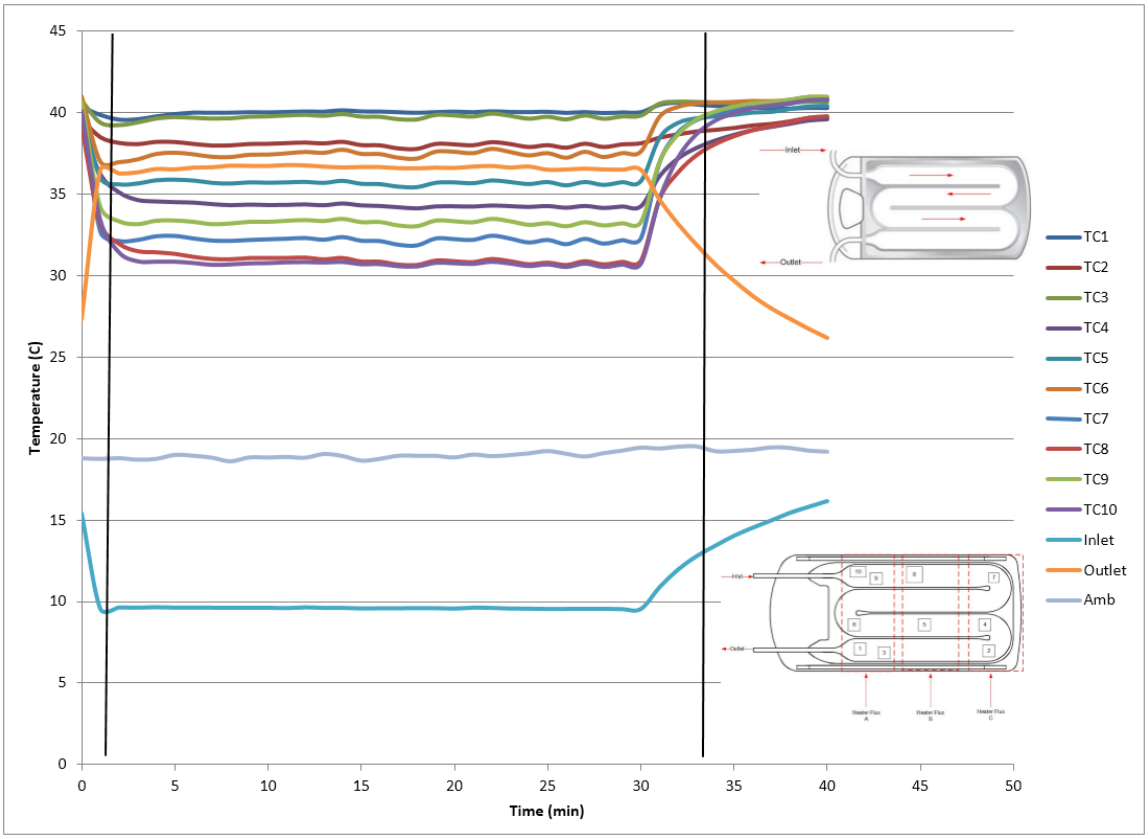

Figure 5-13. Temporal temperature distributions for operating condition 2 with a flowrate of 9 L/hr.

5.6 Outcomes of Chapter 5

Careful experimentation techniques are important in order to obtain an accurate baseline performance measurement of a fluid warming device. The results of the baseline experiments provide the framework for the simulation modeling and results in Chapter 6. The technique of affixing a thermocouple to the aluminum plate or creating bulk temperature measurement points aid in the obtainment of accurate temperature measurements.

Results of the experiment show recirculation zones exist at the inlet passages of the system. This is visualized using a dye injection method. Temperature measurements were obtained for two operating conditions with low and high flowrates of 9 L/hr and 30

L/hr respectively. Four distinct time intervals are evaluated for the experiments: (a) the heating unit is turned on, (b) fluid flow is initiated, (c) steady state is achieved, and (d) stop flow is imposed. A key distinction between the two operating conditions is in the duration of the residence time of the fluid in the disposable. At the lower flow rate, the residence time of the fluid in the disposable is considerable longer than that experienced by the fluid at the higher flow rate. As a consequence of the longer residence time, the fluid is considerably more heated and experiences higher temperatures.

Furthermore, the stopflow condition gives rise to a variety of temperature responses. One of the major responses is that at all thermocouple measurement locations that pertain to the fluid in the disposable, there is an increase of temperature values. This behavior is a result of thermal energy flowing from the aluminum heater plates into the stationary fluid.

CHAPTER 6

Numerical Simulation of Fluid Warming Device

6.1 Introduction

The philosophy underlying the present approach is that the synergistic use of the numerical simulation and experimentation provides an optimum design methodology. To implement this approach, the first step is to create a simulation model which precisely mimics the baseline experiments described in Chapter 5. The next step is to compare the predictions of the simulations to the corresponding experimental results. This type of validation is essential to the intended extension of the simulation model to be a predictive tool for the determining an optimum design.

This chapter is subdivided into two parts. The first part is focused on modeling the baseline case which constituted the experimental situation of Chapter 5, and the second part is to extend the simulation model to serve as a design tool.

6.2 Simulation of the experimental situation for the baseline case

6.2.1 Geometry of the model

The major components of the modeled geometry are the disposable and the heater plates. A drawing of the disposable as it was implemented in the simulation model is displayed in Figure 6-1. With the heater plates, the heater windings that are shown in Figure 5-4 could not conveniently be reproduced as such. Rather, as illustrated in Figure 6-2, three zones, each assigned a uniform heat flux, were used to model the heater windings. Zones 1 and 2 were modeled as having the same heat flux, while zone 3 was assigned a lesser heat flux. The heat flux values employed in the simulation were those of the experiment.

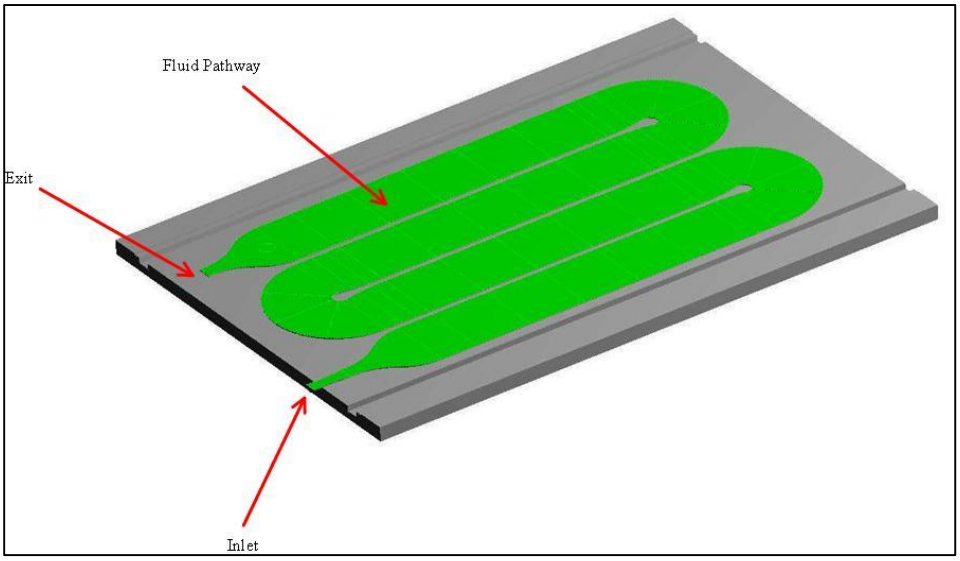

Figure 6-1. Detail of fluid pathway (colored green) used in the simulation.

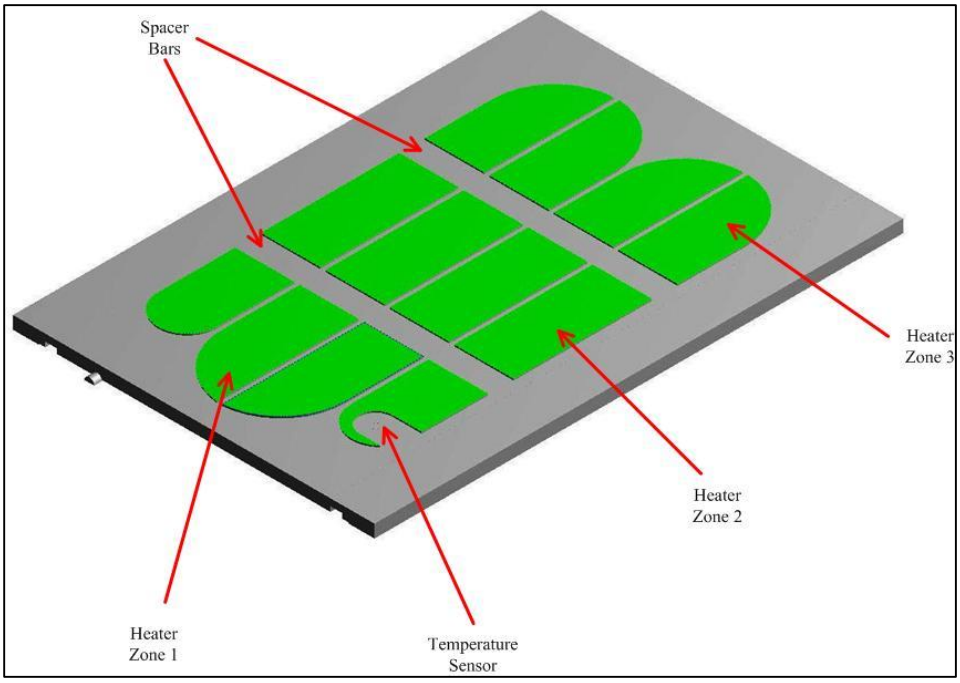

Figure 6-2. Detail of the three separate heater zones (colored green) used in simulation with call outs for the location of the heaters and spacer bars. The green zones for the first and second heaters were specified to have the same uniform heat flux. The heat flux for the third heater was also uniform, but of lower magnitude. The unheated surface is depicted in gray. That surface was treated as adiabatic.

Since the components that were identified in the preceding paragraphs possessed side-to-side symmetry, the solution domain was selected to incorporate this feature.

6.2.2 Governing equations

The following section outlines the conservation equations used to model the physics of the fluid flow situation. These conservation equations are written for both transient and steady-state, three-dimensional fluid flow, and heat transfer. When heat transfer occurs in two media which interact with each other, the resulting problem is designated as conjugate.

The approach to solution of the problem is based on first solving for the steady-state velocity and temperature distributions in the fluid and the temperature distribution in the solid media. When the stop-flow condition is imposed, a transient is initiated. In all of the forthcoming equations, it is assumed that the thermophysical properties of the participating media are constant.

6.2.2.1 Steady-state case

For the steady-state situation, the mathematical description of the fluid flow includes the momentum conservation equations in the *x*, *y*, and *z* directions and the equation of mass conservation. For the *x*-direction, momentum conservation is described in Equation (6-1). The *y*- and *z*-conservation equations may be obtained from this same equation by a rotation of the coordinates and velocities. The prototypical momentum conservation is

$$\rho\left(\frac{\partial u^2}{\partial x}+\frac{\partial uv}{\partial y}+\frac{\partial uw}{\partial z}\right)=-\frac{\partial p}{\partial x}+\mu\left(\frac{\partial^2 u}{\partial x^2}+\frac{\partial^2 u}{\partial y^2}+\frac{\partial^2 u}{\partial z^2}\right) \tag{6-1}$$

The terms that appear on the left-hand side of the equation represent momentum conservation, whereas the terms on the right correspond to the forces, respectively pressure and viscous.

The mass conservation equation, which is also used for fluid flow calculations during both the transient and steady-state operations, is a scalar which is

$$\frac{\partial u}{\partial x}+\frac{\partial v}{\partial y}+\frac{\partial w}{\partial z}=0 \tag{6-2}$$

The absence of time derivative is due to the density being independent of time.

For the mathematical description of the heat transfer for the steady-state situation, separate consideration has to be given to each of the three participating media since they have distinct thermal physical properties. For the flowing fluid (subscript *f*),

$$(pc)_f\left(\frac{\partial uT_f}{\partial x}+\frac{\partial vT_f}{\partial y}+\frac{\partial wT_f}{\partial z}\right)=k_f\left(\frac{\partial^2 T_f}{\partial x^2}+\frac{\partial^2 T_f}{\partial y^2}+\frac{\partial^2 T_f}{\partial z^2}\right) \tag{6-3}$$

On the left side of this equation, convection is represented, while the right side consists of the conduction terms. This equation represents the First Law of Thermodynamics for the steady state. It states that the rate of energy inflow must equal the rate of energy outflow for an infinitesimal control volume that surrounds any point in the flow. The heat transfer process in the disposable, which is a plastic (subscript *p*), is conduction alone, so that

$$\frac{\partial^2 T_p}{\partial x^2}+\frac{\partial^2 T_p}{\partial y^2}+\frac{\partial^2 T_p}{\partial z^2}=0 \tag{6-4}$$

The aluminum plates (subscript *a*), which constitute the heat spreaders, also transfer heat by conduction alone. The equation which governs that heat transfer is

$$\frac{\partial^2 T_a}{\partial x^2} + \frac{\partial^2 T_a}{\partial y^2} + \frac{\partial^2 T_a}{\partial z^2} = 0 \qquad (6\text{-}5)$$

Taken together, Equations (6-1) through (6-5) constitute a set of five partial differential equations. It might appear that the first three of these can be solved independently from the rest because the fluid properties are taken to be independent of temperature. However, the thermal boundary conditions for the flowing fluid are conditions of continuity which connect the fluid and the solid-media temperatures at their interface. This connection requires that all of the foregoing partial differentiation equation must be solved simultaneously.

6.2.2.2 Transient case

For the transient that follows the stop-flow action, the governing equations that are presented previously for the steady-state case have to be generalized to include a time-dependent term. I n particular, Equation (6-1) becomes

$$\rho\left(\frac{\partial u}{\partial t} + \frac{\partial u^2}{\partial x} + \frac{\partial uv}{\partial y} + \frac{\partial uw}{\partial z}\right) = -\frac{\partial p}{\partial x} + \mu\left(\frac{\partial^2 u}{\partial x^2} + \frac{\partial^2 u}{\partial y^2} + \frac{\partial^2 u}{\partial z^2}\right) \qquad (6\text{-}6)$$

With regard to mass conservation, Equation (6-2), there is no change since the density is constant for an incompressible medium. Finally, the conservation of energy equation, after modification, becomes

for the fluid:

$$(\rho c)_f\left(\frac{\partial T_f}{\partial t} + \frac{\partial u T_f}{\partial x} + \frac{\partial v T_f}{\partial y} + \frac{\partial w T_f}{\partial z}\right) = k_f\left(\frac{\partial^2 T_f}{\partial x^2} + \frac{\partial^2 T_f}{\partial y^2} + \frac{\partial^2 T_f}{\partial z^2}\right) \qquad (6\text{-}7)$$

and for the disposable plastic:

$$(\rho c)_p \frac{\partial T_p}{\partial t} = \frac{\partial^2 T_p}{\partial x^2} + \frac{\partial^2 T_p}{\partial y^2} + \frac{\partial^2 T_p}{\partial z^2} \quad (6\text{-}8)$$

and for the aluminum:

$$(\rho c)_a \frac{\partial T_a}{\partial t} = \frac{\partial^2 T_a}{\partial x^2} + \frac{\partial^2 T_a}{\partial y^2} + \frac{\partial^2 T_a}{\partial z^2} \quad (6\text{-}9)$$

To facilitate the numerical solutions, it is necessary to specify the properties of the participating media. This information is conveyed in Table 6-1.

Table 6-5. Thermophysical properties of the participating media [45]

Material	Density	Specific Heat	Thermal Conductivity	Dynamic Viscosity
	kg/m^3	J/kg-C	W/m-C	kg/m-s
Aluminum	2750	880	142	-
PVC	1400	1050	0.16	-
Water	1000	4187	0.60	0.000890

6.2.2.3 Inlet velocity

To characterize the flow, it is important to calculate the Reynolds number in order to assess if the flow is laminar or turbulent. The following equation is used to obtain the Reynolds number

$$Re = \frac{\rho U D_H}{\mu} \quad (6\text{-}10)$$

in which U is the mean velocity, D_H is the hydraulic diameter, and ρ and μ are the density and viscosity of the fluid, respectively.

Since the flow passages within the disposable are rectangular ducts of very large aspect ratio (approximately 25), the hydraulic diameter D_H is very nearly equal to twice the

height of the passage. Therefore, D_H is approximately to 0.00195 m. Experimental research on developing flow in rectangular ducts [40] for aspect ratios from 1:1 (square duct) to 51:1 (parallel-plate channel) showed that flow was laminar for Reynolds number up to 3000. The calculated Reynolds number for the 30 L/hr case is 483, thus characterizing the flow as laminar.

6.2.3 Boundary conditions

To complete the specification of the problem, it is necessary to state boundary conditions. Since the differential equations are elliptic in space, it is necessary to specify two boundary conditions for each coordinate. On the other hand, the equations are parabolic in time, so that only one boundary condition need be specified for time.

It is convenient to subdivide the specification of the boundary conditions into those for fluid flow and those for temperature. At any solid-liquid interface, it is required that the two velocity components (perpendicular and parallel) be identically zero. At the inlet of the disposable, the cross section of the passage is round, so that the inlet velocity profile is

$$Inlet\ Velocity = 2 * MeanVelocity\left[1 - \left(\frac{r}{R}\right)^2\right] \quad (6\text{-}11)$$

With regard to the fluid exit, there is some ambiguity since conditions at that location are truly unknown. To cope with this situation, very weak boundary conditions are applied there. Specifically, the streamwise second derivative of each velocity component is set equal to zero. The pressure is taken to be gauge pressure with its datum of zero imposed at the fluid exit.

An important advantage is provided by the participating software for the application of the thermal boundary conditions. It has built-in thermal continuity at all solid-solid interfaces and at solid-liquid interfaces. In particular, continuity of both temperatures and

heat flux are imposed. It still remains to specify the inlet and exit thermal conditions as well as that at the heater faces of the aluminum heat-spreader plates. For the steady-state solution, the inlet temperature is set at a constant equal to 10°C, while at the exit, the second derivative of the temperature in all of the coordinate directions is set equal to zero. With regard to the heater faces of the aluminum heat-spreader plates, the thermal boundary conditions have already been specified in the caption of Figure 6-2.

Table 6-2 lists the heat flux values that were specified in connection with the numerical simulation. In addition to what is conveyed in the caption of Figure 6-2, an alternate condition was applied as part of a sensitivity study. In particular, the adiabatic condition which was initially applied at the unheated portion of the aluminum plates was replaced by a convective heat loss with a heat transfer coefficient of 10 $\frac{\mathrm{W}}{\mathrm{m}^2\mathrm{K}}$ and an ambient temperature of 20°C. The difference in the key results corresponding to these two alternative boundary conditions was found to be negligible.

Table 6-6. Summary of thermal boundary conditions for simulation model

Boundary Conditions	Value
Inlet temperature	10°C
Outlet pressure	0 gauge pressure
Heater zone 1	18,820 W/m^2
Heater zone 2	18,860 W/m^2
Heater zone 3	13,380 W/m^2

For the transient solution, initial conditions are required. For the velocity problem, the initial velocity within the solution domain was taken from the steady-state solution. The boundary conditions were maintained the same as for the steady-state problem. In the case of the thermal solution, the initial temperatures of both the solid and fluid media contained within the solution domain are those of the steady state. The inlet temperature was maintained at 10°C as before as were the weak boundary conditions at the fluid exit.

6.2.4 Numerical solutions

The numerical solutions were implemented by means of ANSYS CFX 14.0 CFD software. The complexity of the fluid flow geometry and conjugate nature of the heat transfer required careful meshing. For the final solutions, the spatial mesh encompassed 2.4 million nodes. This discretization was verified to be sufficient by a mesh independence study to be described shortly. In case of the transient, a suitable time step has to be chosen. By means of a number of comparison solutions, each executed with a different time step, it was found that a time step of 0.01 seconds was suitable for high accuracy.

6.2.4.1 Mesh independence study

The meshing of the solution space is a significant technique since it has a major impact on the accuracy in the results. The fluid passages were subdivided into 56 sections as this allowed a finer mesh to be applied. The following figures, 6-3 to 6-6, will illustrate the nature of the mesh at the fluid inlet, bend sections of the fluid flow path, fluid outlet, and heater portions of the aluminum plate.

Attention is now focused on Figure 6-3 where the mesh at the inlet is displayed. The exhibited mesh consists of two parts, one part being the flow passage and the other encompassing the aluminum plate. Of particular note is the extremely fine mesh (so fine as to appear continuous rather than discrete) in the geometry transition region between the upstream circular tube and the rectangular cross section of the flow passages in the disposable. In the downstream portion of the mesh which spans the fluid, the elements are very regular and form what is often termed a brick mesh. The mesh on the face of the aluminum plate is not nearly as fine as that in the fluid region because the conductivity of the aluminum diminishes the magnitude of the temperature gradients.

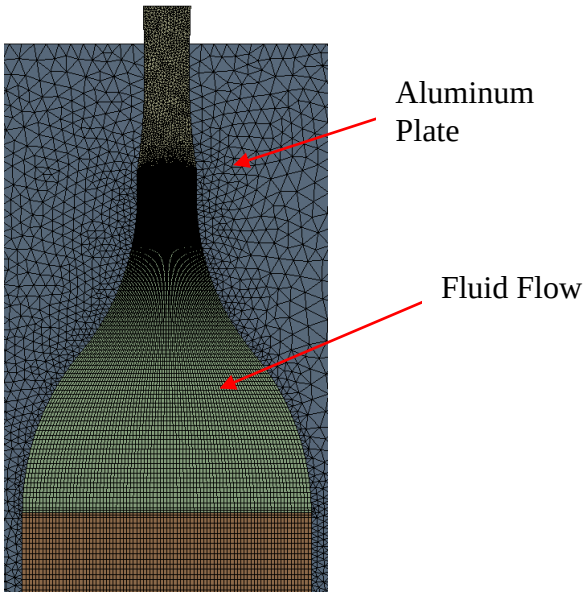

Figure 6-3. Mesh deployment at the inlet encompassing the flow passage and the aluminum plate.

Figure 6-4 shows the mesh strategy that was employed at the bends and the flow passages. The challenge is connect the bend mesh with those in the straight sections of the passages which interconnect with the bend. The goal in the meshing is to create smooth transitions between the three interacting portions of the flow passage.

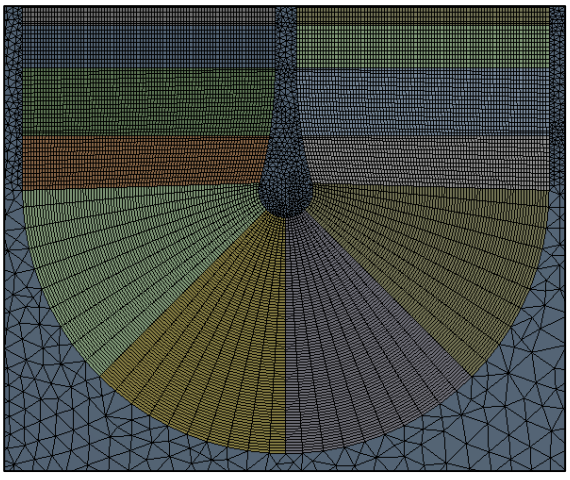

Figure 6-4. Mesh layout at the 180° bends and its connection with the meshes in the interconnecting straight sections.

The next figure, 6-5, shows the mesh deployment at the downstream end of the disposable. This deployment differs from that for the inlet that was previously displayed in Figure 6-3. The reason for this different deployment is that there was no need to consider the presence of a circular tube downstream of the exit. Also shown in Figure 6-5 is the RTD temperature sensor which interconnects with the heater control system.

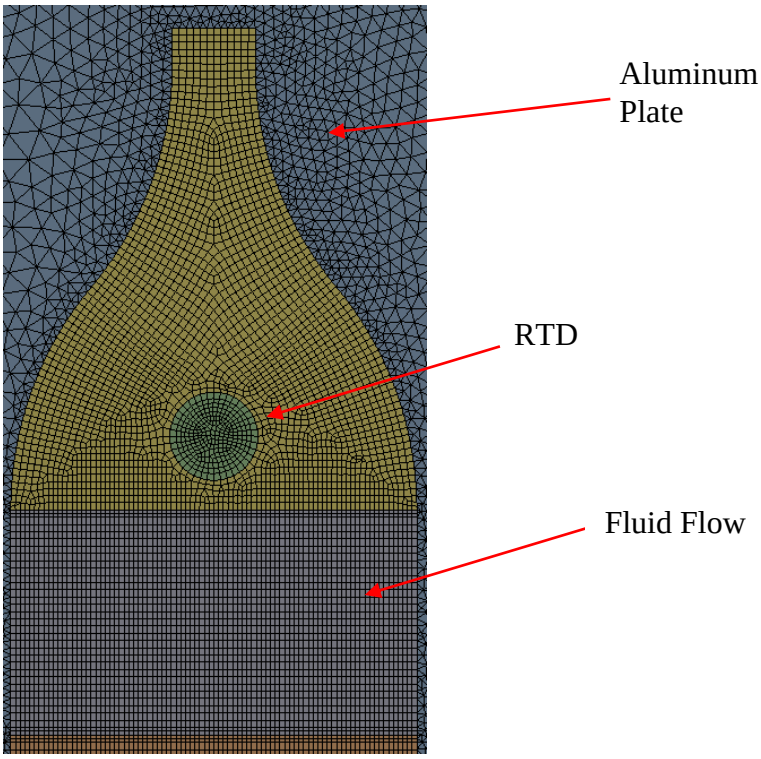

Figure 6-5. Mesh layout at the exit of the disposable.

The last of the mesh-related displays is Figure 6-6. That figure shows the meshing of the heater zones on the back surface of the aluminum heat-spreading plate. For the rectangular sections beneath the heaters, a brick mesh was most suitable. For those sections of non-rectangular shape, meshes tailored to the specific shapes were created. In the spaces not covered by the heaters, tetrahedral elements were employed.

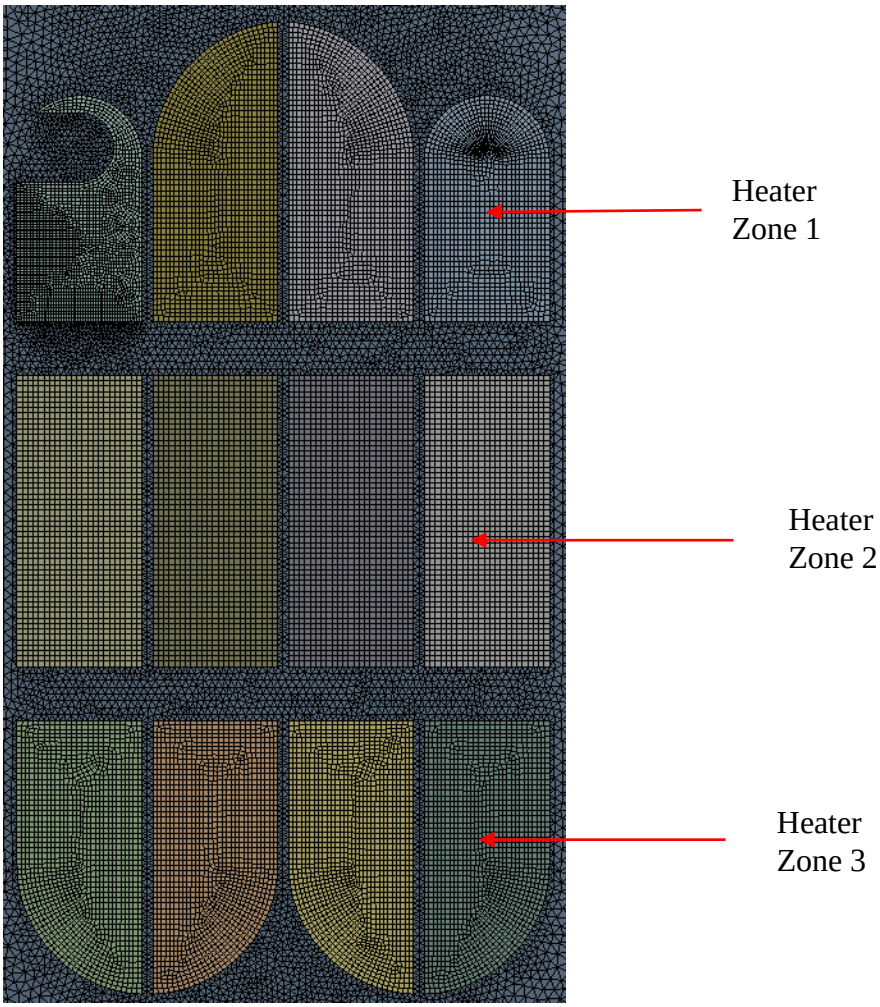

Figure 6-6. Mesh layout for the heater zones.

The outcome of a mesh-independence study is shown in Figure 6-7. As noted earlier, the flow passage was subdivided into 56 control volumes and the bulk temperature of the fluid within each volume was calculated. The study encompassed node numbers of 0.5, 1.1, 2.4, and 4.8 million.

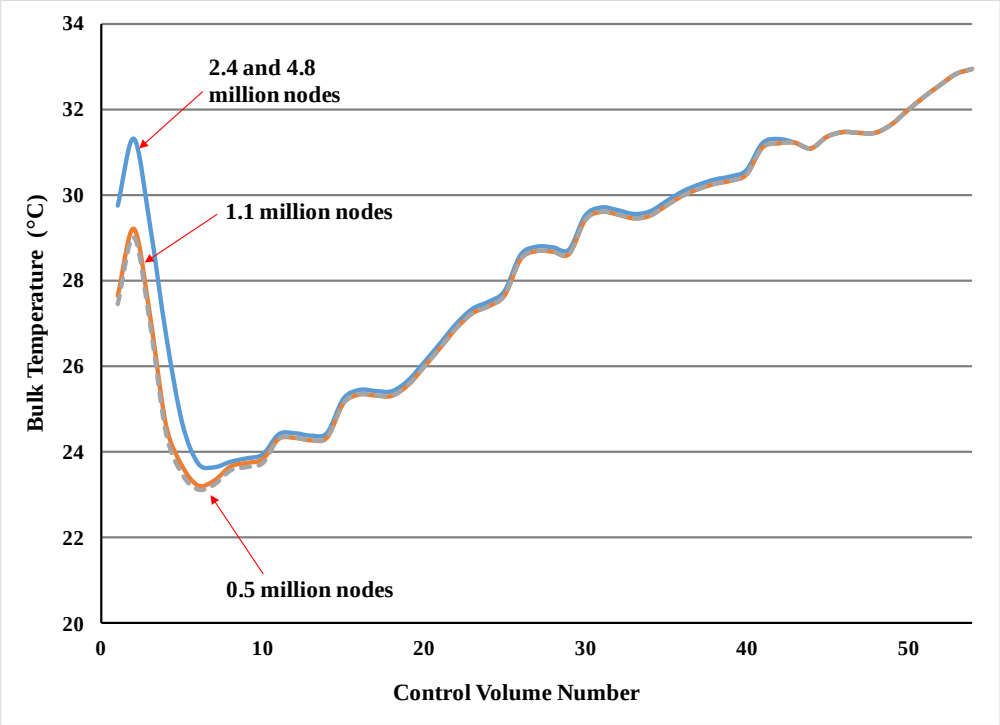

Figure 6-7. Mesh independent study.

The bulk temperatures for each fluid volume are plotted in Figure 6-7. A review of the figure shows that for control volumes 7 through 56, 0.5 million nodes are sufficient, while for control volumes 1 to 7, 2.4 million nodes are needed for high accuracy. Control volumes 1 through 7 are at the inlet of the disposable where flow development is critical. Thus, a need for more nodes is justified.

6.2.4.2 Baseline simulation results

The baseline case was first introduced in Section 6.2. The simulation version of that case was designed to match the geometry and operating conditions of the baseline experiment. The motivation for addressing the baseline case is to validate the simulation model by means of comparisons with the experimental results. Once validated, the model can be used as a mean for guiding the subsequent optimization of the system. The presentation of the simulation results will have two facets. The first is the comparison with the

experimental data, and the second is a display of information that provides insights into the physical phenomena.

Figure 6-8 compares the measured temperatures at 10 locations on the disposable-facing surface of the aluminum heater plate with those predicted by the numerical simulation. An overall inspection of figure indicates very satisfactory agreement between the two sets of results. The maximum deviation of 3°C is highly localized. It occurs in a zone where there are large spatial temperature variations so that a slight deviation of the thermocouple junction from its expected location could well be responsible for the apparent deviation. Overall, it may be concluded that the numerical simulation model is well supported by the experimental data.

Not shown in Figure 6-8 is the comparison between the measured fluid temperature at exit and that predicted by the simulation. The respective temperatures at that location are 28.05°C and 28.88°C. These values agree to better than 1°C and, therefore, provide further validation of the numerical model.

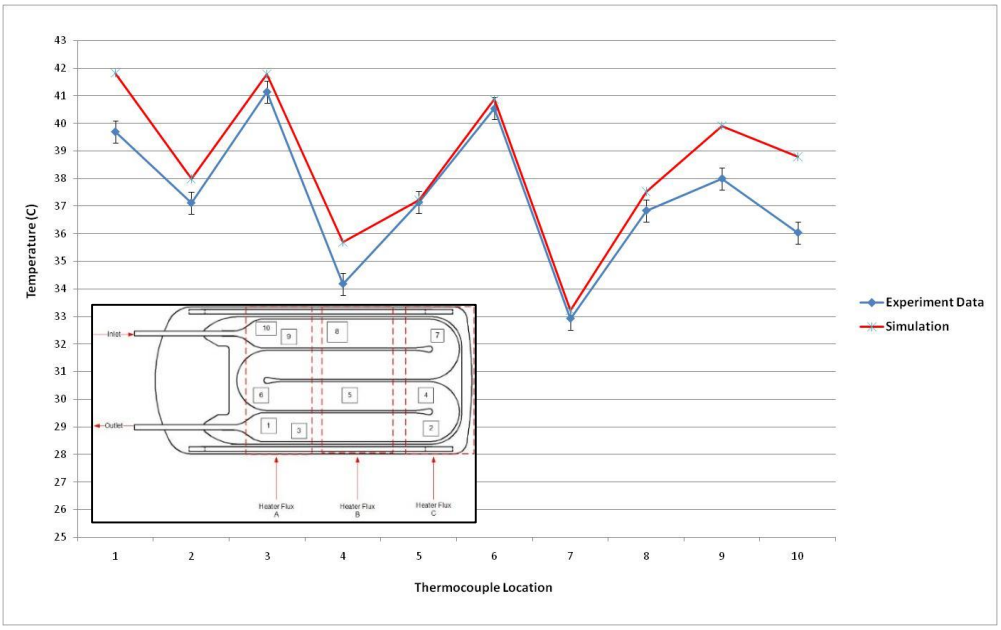

Figure 6-8. Comparison between simulation and experimental temperature results.

The numerical solutions provide more detailed information than could be extracted from the experimental work. One result of interest is the temperature distribution on the disposable-facing surface of the heater plate. This information is conveyed in the color contour diagram of Figure 6-9. It is seen that there is substantial temperature variation across the surface of the plate. The highest temperatures occur at the downstream end of the last flow passage. Although it might seem that this outcome is less than desirable, it is worthy of note that the fluid temperatures in that neighbor are also the highest throughout the disposable. There are a number of reasons to which this outcome can be attributed. One of these is the non-uniformity of the heating power distribution imposed at the outward-facing surface of the plate. Another is the presence of aluminum stiffener bars which are effective in moving heat transversely to the direction of fluid flow.

The significant departure of the temperature distribution from the uniformity is judged to be undesirable, especially under stop-flow conditions. In that situation, the non-uniformity of the temperature would give rise to substantial differences in the heat flow from the plate to the sequestered fluid, thereby opening the possibility of excessive fluid temperature rises.

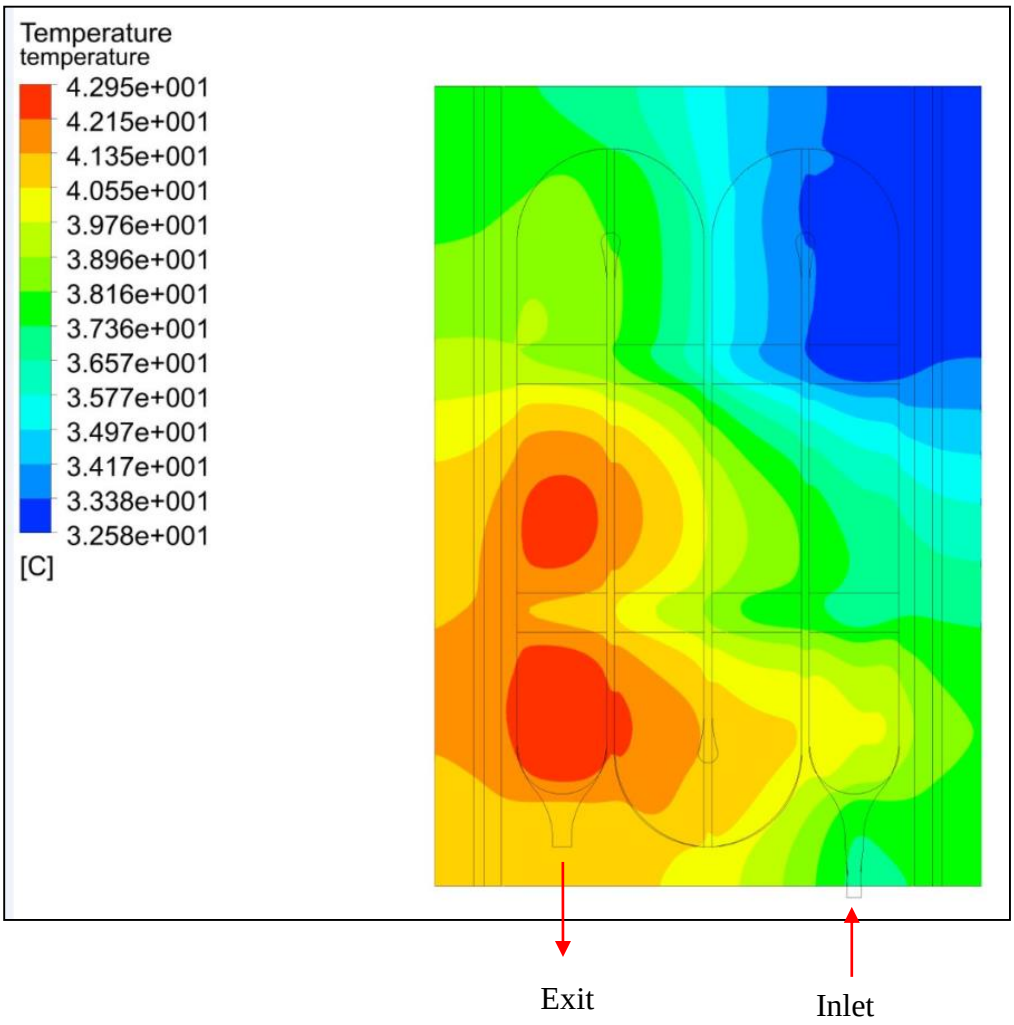

Figure 6-9. Color contour diagram showing the temperature distribution on the disposable-facing surface of the heater plate.

The next figure is a composite of complementary velocity and temperature information. The issue of interest is the behavior of both flow and temperature in the immediate neighborhood of the inlet of the disposable. The left-hand part of the figure is a color contour diagram of the velocity distribution in the immediate neighborhood of the inlet to the disposable. Inspection of that figure reveals the presence of very low velocities (deep blue zones) adjacent to the bounding walls of the flow passage. These zones are actually locations of recirculating flow resulting from the inability of the fluid to accommodate to the rapid expansion of the flow cross section. In general, separated regions are zones of

captive fluid which remain segregated from the main forward-flowing fluid. Since the fluid is captive and very slowly recirculating, it is the recipient of continuous heating which engenders high temperatures. This expectation is verified in the right-hand diagram of Figure 6-10. The temperatures of the fluid in the separated region are clearly the highest in the entire disposable system.

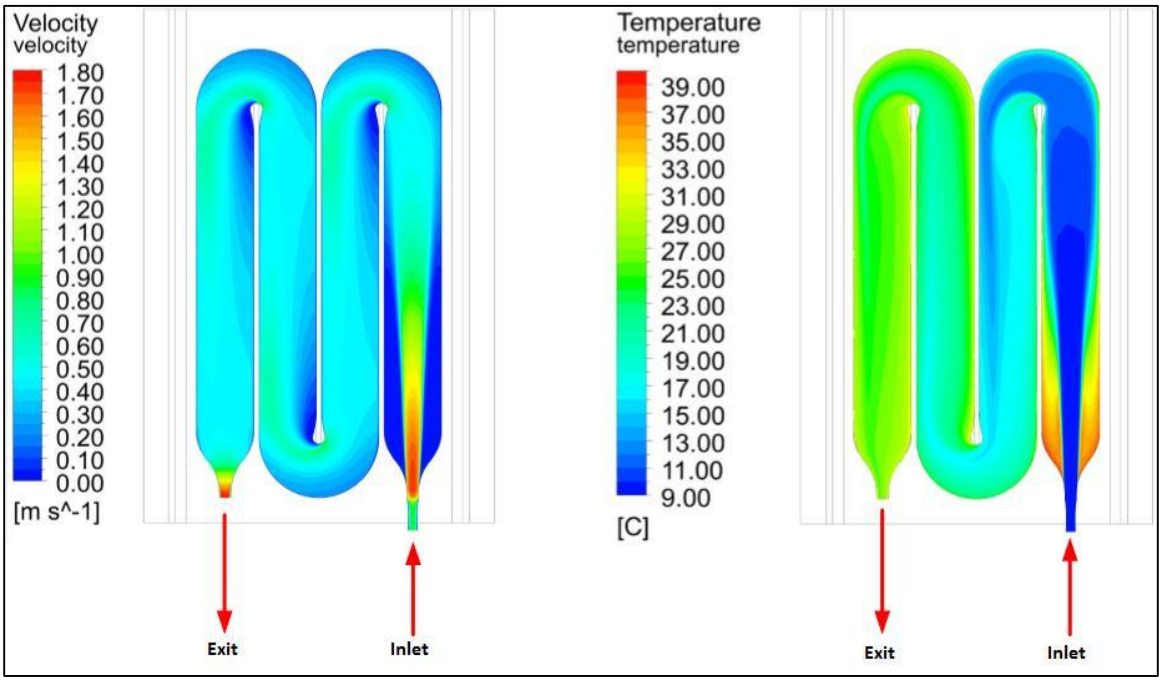

Figure 6-10. Left-hand diagram: velocity distribution in the flow passages and the inlet and exit sections; Right-hand diagram: temperature distribution.

6.3 Simulation for an improved fluid warmer performance

From assessing the simulation results from the baseline case, there is adequate motivation to improve the performance of the fluid warmer. In particular, it is appropriate to seek means of increasing the exit fluid temperature while maintaining the plate temperature to be below 48°C to accommodate the stop-flow scenario [44]. The aforementioned goals can be made plausible by examination of the experimental results that were conveyed in the foregoing. While the setpoint of the system was set to 41°C, the exit fluid temperature at 30 L/hr is approximately 28°C. The fluid leaving the exit of the

disposable is conveyed by plastic tubing to the point of use, which is a patient whose normothermic temperature is approximately 37°C. From this point of view, it is desirable to increase the temperature of the fluid at the exit of the disposable. The rationale for maintaining the plate temperature below 48°C is concern that temperatures above that value would tend transfer excessive heat into the fluid when the stop-flow condition is imposed.

6.3.1 Redesigned of the heating system

Clearly, the attainment of the goals set forth in the preceding paragraph must involve alterations of the heating system. For the redesign, it is proposed that the current three-zone heating pattern be redeployed into six zones, where the heat flux values would be decreasing in value from heaters one to six as shown in Figure 6-11.The choice of six zones and not a larger number is that the interactions among the individual zones would become unmanageable.

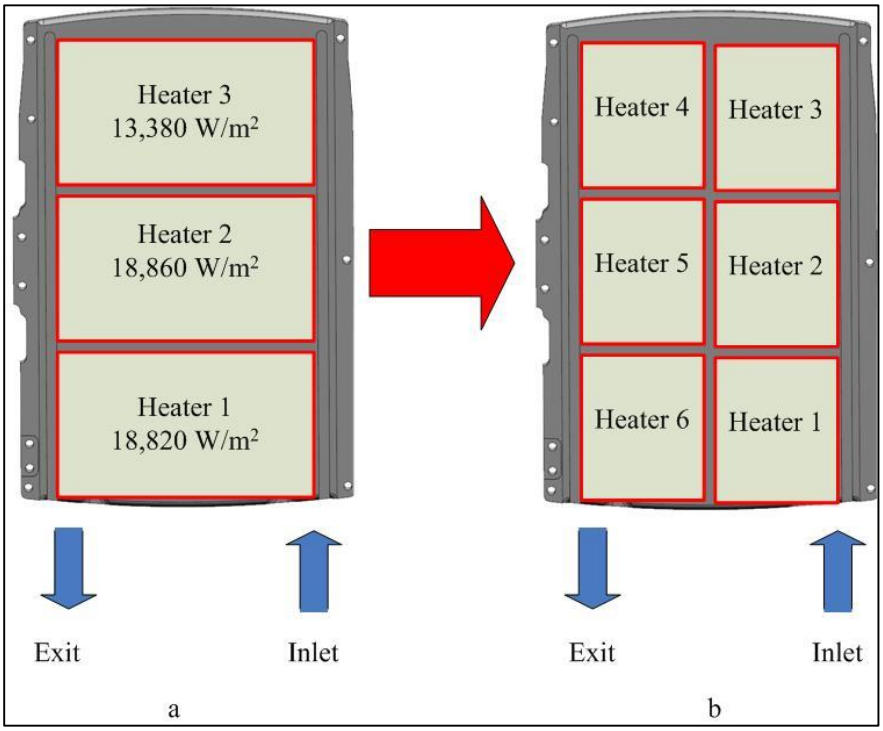

Figure 6-11. (a) Original heater map. (b) Redesigned heater map.

Note that the heat flux values for the redesigned heater map are not stated in the Figure 6-11(b). These flux values were obtained by a process of fine tuning during the course of numerical simulation.

6.3.2 Strategy for simulation

The strategy to determine appropriate heat flux values is an *inverse method* using an iterative process. The current situation is ill-posed in which the unknowns are the rates of heat input to the respective heaters. The objectives are to minimize the high-to-low temperature differences on the heater plate while maximizing the exit fluid temperature. The data inputs to the numerical simulation are: (a) inlet temperature, (b) heat transfer coefficient at the rear face of the heater plate, (c) material properties, (d) flow rates, and (e) trial heat flux values. The geometry of the system is maintained the same as that of the baseline case.

The evaluation of the success of the approach used was based on observation on the outcomes corresponding to a given set of trial heat flux values. Those outcomes include: the plate max-to-min temperature difference and the exit fluid temperature. From this information, the heat flux values for the next iteration were selected based on intuition learned from a training period at the very start of the iterative work.

Table 6-1 lists results from the training period. The goal of the training period was to achieve an average heat flux value for the plate to be similar to the baseline case. The maximum and minimum plate temperatures and exit temperature were computed at each step of the iterations.

Table 6-1. Results of training period

#	Heater 1	Heater 2	Heater 3	Heater 4	Heater 5	Heater 6	Plate Temp (max) °C	Plate Temp (min) °C	Plate Temp Diff °C	Exit Temp °C
Baseline	18820	18860	13380	13380	18860	18820	43.0	32.6	10.4	28.9
1	18000	18000	18000	18000	18000	18000	43.0	34.5	8.5	29.8
2	23000	21000	19000	17000	15000	13000	43.6	36.4	7.2	29.8
3	28000	24000	20000	16000	12000	8000	47.0	37.0	10.0	29.7
4	30000	28000	26000	10000	8000	6000	49.3	36.6	12.7	29.7

From each iteration, a plot similar to Figure 6-12 was created. The figure showed areas of high and low temperatures. The guiding principle for altering the six heat flux inputs was to increase the local flux value where the temperature was low and to decrease the value where the temperature was high.

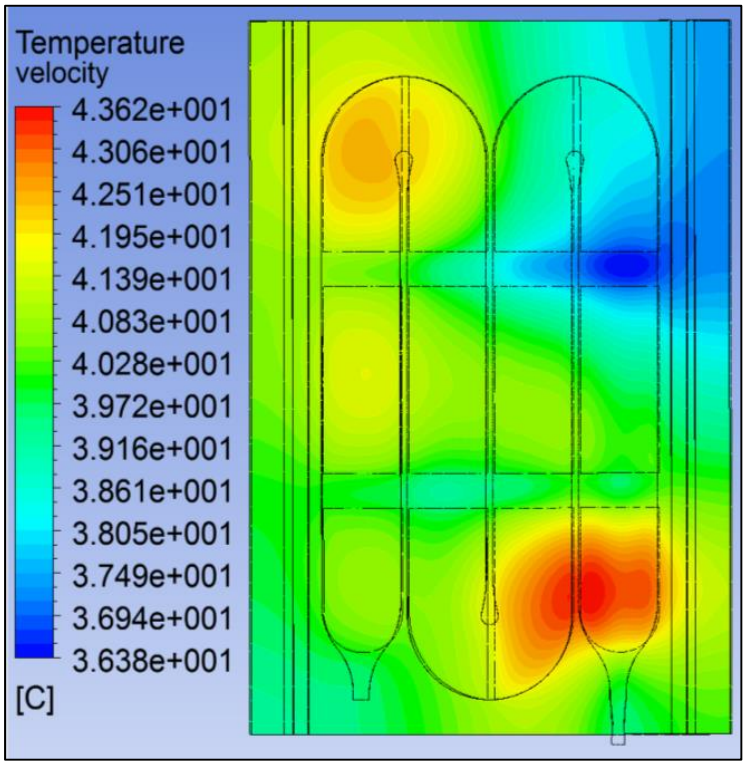

Figure 6-12. An example of a temperature contour map for the exposed face of the aluminum plate.

The final results of the procedure described in the preceding paragraph are displayed in Table 6-2. A review of the results shows that as the heater values are distributed more

evenly, the exit temperature increases while the max-to-min temperature difference of the plate is kept to a minimum.

Table 6-2. Results of heat flux values for the post-training period

#	Heater 1	Heater 2	Heater 3	Heater 4	Heater 5	Heater 6	Plate Temp (max) °C	Plate Temp (min) °C	Plate Temp Diff °C	Exit Temp °C
5	19000	22000	22500	14000	14000	13000	41.3	37.1	4.2	29.6
6	19500	21000	22000	14000	14000	13000	40.9	36.7	4.2	29.0
7	18250	22750	23250	14000	14250	14000	41.2	37.0	4.2	29.6
8	19250	21500	22500	14000	14000	13000	40.9	37.0	3.9	29.1
9	19500	21500	22500	14000	14000	13000	41.1	37.2	4.0	29.2
10	19200	23200	23500	14300	14900	15100	42.2	38.2	4.0	30.2
11	19200	23200	23600	14400	14850	14400	42.0	37.9	4.1	30.1
12	19980	23200	23700	14400	15500	12300	42.2	38.2	4.0	30.2
13	19980	23200	23700	14400	15500	13500	42.5	38.3	4.1	30.2
14	19980	23200	23700	14400	15500	14000	42.6	38.5	4.1	30.4

Iteration 14 sets forth the final results. As expected for optimum performance, the largest heat flux value occur in the first two legs of the flow passage. The fact that heater 1 is somewhat less in magnitude than heaters 2 and 3 is attributable to the separated flow which occurs just downstream of the inlet. The smallest max-to-min temperature difference on the plate surface is about 4°C. This outcome is a major improvement over the 10°C temperature difference for the baseline case. It is also seen from the table that the exit fluid temperature is predicted to be 30.4°C, which reflects a modest increase from the 28.9°C exit temperature for the baseline case.

A graphical summary of the key results of the design procedure is conveyed by Figures 6-13(a) and (b). Figure 6-13(a) is a color contour diagram showing the temperature distribution on the external face of the heater plate. Of particular note is the temperature of the plate in the neighborhood of the fluid exit zone. That temperature is constrained by the control system never to exceed 41°C. This is the reason why the temperature in that neighborhood is lower than that at other regions of the plate. The (b) part of the figure displays the fluid temperature. The highest temperatures occur in the separated region just downstream of the fluid inlet. The fluid in a separated region recirculates and never escapes. Therefore, it is more vulnerable to heating than fluid which is passing through. Aside from the aforementioned zone of high temperature near the inlet, the highest of the other temperatures occur in the last leg of the flow passage.

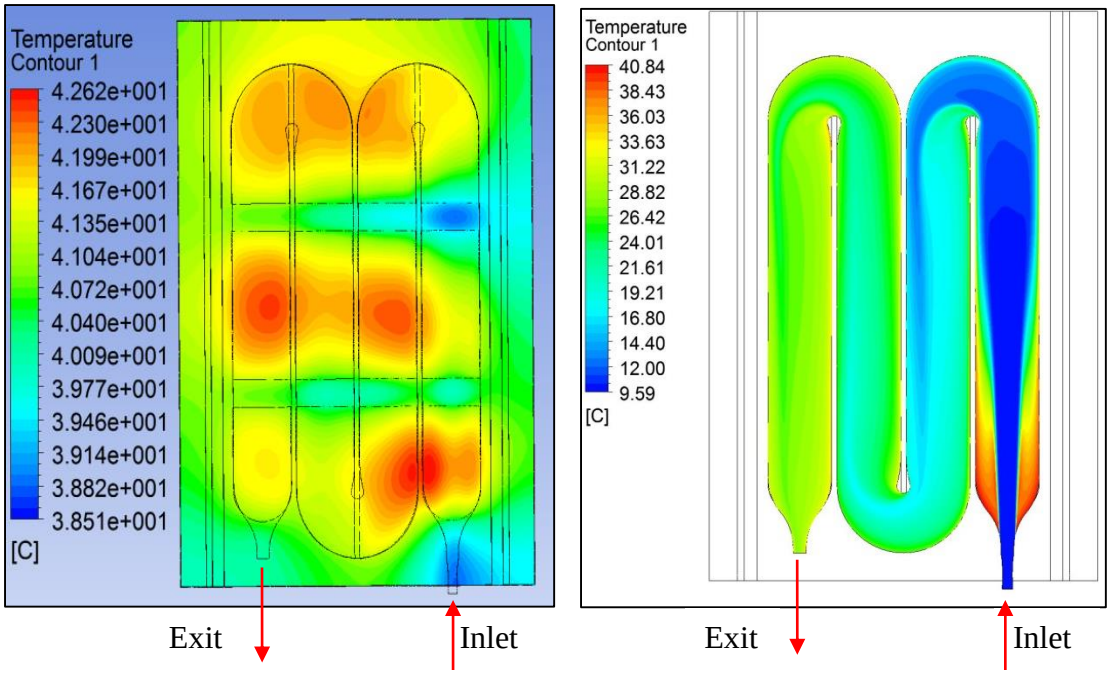

Figure 6-13. (a) Temperature distribution of plate for steady-state condition and (b) Fluid temperature distribution for steady-state condition.

The success of the new design can be observed graphically in Figure 6-14. The figure shows the variations of both the maximum plate temperature and the maximum fluid temperature subsequent to stop flow. Although the fluid flow is stopped at a certain moment of time, the heating continues until the temperature of the control point reaches 41°C. However, this constraint does not prevent temperatures at other points on the plate surface to reach higher temperatures. As shown in the figure, the highest plate temperature achieved is 47.2°C. That temperature is achieved in the zone serviced by heater number 5. The fluid temperature does not achieve values as high as that achieved by the plate; its maximum value is 45.4°C. It is interesting to note that as time evolves, the maximum fluid temperature slightly exceeds the maximum plate temperature. This apparent paradox is readily understood by recognizing that the respective maxima do not occur in the same zone. In particular, the maximum fluid temperature occurs within the separated flow region just downstream of the fluid inlet.

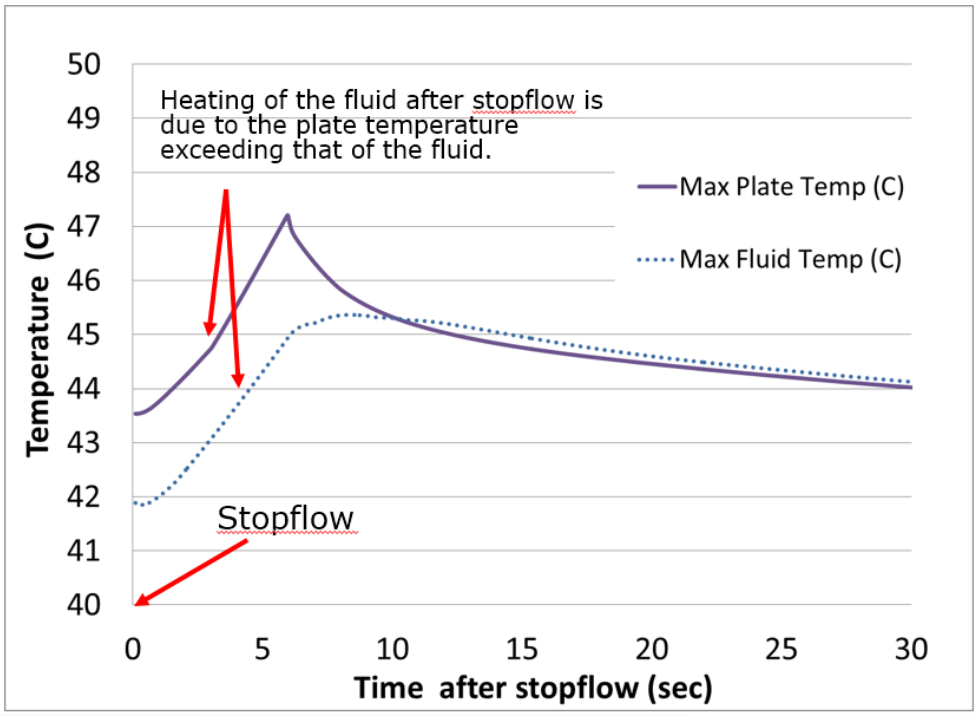

Figure 6-14. Variation of the maximum plate temperature and maximum fluid temperature as a function of time subsequent to stop flow.

6.4 Experimental verification of the new designed heating pattern

Numerical simulation is a valuable design tool only when it has been verified. Among the potential verification means, the most trusted is experimentation. To this end, an experiment encompassing the new six-zone heater design was performed. The physical manifestation of the six-zone heater is displayed in Figure 6-15. Each zone is clearly marked. The individual-zone heat fluxes obtained from the simulation from the previous sections of this chapter served as input. The same test setup described in Chapter 5 was used to facilitate the experiment.

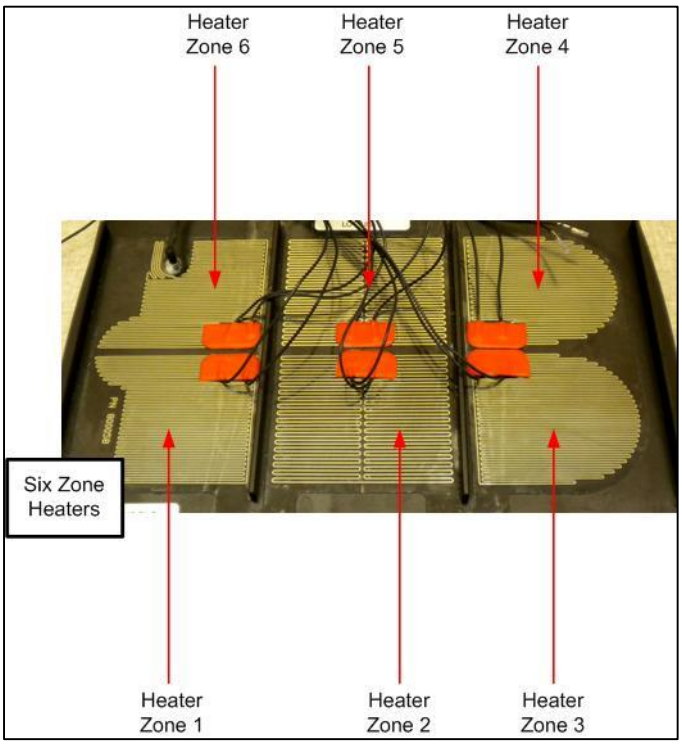

Figure 6-15. The six-zone heater layout.

For reference purposes, the locations of the eight thermocouples with respect to the six-zone heater is shown in Figure 6-16.

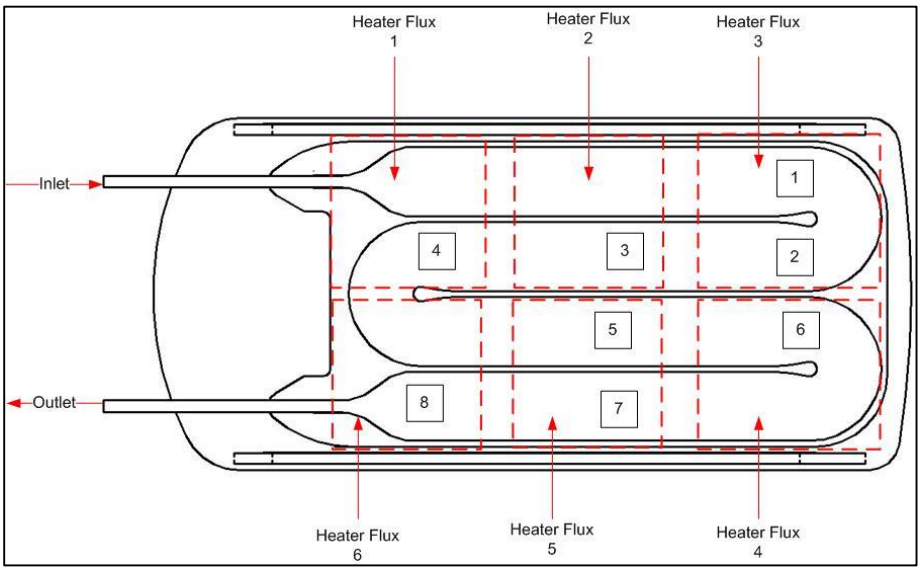

Figure 6-16. Map of thermocouple locations on the disposable-facing surface of the aluminum plate with respect to the six-zone heaters superimposed.

A comparison of the predicted temperatures at the locations of the eight thermocouples with the experimental data is displayed in Figure 6-17. Inspection of the figure indicates that except at the location of thermocouple 8, the numerical prediction and the experimental data do not deviate more than 2°C. The slightly larger deviation at the location thermocouple 8 may be attributed to the near presence of the control point RTD installation, since precise modeling of the RTD installation is questionable. Furthermore, the fluid exit temperatures between the experiment and simulation are 31.3°C and 30.4°C respectively; agreement between the two values is within 1°C.

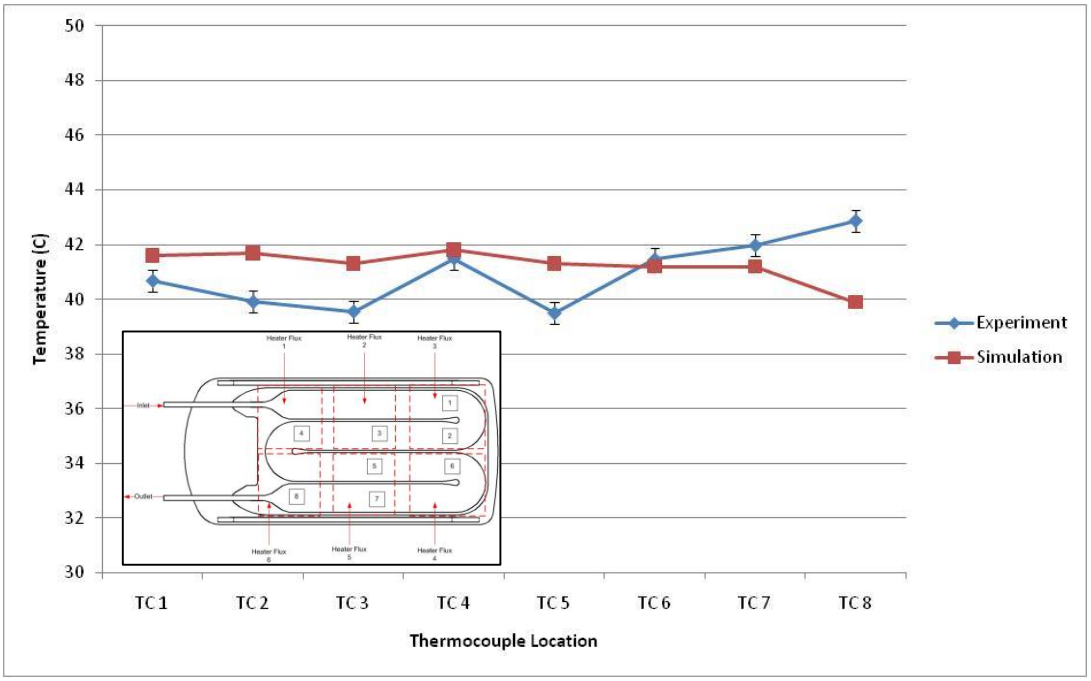

Figure 6-17. Comparison between simulation and experimental temperature results for the size-zone heater design.

The excellent agreement evidenced by foregoing comparison strongly supports the numerical simulation model and its implementation. Therefore, it can be used with high effectiveness as a design tool for further optimization of the device.

6.5 Outcomes of Chapter 6

The use of numerical simulations can provide predictive analysis that serves to reduce the amount of experimental work. The analysis at hand was to increase the output temperature while maintaining a temperature of 48°C at stopflow. This goal was accomplished by optimizing the heater module layout pattern.

Using Ansys CFX 14.0, the baseline was modeled and validated with experimental methods. Once the baseline numerical model for three-zone heater was validated, an iterative process using an Inverse Method was implemented for the six-zone heater design. The redesigned heater layout had a modest temperature outlet increase of 1.5°C.

The numerical simulation model was then compared to experimental results with agreements between the two methods to be within 2°C.

CHAPTER 7

Concluding Remarks

The goal of this research was to apply rigorous physical principles to the design of thermal-based biomedical therapeutic devices. The accomplishment of this goal was achieved by synergistic interactions of numerical simulations and experimentation. The research extended over two discrete focal devices: (a) a noninvasive means for determining the body core temperature and (b) a means for maintaining near-normothermic body core temperature during operating room procedures by infusion of appropriate fluids. The devices described in the foregoing operate synergistically in that the need for the fluid infusions is dictated by the knowledge of the body core temperature. It was demonstrated that rational first-principles design could be rigorously applied with a minimum of simplifying assumptions.

Rational models were made of the participating fluid flow and heat transfer processes. These models were incorporated into numerical simulation means to yield thermal and fluid flow results. To verify both the models and the simulation methodology, painstaking experiments were devised and executed. The experimental hardware was created with attention to detail to enable experiments of impeccable accuracy to be performed. The experimental results were used as a means of validating the simulation-based predictions.

The first focus of the thesis research was to devise a temperature probe capable of noninvasively determining body core temperature. The positioning of such a probe was deemed most acceptable on the forehead because of the close proximity of the carotid artery. The principle underlying the design of the probe was the suppression of heat flow at the point of temperature measurement. This principle was maintained as the dimensions and materials of the probe were varied parametrically. Since the

determination of the core temperature is a timewise necessity, the numerical simulations were performed in the transient mode. A steady-state model was also devised as a means for verifying the more complex transient analysis.

The initial probe configuration demonstrated lagging performance in that approximately 10 minutes was required to achieve a steady temperature outcome. A change in the material media from a polymeric foam to aluminum dramatically increased the responsiveness of the probe so that steady state was achievable within 0.5 minutes. A further enhancement gave rise to compactness while maintaining the accuracy of the temperature measurement and its responsiveness.

To support the aforementioned simulation-based probe design, an experimental protocol was created with the goal of testing the critical issues of the model. The experimental work consisted of two independent activities. In the first, an *ex-vivo* setup was designed and fabricated to facilitate the collection of highly accurate temperature data at a simulated skin surface and body core. The experimental setup enabled precise control of the operating conditions and, thereby, provided a valid test of the simulation-based design. Three independent replicate data runs were performed. The differences between the measured skin temperature and that of the simulated core for the respective data runs were $0.1^{o}C$. Since the accepted standard of temperature measurement accuracy is $0.5^{o}C$, the satisfactory performance of the probe is thereby established.

Another means of interrogating the accuracy of the numerical-simulation results was to make use of clinical data. A drawback of doing so was that the personnel involved with the data collection were free to use their own methodologies. Another drawback was that a sublingual (oral) temperature measurement was regarded as representing the core temperature, despite the fact that medical practitioners are widely dispersed in their opinions of the sublingual temperature as a surrogate for the core temperature.

The quality of the probe-measured temperatures was deduced from statistical processing of the data in the form ($T_{probe} - T_{oral}$). The standard deviations obtained from these operations displayed values well within the required accuracy. The logic-based design innovations, including material substitution and miniaturization, have led to heighted accuracy, improved temporal responsiveness, and to greater flexibility with respect to placement due to compaction.

The second focus of the thesis was directed to fluid-conditioning devices with a specific focus on temperature. The introduction of a restorative fluid into the human body at a temperature considerably lower than the body's normotheric value can lead to negative outcomes including hypothermia. This is especially true when large infusions of fluid are required over a very short time, thereby not allowing for suitable equilibration. Whenever blood is infused, it is accompanied by the infusion of saline. In the case of dehydration, saline alone is sufficient.

Blood warming is a care-requiring process. In particular, the danger of local overheating requires careful control. The device that was devised to perform the heating of both blood and saline included a multi-pass fluid flow trajectory punctuated with 180^{o} turns needed to fulfill compactness requirements. Heating of the fluid in question was achieved by use of electrically heated homogenizing plates which function as thermal temperature homogenizers.

During the period of fluid infusion, singular events may occur which require modulated responses by the fluid heating system. One of these events is called stopflow, wherein an unforeseen medical crisis occurs which mandates immediate cession of fluid infusion. The suppression of fluid flow does not necessarily coincide with the termination of heat flow into the now-stationary fluid. The heat capacity of the homogenizing plates coupled with their elevated temperatures becomes an unintended and uncontrolled heat source. The issue of hemolysis becomes a possible reality. One of the features of the thermal

design of the system was to tailor the heat capacity of the homogenizing plates to ensure failsafe temperature excursions of the nonmoving fluid.

The sensitive nature of the fluid warming system, as described in the foregoing, demanded a first-principles investigation that included both numerical simulations and precision-level experimentation. The simulation model included three-dimensional, transient fluid flow which was necessarily coupled to three-dimensional, transient, and conjugate conduction heat transfer. By conjugate heat transfer, it is meant that the convective transfer between the flowing fluid and the wall of the homogenizing plates had to be coupled with the conduction within the plates. The complexity of the fluid flow was enhanced by the need for compactness of the flow passages. The solution for the compactness requirement was to use a multi-pass orientation of the flow passages which necessitated the use of several 180^{o} turns. Such flow reversals necessarily bring about flow separation and recirculation. The same compactness requirement also created the need for too-rapid expansion.

One of the major goals of the design effort was to increase the temperature of the fluid exiting the fluid-warming device. To this end, a reconfiguration of the pattern of fluid warming was performed by means of numerical simulation. This simulation was, in fact, a second round, the first round being the evaluation of the characteristics of an original design. The particular value of the two-stage simulation pattern was to evaluate the degree of improvement brought about by the design features that were incorporated subsequent to the original design.

The experimentation also encompassed a two-stage pattern, the first stage making use of the original design and the second stage involving the revised design based on the information gleaned from both the simulation and the experimentation of the original design.

The validation of both the original and updated simulation-based designs was performed by comparisons with the results of the corresponding experiments. The comparisons consisted of contrasting, on a one-on-one basis, temperature information at 10 distinct locations within the fluid-warming system. These comparisons turned out to be highly favorable for both the original design and the subsequently updated design. In no case did the comparison show a difference in temperature greater than 2°C. Another goal of the redesigned system was to increase the temperature of the fluid exiting the system. That goal was fulfilled to the extent of an increase of the temperature by 1.5°C.

References

[1]. Teunissen, L. P., Klewer, J., De Hann, A., De Koning, J. J., & Daanen, H. A. (2011). Non-invasive continuous core temperature measurement by zero heat flux. *Physiological Measurement, 32*, 559-570.

[2]. Pusnik, I., & Miklavec, A. (2009). Dilemmas in Measurement of Human Body Temperature. *Instrumentation Science and Technology*, *37*, 516-530.

[3]. Longo, D. L., & Harrison, T. R. (2011). Fever and Hyperthermia. In *Harrison's principles of internal medicine* (18th ed.). New York: McGraw-Hill.

[4]. Niedermann, R., Wyss, E., Annaheim, S., Psikuta, A., Savey, S., & Rossi, R. M. (2013). Prediction of human core temperature using non-invasive measurement methods. *International Journal of Biometeorology*.

[5]. Yamakage, M., & Namiki, A. (2003). Deep temperature monitoring using a zero-heat-flow method. *Journal of Anesthesia*, *17*, 108-115.

[6]. Frommelt, T., Ott, C., & Hays, V. (2008). Accuracy of different devices to measure temperature. *MEDSURG Nursing*, *17*(3), 171-182.

[7]. Fox, R. H., & Solman, A. J. (1971). A new technique for monitoring the deep body temperature in man from the intact skin surface. *Journal of Physiology, 212*(2), 8-10.

[8]. Fox, R. H., Solman, A. J., Isaacs, R., Fry, A. J., & MacDonald, I. C. (1973). A new method for monitoring deep body temperature from the skin surface. *Clinical Science*, *44*, 81-86.

[9]. Kobayashi, T., Nemoto, T., Kamiya, A., Togawa, T. (1975). Improvement of deep body thermometer for man. *Annals of Biomedical Engineering*, *3*, 181-188.

[10]. Togawa, T. (1979). Non-invasive deep body temperature measurement. *Non-invasive physiological measurements, 1*, 261-277.

[11]. Binzoni, T., Springett, R., Dalton, J. C., & Delpy, D. (1999). A new combined deep-body-temperature/nirs probe for non-invasive metabolic measurements on human skeletal muscle.*Advances in Experimental Medicine and Biology*, *471*, 623-629.

[12]. Kimberger, O., Thell, R., Schuh, M., Koch, J., Sessler, D., & Kurz, A. (2009). Accuracy and precision of a novel non-invasive core temperature. *British Journal of Anaesthesia*,*103*(2), 226-231.

[13]. Zeiner, A., Klewer, J., Sterz, F., Haugk, M., Krizanac, D., Testori, C., . . . Losert, H. (2010). Non-invasive continuous cerebral temperature monitoring in patients treated with mild therapeutic hypothermia: an observational pilot study. *Resuscitation*, *81*(7), 861-866.

[14]. Yamakage, M., Iwasaki, S., & Namiki, A. (2002). Evaluation of newly developed monitor of deep body temperature. *Journal of Anesthesia*, *16*, 354-357.

[15]. Matsukawa, T., Sessler, D. I., Ozaki, M., Hanagata, K., Iwashita, H., & Kumazawa, T. (1997). Comparison of distal oesophageal temperature with deep and trachael temperatures. *Canadian Journal of Anesthesia*, *44*(4), 433-438.

[16]. Sessler, D. I. (2008). Temperature monitoring and perioperative thermoregulation.*Anesthesiology*, *109*, 318-338.

[17]. Harioka, T., Matsukawa, T., Ozaki, M., Nomura, K., Sone, T., Kakuyama, M., & Toda, H. (200). Deep-forehead temperature correlates well with blood temperature. *Canadian Journal of Anesthesia*, *47*(10), 980-983.

[18]. Pennes, H. H. (1948). Analysis of tissue and arterial blood temperatures in the resting human forearm. *Journal of Applied Physiology*, *1*(2), 93-122.

[19]. Kolios, M. C., Worthington, A. E., Sherar, M. D., & Hunt, J. W. (1998). Experimental evaluation of two simple thermal models using transient temperature analysis. *Physics in Medicine and Biology*, *43*, 3325-3340.

[20]. Lyons, B. E., Samulski, T. V., Cox, R. S., & Fessenden, P. (1989). Heat loss and blood flow during hyperthermia in normal canine brain. *International Journal of Hyperthermia*, *5*, 225-247.

[21]. Zhu, L., & Xu, L. X. (1999). Evaluation of the effectiveness of transurethral radio frequency hyperthermia in the canine prostate: temperature distribution analysis. *ASME Journal of Biomedical Engineering*, *121*, 584-590.

[22]. Weinbaum, S., Lemons, D. E., & Jiji, L. M. (1984). Theory and experiment for the effect of vascular microstructure on surface tissue heat transfer - part II: model formulation and solution. *Journal of Biomechanical engineering*, *106*, 331-341.

[23]. Janssen, F. E., Van Leeuwen, G. M., & Van Sttenhoven, A. A. (2005). Modeling of temperature and perfusion during scalp cooling. *Physics in Medicine and Biology*, *50*, 4065-4073.

[24]. Holman, J. P. (1997). *Heat transfer* (8th ed.). New York: McGraw-Hill Companies.

[25]. Gebhart, B. (1988). *Buoyancy-induced flows and transport*. Washington [D.C.: Hemisphere Pub. Corp.

[26]. McAdams, W. H. (1954). *Heat Transmission* (3rd ed.). New York: McGraw-Hill Book Company.

[27]. Eckert, E. R., & Jackson, T. W. (1951). Analysis of turbulent free convection boundary layer on a flat plate. *NACA Report, 1015*.

[28]. Warner, C. Y., & Arpaci, V. S. (1968). An experimental investigation of turbulent natural convection in air at low pressure along a vertical heated flat plate. *International Journal of Heat and Mass Transfer, 11*, 397.

[29]. Bayley, F. J. (1955). An analysis of turbulent free convection heat transfer. *Proceedings of the Institution of Mechanical Engineers, 169*(20), 361.

[30]. Fujii, T., & Imura, H. (1972). Natural convection heat transfer from a plate with arbitrary inclination. *International Journal of Heat and Mass Transfer, 15*, 755.

[31]. Llyod, J. R., & Moran, W. R. (1974). Natural Convection Adjacent to Horizontal Surface of Various Planforms. *Journal of Heat Transfer, 96*(4), 443-447.

[32]. Winslow, E. H., Cooper, S. K., Haws, D. M., Balluck, J. P., Jones, C. M., Morse, E. C., . . . Edwards, T. D. (2012). Unplanned perioperative hypothermia and agreement between oral, temporal artery, and bladder temperatures in adult major surgery patients. *Journal of Perianesthesia Nursing, 27*(3), 165-180.

[33]. Fukuoka, M., Yamori, Y., & Toyoshima, T. (1986). Twenty-four hour monitoring of deep body temperature with a novel flexible probe. *Journal of Biomedical Engineering, 9*, 173-176.

[34]. Lees, D. E., Kim, Y. D., & Macnamara, T. E. (1980). Noninvasive determination of core temperature during anesthesia. *Southern Medical Journal*, *73*(10), 1322-1324.

[35]. Nemoto, T., & Togawa, T. (1988). Improved probe for a deep body thermometer. *Medical & Biological Engineering & Computing*, *26*, 456-459.

[36]. Sparrow, E.M., Miller, G.B., and Jonsson, V.K. (1962). Radiative effectiveness of annular- finned space radiators, including mutual irradiation between radiator elements. *Journal of Aerospace Science,* 29(11), 1291-1299.

[37]. Kurz, A., Sessler, D. I., Christensen, R., & Dechert, M. (1995). Heat Balance and Distribution during the Core-Temperature Plateau in Anesthetized Humans. *Anesthesiology,* 83: 491-499.

[38]. Jurkovich, G. J., Greiser, W. B., Luterman, A., & Curreri, P. W. (1987). Hypothermia in Trauma Victims: An Ominous Predictor of Survival. *Journal of Trauma-injury Infection and Critical Care*, 27: 1019-1022.

[39]. Rajek, A., Greif, R., Sessler, D. I., Baumgardner, J., Laciny, S., & Bastanmehr, H. (2000). Core Cooling by Central Venous Infusion of Ice-cold (4^{o}C and 20^{o}C) Fluid: Isolation of Core and Peripheral Thermal Compartments. *Anesthesiology*, 93: 629-637.

[40]. Gentilello, L. M., Cobean, R. A., Offner, P. J., Soderberg, R. W., & Jurkovich, G. J. (1992). Continuous Arteriovenous Rewarming: Rapid Reversal of Hypothermia in Critically Ill Patients. *Journal of Trauma-injury Infection and Critical Care*, 32: 1436-1449.

[41]. Gentilello, L. M., Cobean, R. A., Offner, P. J., Soderberg, R. W., & Jurkovich, G. J. (1992). Continuous Arteriovenous Rewarming: Rapid Reversal of Hypothermia in Critically Ill Patients. *Journal of Trauma-injury Infection and Critical Care*, 32: 16-25.

[42]. Barcelona, S. L., & Vilich, F. (2003). A Comparison of Flow Rates and Warming Capabilities of the Level 1 and Rapid Infusion System with Various-Size Intravenous Catheters. *Anesthesia and Analgesia*, 358-363.

[43]. Satoh, J., Yamakage, M., Asaki, S. I., & Namiki, A. (2006). Performance of Three Systems for Warming Intravenous Fluids at Different Flow Rates. *Anaesth Intensive Care*, 34: 46-50.

[44]. ASTM Standard F 2172-02, 2011, "Standard Specification for Blood/Intravenous Fluid/Irrigation Fluid Warmers," ASTM International, West Conshohocken, PA, 2011, DOI: 10.1520/F2172-02R11, www.astm.org.

[45]. Avallone, E. A., Baumeister, T., Sadegh, A., & Marks, L. S. (1996). *Mark's Standard handbook for mechanical engineers 11 th Edition*. McGraw-Hill.

[46]. Sparrow, E. M., Beavers, G. S., & Magnuson, R. A. (1970). Experiments on Hydrodynamically Developing Flow in Rectangular Ducts of Arbitrary Aspect Ratio. *International Journal of Heat and Mass Transfer*, 13, 689-702.

[47]. Sparrow, E. M., Abraham, J. P., & Minkowycz, W. J. (2009). Flow separation in a diverging conical duct: Effect of Reynolds number and

divergence angle. *International Journal of Heat and Mass Transfer*, 52, 3079-3083.

[48]. Faries, Aries, G., Johnston, C., Pruitt, K., & Plouff, R. (1991). Temperature relationship to distance and flow rate of warmed IV fluids. *Annals of Emergency Medicine,* 48: 1198-1200.

[49]. Eshraghi, Y., & Sessler, D. I. Exploratory Method-Comparison Evaluation of a Disposable Non-Invasive Zero Heat Flow Thermometry System. 2012 American Society of Anesthesiologists Annual meeting. A63.

[50]. Engineering ToolBox. (n.d.). Retrieved from http://www.engineeringtoolbox.com

[51]. Becker, J. A., Green, C. B., & Pearson, G. L. (1946). Properties and Uses of Thermistors - Thermally Sensitive Resistors. *Transactions of The American Institute of Electrical Engineers, 65: 711-725*.

[52]. Steinhart, J., & Hart, S. (1968). Calibration curves for thermistors. *Deep Sea Research and Oceanographic Abstracts, 15: 497-503.*

[53]. Giuliano, K. K., Scott, S. S., Elliot, S., & Giuliano, A. J. (1999). Temperature measurement in critically ill orally intubated adults: A comparison of pulmonary artery core, tympanic, and oral methods. *Critical Care Medicine*, V27 (10): 2188-2193.

[54]. Gunga, H., Sandsund, M., Reinertsen, R. E., Sattler, F., & Koch, J. (2008). A non-invasive device to continuously determine heat strain in humans. *Journal of Thermal Biology*, 33: 297-307.

[55]. Nutter, G. D. (1988). Radiation thermometry: The measurement problem.

[56]. Betta, V., Cascetta, F., & Sepe, D. (1997). An assessment of infrared tympanic thermometers for body temperature measurement. *Physiological Measurement*, 18: 215-225.

[57]. Kistemaker, J. A., Hartog, E. A., & Daanen, H. A. (2006). Reliability of an infrared forehead skin thermometer for core temperature measurements. *Journal of Medical Engineering & Technology*, 30: 252-261.

[58]. Ikeda, T., Sessler, D. I., Marder, D., & Xiong, J. (1997). Influence of Thermoregulatory Vasomotion and Ambient Temperature Variation on the Accuracy of Core-temperature Estimates by Cutaneous Liquid-crystal Thermometers. *Anesthesiology*, 86: 603-12.

[59]. Mackenize, R., & Asbury, A. J. (1994). Clinical evaluation of liquid crystal skin thermometers. *British Journal of Anaesthesia*, 72: 246-249.

[60]. Somers, E. V., & Cyphers, J. A. (1951). Analysis of Errors in Measuring Thermal Conductivity of Insulating Materials. *Review of Scientific Instruments*, 22: 583-586.

[61]. Erickson, R. S., & Kirklin, S. K. (1993). Comparison of ear-based, bladder, oral, and axillary methods for core temperature measurement. *Critical care medicine*, *21*(10), 1528-1534.

[62]. Moran, D S, Moran, L, & Mendal. (2002). Core temperature measurement. Sports medicine, 32(14), 879-885.

[63]. Rajek, A. (2000). Core cooling by central venous infusion of ice-cold (4 c and 20 c) fluid: Isolation of core and peripheral thermal compartments. Anesthesiology, 93(3), 629.

[64]. Charlmers, C., & Russell, W. J. (1974). When Does Blood Haemolyse?: A Temperature Study. *British Journal of Anaesthesia*, 46 (10): 742-746.

[65]. Brown, M. E. (Ed.). (2001). Introduction to thermal analysis: techniques and applications (Vol. 1). Springer.